

**CHARACTERIZATION OF PLATINUM-GROUP METAL
NANOPHASE ELECTROCATALYSTS EMPLOYED IN
THE DIRECT METHANOL FUEL CELL AND
SOLID-POLYMER ELECTROLYTE ELECTROLYSER**

MARIO WILLIAMS



A thesis submitted in fulfilment of the requirements for the degree of Magister Scientiae
in the Department of Chemistry, University of the Western Cape.

Supervisor: Prof. V.M. Linkov

Co-supervisor: Dr. L. Khotseng

November 2005

DECLARATION

I declare that “*Characterization of Platinum-Group Metal Nanophase Electrocatalysts Employed in the Direct Methanol Fuel Cell and Solid-Polymer Electrolyte Electrolyser*” is my own work, that it has not been submitted for any degree or examination in any other university, and that all the sources I have used or quoted have been indicated and acknowledged by complete references.

Mario Williams



November 2005

Signed:.....

SYNOPSIS

CHARACTERIZATION OF PLATINUM-GROUP METAL NANOPHASE ELECTROCATALYSTS EMPLOYED IN THE DIRECT METHANOL FUEL CELL AND SOLID-POLYMER ELECTROLYTE ELECTROLYSER

M. Williams

M.Sc. Thesis, Department of Chemistry, University of the Western Cape

Characterization of nanophase electrocatalysts, which are an essential part in the direct methanol fuel cell (DMFC) and solid-polymer electrolyte (SPE) electrolyser, have been studied in this work. Their nanoparticulate size raises significant challenges in the analytical techniques used in their structural and chemical characterization. Hence, the applicability of analytical protocols for the qualitative and quantitative characterization of structural and chemical properties of nanophase platinum and platinum-ruthenium electrocatalysts was investigated. Also, fabricated carbon-supported platinum, platinum-ruthenium, iridium oxide, and mesoporous silica-templated platinum electrocatalysts were screened on the basis of their electrocatalytic activity.

A set of structural and chemical parameters influencing the performance of nanophase electrocatalysts was identified. Parameters included crystallinity, particle size, particle size distribution, agglomeration, aggregation, surface area, thermal stability, chemical speciation, electrocatalytic activity, and electrochemically-active

surface area. A large range of analytical tools were employed in characterizing the electrocatalysts of interest.

High accuracy and precision in the quantitative and qualitative structural characterization of nanophase electrocatalysts, collected by x-ray diffractometry and transmission electron microscopy, was demonstrated.

Selected-area electron diffraction was limited to a rapid qualitative evaluation of electrocatalyst polycrystallinity and crystal symmetry.

Scanning electron microscopy was limited to the qualitative evaluation of the agglomeration state of supported electrocatalysts.

High-performance particle sizing was unable to resolve the particle size of the electrocatalyst from that of the support and was therefore employed in the quantitative investigation of aggregate size and size distribution in supported electrocatalysts. The technique produced high precision data illustrating the reproducibility of the aggregate size data.

N₂-physisorption produced surface area and pore size distribution data of high quality, but was unable to determine surface areas specific to the metal phase in supported electrocatalysts. The technique was deemed inconsistent in the accurate determination of average pore size.

The resolution of scanning electrochemical microscopy and proton-induced x-ray emission spectroscopy (SECM) did not allow for an investigation of characteristics at the nanoscale. Quantitative chemical information was difficult to extract from SECM maps and the technique was limited to the qualitative characterization of surface topography.

Thermogravimetry was suitable for the qualitative investigation of the thermal stability of the nanophase electrocatalysts of interest.

In this study, temperature-programmed reduction was able to qualitatively speciate the surface chemical state and investigate the strength of the metal-support interaction in supported nanophase electrocatalysts.

Cyclic voltammetry and linear-sweep voltammetry were employed in the electrochemical characterization of nanophase electrocatalysts and both qualitative and quantitative information were obtained. The techniques were able to discriminate between various commercial and fabricated electrocatalysts and identify new highly-active materials. Preparation variables could be critically evaluated for the fabrication of cost-effective highly-active nanophase electrocatalysts.

Certain techniques were deemed to be highly applicable in discriminating between high and low activity nanophase electrocatalysts based on their structural and chemical properties. The electrocatalyst characterization strategy and methodology was developed and will be implemented for future characterization of nanophase electrocatalysts.

November 2005

ACKNOWLEDGEMENTS

- Almighty God for the opportunities he has provided me and for always helping me through those difficult dark hours.
- Greatest thanks and gratitude to my parents, Mr. I.J. Williams and Mrs. P.W. Williams, for always supporting and encouraging me in achieving my goals. This work would not be possible without your influence and guidance.
- Prof. V.M. Linkov, Dr. L. Khotseng, and the staff of the South African Institute for Advanced Materials Chemistry for allowing me to conduct the research.
- Huge thanks and gratitude to Mrs. L. Petrik and Dr. A. Nechaev for their insight into thesis writing and for always helping me through the difficult times.
- Z. Godongwana, Q. Ying, X. Wang, T. Thamahane, (SAIAMC), and L. Cele (University of Johannesburg) for fabricated nanophase electrocatalysts and supports.
- Dr. B. Julies (Electron Microscopy Unit, Department of Physics, University of the Western Cape) and Dr. G. Malgas – Scanning Electron Microscopy, Transmission Electron Microscopy; Selected-Area Electron Diffraction.
- Dr. C.A. Pineda-Vargas (Materials Research Group, iThemba Labs) – Proton-Induced X-ray Emission Spectroscopy.
- The financial assistance of the National Research Foundation (NRF) towards this research is hereby acknowledged. Opinions expressed and conclusions arrived at, are those of the author and are not necessarily to be attributed to the NRF.
- The German Academic Exchange Service (DAAD) for their financial support.

TABLE OF CONTENTS

Declaration	i
Synopsis	ii
Acknowledgements	v
Abbreviations	xii

CHAPTER 1 INTRODUCTION: MOTIVATION AND OBJECTIVES OF

THE STUDY **1**

1.1. BACKGROUND TO FUEL CELL TECHNOLOGY	1
1.2. HYDROGEN PRODUCTION AND WATER ELECTROLYSIS	2
1.3. RATIONALE TO THE INVESTIGATION	3
1.4. REFINEMENT OF RESEARCH	5
1.5. RESEARCH AREA AND HYPOTHESIS	5
1.6. RESEARCH FRAMEWORK AND DESIGN	6
1.7. DELIMITATIONS OF THE INVESTIGATION	6
1.8. INVESTIGATION OUTLINE	7

CHAPTER 2 LITERATURE REVIEW: NANOPHASE ELECTROCATALYSTS IN THE DIRECT METHANOL FUEL CELL AND SOLID- POLYMER ELECTROLYTE ELECTROLYSER **10**

2.1. BOUNDARIES OF THE LITERATURE REVIEW	10
2.2. KEY CONCEPTS	11
2.3. PHYSICO-CHEMICAL PROPERTIES AND GENERAL PRINCIPLES IN THE PREPARATION OF NANOPHASE ELECTROCATALYSTS	13
2.3.1. Structure of Nanomaterials	13

Table of Contents

2.3.2. Electrocatalytic Application of Nanomaterials	15
2.3.3. General Principles in the Preparation of Supported Nanophase Electrocatalysts	16
2.3.3.1. <i>Support Materials</i>	16
2.3.3.2. <i>Metal-Support Interactions</i>	18
2.3.3.3. <i>Nanophase Electrocatalyst Preparation</i>	19
2.4. ROLE OF PHYSICO-CHEMICAL AND ELECTROCHEMICAL CHARACTERIZATION OF NANOPHASE ELECTROCATALYSTS	20
2.5. NANOPHASE ELECTROCATALYSTS FOR ELECTRODE PROCESSES IN THE DIRECT METHANOL FUEL CELL	26
2.5.1. Nanophase Electrocatalysts in the Methanol Oxidation Reaction	26
2.5.2. Nanophase Electrocatalysts in the Oxygen Reduction Reaction	29
2.6. NANOPHASE ELECTROCATALYSTS FOR ELECTRODE PROCESSES IN THE SOLID-POLYMER ELECTROLYTE ELECTROLYSER	31
2.6.1. Nanophase Electrocatalysts in the Oxygen Evolution Reaction	31
2.6.2. Nanophase Electrocatalysts in the Hydrogen Evolution Reaction	33
2.7. CONCLUSIONS OF THE LITERATURE REVIEW	35
2.8. EXPERIMENTAL TASKS	36

CHAPTER 3 METHODOLOGY	38
3.1 MATERIALS AND METHODS	38
3.1.1. Materials	38
3.1.2. Methods of Synthesis	39
3.2 LIMITATIONS IN THE CHARACTERIZATION OF NANOPHASE ELECTROCATALYSTS	42
3.3. STRUCTURAL CHARACTERIZATION OF NANOPHASE ELECTROCATALYSTS	43
3.3.1. X-ray Diffractometry	43
3.3.2 Selected-Area Electron Diffraction	45
3.3.3. Scanning Electron Microscopy	46
3.3.4. Transmission Electron Microscopy	47
3.3.5. Aggregate Size Analysis by Dynamic Light Scattering	48
3.3.6. Surface Area and Porosity Determination by N ₂ Physisorption	49
3.3.7. Proton-Induced X-Ray Emission Spectroscopy	50
3.4. THERMAL CHARACTERIZATION OF NANOPHASE ELECTROCATALYSTS BY THERMAL ANALYSIS	52
3.5. CHEMISORPTIVE SPECIATION OF NANOPHASE ELECTROCATALYSTS BY TEMPERATURE- PROGRAMMED REDUCTION	53
3.6. ELECTROCHEMICAL CHARACTERIZATION USING CYCLIC AND LINEAR-SWEEP VOLTAMMETRY	55
3.7. SCANNING ELECTROCHEMICAL MICROSCOPY	60
3.8. OVERVIEW OF MAIN POINTS	62

CHAPTER 4 RESULTS AND DISCUSSION: STRUCTURAL, THERMAL, AND CHEMISORPTIVE CHARACTERIZATION OF NANOPHASE ELECTROCATALYSTS	65
4.1. STRUCTURAL CHARACTERIZATION OF NANOPHASE ELECTROCATALYSTS	65
4.1.1. Crystallinity, Symmetry, and Particle Sizing of Nanophase Electrocatalysts	65
4.1.2. Agglomeration and Aggregation of Supported Nanophase Electrocatalysts	72
4.1.3. Metal Particle Size and Metal Particle Size Distribution of Supported Nanophase Electrocatalysts	76
4.1.4. Determination of Surface Area and Porosity of Supported Nanophase Electrocatalysts	79
4.2. THERMAL AND CHEMISORPTIVE CHARACTERIZATION OF SUPPORTED NANOPHASE ELECTROCATALYSTS	85
4.2.1. Thermal Stability of Nanophase Electrocatalysts	85
4.2.2. Chemisorptive Speciation of Nanophase Electrocatalysts	88
4.3. SUMMARY OF MAIN RESULTS	91
CHAPTER 5 RESULTS AND DISCUSSION: ELECTROCHEMICAL CHARACTERIZATION OF NANOPHASE ELECTROCATALYSTS	97
5.1. ESTABLISHING A TESTING PROTOCOL FOR THE ELECTROCHEMICAL CHARACTERIZATION OF NANOPHASE ELECTROCATALYSTS	97

Table of Contents

5.1.1. Experimental Setup	98
5.1.2. Modelling the Solid-Polymer Electrolyte	99
5.1.3. Electrocatalyst Cast-Film Application	99
5.1.4. Topography of Nanophase Electrocatalyst Cast-Films	102
5.1.5. Influence of Methanol Concentration on the Methanol Oxidation Reaction	107
5.1.6. Influence of Nafion [®] Content on Electrocatalytic Activity	108
5.1.7. Influence of Oxygen Saturation on the Oxygen Reduction Reaction	110
5.2. ELECTROCHEMICAL CHARACTERIZATION OF NANOPHASE ELECTROCATALYSTS	111
5.2.1. Dilute Acid Electrolysis	111
5.2.2. Electrochemical Screening of Nanophase Electrocatalysts in Potassium Ferrocyanide	114
5.2.3. Electrochemical Characterization of Nanophase Electrocatalysts in the Methanol Oxidation Reaction	118
5.2.4. Electrochemical Characterization of Nanophase Electrocatalysts in the Oxygen Reduction Reaction	124

Table of Contents

5.2.5	Electrochemical Characterization of Nanophase Electrocatalysts in the Oxygen Evolution Reaction	128
5.2.6.	Electrochemical Characterization of Nanophase Electrocatalysts in the Hydrogen Evolution Reaction	129
5.2.7.	Electrochemically-Active Surface Area of Platinum- Based Nanophase Electrocatalysts	134
5.3.	SUMMARY OF MAIN RESULTS	137
CHAPTER 6 CONCLUSIONS AND RECOMMENDATIONS		142
REFERENCES		148
APPENDICES		



ABBREVIATIONS

BET	Brunauer-Emmett-Teller
BJH	Barrett-Joyner-Halenda
CV	Cyclic Voltammetry
DMFC	Direct Methanol Fuel Cell
HER	Hydrogen Evolution Reaction
HMS	Hexagonal Mesoporous Silica
HPPS	High-Performance Particle Sizing
HOPG	Highly Oriented Pyrolytic Graphite
H _{UPD}	Hydrogen Underpotential Deposition
JM Pt/C	Commercial Johnson Matthey™ Carbon Black-Supported Nanophase Platinum
JM PtRu/C	Commercial Johnson Matthey™ Carbon Black-Supported Nanophase Platinum-Ruthenium
LPG	Liquefied-Petroleum Gas
LSV	Linear-Sweep Voltammetry
MOR	Methanol Oxidation Reaction
OER	Oxygen Evolution Reaction
ORR	Oxygen Reduction Reaction
PIXE	Proton-Induced X-ray Emission Spectroscopy
Pt/C	Carbon Black-Supported Nanophase Platinum
Pt/CNT	Carbon Nanotube-Supported Nanophase Platinum
PtRu/C	Carbon Black-Supported Nanophase Platinum-Ruthenium
RDE	Rotating-Disk Electrode

Abbreviations

SAED	Selected-Area Electron Diffraction
SCE	Saturated Calomel Electrode
SECM	Scanning Electrochemical Microscopy
SEM	Scanning Electron Microscopy
SHE	Standard Hydrogen Electrode
SPE-electrolyser	Solid-Polymer Electrolyte Electrolyser
TEM	Transmission Electron Microscopy
TGA	Thermogravimetric Analysis
TPR	Temperature-Programmed Reduction
UME	Ultra-Micro Electrode
XRD	X-ray Diffractometry
CA	Carbon Analogue
d_{hkl}	Inter-planar Spacing
a_0	Lattice Parameter
$SA_{Pt/C}$	Platinum Metal Surface Area
i_{PA}	Anodic Peak Current
i_{PC}	Cathodic Peak Current
j_{PA}	Anodic Peak Current Density
j_{PC}	Cathodic Peak Current Density
E_{PA}	Anodic Peak Potential
E_{PC}	Cathodic Peak Potential
ΔE_P	Peak Separation
E^0	Formal Potential
Q_{H^+}	Charge Associated with a Hydride Monolayer

CHAPTER 1

INTRODUCTION: MOTIVATION AND OBJECTIVES OF THE STUDY

1.1. BACKGROUND TO FUEL CELL TECHNOLOGY

The 21st century marks the beginning of an energy revolution which is steadily gaining momentum and will have a great impact on modern civilization. Energy production will shift from fossil fuel combustion to sustainable energies which are safer, cleaner, and more efficient. These sustainable energies should provide an energy security due to their inexhaustible fuel stocks as well as their environmental compatibility. At the forefront of sustainable energies is fuel cell technology, which is an attractive form of energy production which would be able to satisfy the growing energy demand when fully developed. Fuel cells are simply electrochemical devices which convert chemical energy into electrical energy. They may lead to a revolutionary improvement in energy production and could soon become the next true world economy, having an impact similar to the current oil and petroleum markets. Fuel cells for commercial energy production are economically feasible and less expensive materials and fuels are being developed for more efficient energy production. Attributes of fuel cells which make their use advantageous are:

- Cheap fuels which are easy to store, transport, and distribute
- High selectivity
- Good mechanical properties
- High power densities
- Low temperature operation
- Environmentally-friendly due to low harmful emissions as their operation involves a full chemical reaction and no combustion processes
- They are not constrained thermodynamically and are therefore highly efficient in extracting energy from fuels

Fuels cells are envisaged for use in the automotive industry where they may replace the internal combustion engine; in the military as a portable power source; and to provide electricity to rural areas not connected to a national electricity supply.

A large range of fuel cells are available, each incorporating different membranes and electrode materials and utilizing different fuels. Most attractive is the direct methanol fuel cell (DMFC) due to its high power densities and ease of fuel distribution. In addition, existing petroleum distribution facilities could be retained for the distribution of DMFC electrode fuels with minimum modification.

1.2. HYDROGEN PRODUCTION AND WATER ELECTROLYSIS

“I believe that water will one day be employed as fuel, that hydrogen and oxygen which constitute it, used singly or together, will furnish an inexhaustible source of heat and light, of an intensity of which coal is not capable. I believe then that when the deposits of coal are exhausted, we shall heat and warm ourselves with water. Water will be the coal of the future.” Jules Verne (1874) "L'île mystérieuse" (The Mysterious Island).

UNIVERSITY of the
WESTERN CAPE

This is the prediction of Jules Verne (1828-1905), renowned French writer and pioneer of modern science fiction, whose most well-known works include “*Twenty Thousand Leagues under the Sea*” (1870) and “*Around the World in Eighty Days*” (1873). Unbeknownst to Verne, his ideas on water as fuel are a fitting reality and a future energy source envisaged for implementation in the 21st century.

Hydrogen (H₂) may serve as an energy storage medium that could be safely manufactured and distributed. It constitutes about 90% of the known universe, making it an endless supply of energy. Interestingly, burning H₂ produces more heat-per-gram than any other fuel currently available making the use of H₂ even more attractive in energy production and storage.

Among many routes of H₂ production including the steam-reforming process and the water-gas reaction, water electrolysis is the most practical route due to its simplicity; convenience; and absence of carbon monoxide as a by-product. H₂ produced by water electrolysis, in a solid-polymer electrolyte (SPE) electrolyser, can be recombined with O₂ in a proton-exchange membrane fuel cell to produce energy and harmless emissions. Although the advantages of H₂ power are endless, high costs associated with electrocatalysis of the SPE-electrolyser hamper commercialisation of this technology, hence its limited application in industry.

1.3. RATIONALE TO THE INVESTIGATION

The DMFC and SPE-electrolyser currently find limited application in industry and are not readily available to the average consumer. The problem lies in developing fuel cells and electrolysers that maintain their high performance, yet are more affordable. High costs are due to expensive electrocatalysts and membranes required in their operation. Reducing material costs is imperative for future commercialisation of fuel cell technology, hence the dedicated research drive in electrocatalyst development and characterization. To enhance performance and reduce operating costs, electrocatalyst particle sizes are decreased to the nanoscale to increase their surface area with the result that materials gain enhanced or entirely new properties. Extensive research has gone into the development of high performance nanophase electrocatalysts to improve the efficiency of fuel cells. To further enhance catalytic performance to commercially feasible standards important physical and chemical properties of nanophase electrocatalysts should be identified, characterized, and modified. Also, with cheaper and potentially higher performance nanophase electrocatalysts currently being fabricated using novel preparation techniques so the characterization of physico-chemical properties and electrocatalytic screening of these materials becomes important. This stems from the fact that most engineered nanomaterials have a functionality based on their physico-chemistry. Application of

these newly-fabricated nanophase electrocatalysts cannot be achieved without a fundamental understanding of the properties they exhibit or may potentially exhibit.

Fabricated electrocatalysts should have physico-chemical properties of a similar or enhanced nature compared to currently-employed commercial electrocatalysts to be considered for future application in fuel cells and electrolyzers. It is therefore important to establish a physico-chemical standard by which newly fabricated nanophase electrocatalysts should be screened. These standards or benchmarks can be established by the physico-chemical characterization of the commercial nanophase electrocatalysts currently used in the DMFC and SPE-electrolyser.

Importantly, the characterization of nanophase electrocatalysts raises significant challenges about identifying the analytical tools and fundamental methods used in their investigation. Moreover, past approaches and methods used in characterising nanophase electrocatalysts has led to mostly inconsistent results. This inconsistency indicates the need for standardised tests in order to obtain comparable results. The identification of a set of characterization criteria and techniques presents challenges to characterization studies. This is because it is impractical, albeit laudable, to characterise every property of nanophase electrocatalysts. Emphasis should therefore be placed on identifying which properties influence the behaviour of nanophase electrocatalysts the most and upon the selection of methods used to study these properties. Ideally, a minimum set of characterization properties and techniques are considered essential.

The necessity for a detailed standard characterization protocol cannot be overstated. The characterization study ultimately forms the starting point of an envisaged materials cost-reduction. It is with this in mind that the applicability of standard protocols for the characterization and screening of currently-used and prospectively-used nanophase electrocatalysts was investigated.

1.4. REFINEMENT OF RESEARCH

The characterization study was initiated by familiarization with DMFC, water electrolysis, and SPE-electrolyser technologies and their corresponding electrode processes through a comprehensive literature review. The literature review then focussed on nanomaterials, and the structural; thermal; and chemical properties of the nanophase electrocatalysts of interest. The minimum set of essential properties of the nanophase electrocatalysts of interest were then identified and reviewed. The research then delved into a review of characterization techniques which are employable in the study to address the set of properties of nanophase electrocatalysts. Lastly, optimisation of techniques; correct sample preparation; and the treatment and interpretation of data received considerable attention.

1.5. RESEARCH AREA AND HYPOTHESIS

The main research areas of the investigation were: the investigation of standard protocols for the characterization of nanophase electrocatalysts; study of physico-chemical properties influencing the electrocatalytic action and electro-activity of nanophase electrocatalysts; and electrochemical screening of fabricated nanophase electrocatalysts.

The problem statement of the investigation can be hypothesized as follows:

Investigating the applicability of standard protocols for the qualitative and quantitative characterization of nanophase electrocatalysts

In investigating the hypothesis the following sub-objectives will be addressed:

- Investigating the structural, thermal, and chemisorptive characterization of commercial carbon-supported nanophase platinum (Pt/C) and platinum-ruthenium (PtRu/C) nanophase electrocatalysts.

-
- Electrochemically screening commercial and fabricated Pt/C, PtRu/C, iridium oxide (IrO₂), mesoporous silica-templated carbon analogues (CA) and carbon nanotube-supported platinum (Pt/CNT) nanophase electrocatalysts.

1.6. RESEARCH FRAMEWORK AND DESIGN

Assumptions formulated in this study are given as follows:

- Nanomaterials exhibit enhanced electrocatalytic activities compared to the corresponding bulk materials.
- The electrocatalytic activities of nanophase electrocatalysts are optimised in the 2-5 nm size domain.
- Support materials are generally accepted as catalytically-inactive.

The perspective of the study encompasses method validation, material science, crystallography, surface chemistry, electrocatalysis, and electrochemistry.

Commercial nanophase electrocatalysts will be characterized in terms of a minimum set of physico-chemical properties using a range of characterization techniques. A testing protocol for the electrochemical characterization and screening of nanophase electrocatalysts will be investigated. Finally, fabricated nanophase electrocatalysts including mesoporous silica-templated carbon analogues; Pt/C; PtRu/C; IrO₂; and Pt/CNT, will be screened on the basis of their electrocatalytic activities towards electrode reactions of the DMFC and SPE-electrolyser.

1.7. DELIMITATIONS OF THE INVESTIGATION

In the current study the following research areas will be investigated:

-
- The structural, thermal, and chemisorptive characterization of commercial Pt/C and PtRu/C nanophase electrocatalysts.
 - The electrochemical characterization of commercial Pt/C, PtRu/C, and IrO₂ nanophase electrocatalysts.
 - Electrochemical screening of fabricated Pt-based carbon analogues templated from mesoporous silica, fabricated Pt/C and PtRu/C; fabricated Pt/CNT; and IrO₂ nanophase electrocatalysts.

In the current study the following research areas will not be investigated:

- The structural, thermal, and chemisorptive characterization of IrO₂-based materials, mesoporous silica-templated carbon analogues, Pt/CNT, and fabricated Pt/C and PtRu/C materials due to time constraints.
- Characterization of ternary and quaternary nanophase electrocatalysts as these materials were not readily available.
- Solid-polymer electrolyte membranes used as proton-conducting media in the DMFC and SPE-electrolyser. The membranes are outside the scope of the investigation.
- Application of current and prospectively-used nanophase electrocatalysts in DMFC and SPE-electrolyser performance testing as it is outside the scope of the investigation.

1.8. INVESTIGATION OUTLINE

Chapter 2: Literature Review: Nanophase Electrocatalysts in the Direct Methanol Fuel Cell and Solid-Polymer Electrolyte Electrolyser

The literature review focuses on a discussion of physico-chemical and electrocatalytic properties of nanomaterials and the general principles in the preparation of nanophase electrocatalysts. This is followed by a

discussion of the role of physico-chemical characterization in nanophase electrocatalysis and the identification of critical properties which govern the behaviour of nanophase electrocatalysts. The chapter is concluded by a detailed discussion of electrode processes in the DMFC and SPE-electrolyser and the application of nanophase electrocatalysts in these processes.

Chapter 3: Methodology

Chapter 3 fundamentally serves as a continuation of the literature review, but with more emphasis placed on the characterization techniques employed in the study. The chapter is initiated with an introduction to the nanophase electrocatalysts and support materials sampled in the study and the methodologies used in their preparation. This is followed by a detailed discussion and literature review of characterization techniques employed in the study and the sample preparations and experimental parameters used. *Chapter 3* gives insight into the type of data which can be extracted and the benefits they provided to the study and also justifies the choice of characterization tools used in the study.

Chapter 4: Results and Discussion: Structural, Thermal, and Chemisorptive Characterization of Nanophase Electrocatalysts

Chapter 4 gives insight into the structural, thermal, and chemisorptive properties of commercial nanophase electrocatalysts. Important structural, thermal, and chemisorptive properties required in future characterization of prospective nanophase electrocatalytic materials were identified and studied. Structural information of the commercial nanophase electrocatalysts will serve as a standard, or benchmark, for

future characterization studies of fabricated nanophase electrocatalysts.

Chapter 5: Results and Discussion: Electrochemical Characterization of Nanophase Electrocatalysts

Chapter 5 opens with the establishment of a testing protocol for the electrochemical characterization and screening of nanophase electrocatalysts currently or potentially used in DMFC and SPE-electrolyser electrode processes. This is followed by an electrochemical characterization of commercial and fabricated Pt/C, PtRu/C, IrO₂ nanophase electrocatalysts, mesoporous silica-templated carbon analogues, and carbon nanotube-supported electrocatalysts.

Chapter 6: Conclusions and Recommendations

The study is concluded with a concise discussion of salient points pertaining to the qualitative and quantitative applicability of the analytical techniques used in characterizing the physico-chemical properties of nanophase electrocatalysts. Recommendations made, anomalies noted, and the larger relevance and implications of the study are discussed.

CHAPTER 2

LITERATURE REVIEW: NANOPHASE ELECTROCATALYSTS IN THE DIRECT METHANOL FUEL CELL AND SOLID-POLYMER ELECTROLYTE ELECTROLYSER

The literature review focuses on a discussion of physico-chemical and electrocatalytic properties of nanomaterials as well as the general principles in the preparation of nanophase electrocatalysts. The role of the characterization study in nanophase electrocatalyst manufacture and application is discussed in detail and the minimum set of physico-chemical properties influencing the behaviour of nanophase electrocatalysts is identified. A detailed discussion of DMFC and SPE-electrolyser electrode processes and the application of nanophase electrocatalysts in these processes follows. In following this approach the problem areas will be introduced, applications of the materials made known, and the minimum set of properties of nanophase electrocatalysts will be identified. The literature review identifies the physico-chemical properties of nanophase electrocatalysts which require investigation before discussing the characterization techniques which can be included in a standard characterization protocol (*Chapter 3*). Once the minimum set of properties for nanophase electrocatalyst characterization was identified, detailed experimental tasks for the study were formulated.

2.1. BOUNDARIES OF THE LITERATURE REVIEW

The literature review will define the term “*nanomaterials*” and discuss physico-chemical properties materials exhibit or potentially exhibit upon decreasing their particle size to the nanometre domain. The literature review will discuss the role of nanomaterials in electrocatalysis, the properties which make nanomaterials favourable in electrocatalysis, and the criteria for the identification of ideal nanophase electrocatalysts. The general theory of supported nanophase electrocatalysts will be

detailed and the general principles in their preparation will be examined. In terms of applications, the theory behind electrode processes in the DMFC and SPE-electrolyser and the applicability of nanophase electrocatalysts in their operation are detailed.

Nanomaterials besides those currently, or potentially, used as nanophase electrocatalysts in the DMFC and SPE-electrolyser will not be discussed as they are outside the scope of the study (i.e. nanowires, nanobelts, etc.). Fuel cells and electrolysers besides the DMFC and SPE-electrolyser, and the electrode processes involved in their operation, will not be discussed. Finally, mechanical features of the DMFC and SPE-electrolyser will not be discussed as it is outside the scope of the investigation. Although multitudes of adequate characterization techniques are known and have been extensively discussed in literature, it should be stated that the literature review, particularly in *Chapter 3*, will only discuss techniques which are readily available for use and address the minimum set of properties of nanophase electrocatalysts stipulated.

2.2. KEY CONCEPTS

- According to the *Cambridge International Dictionary of English* the word “*characterization*” means to describe something by stating its main qualities. It can involve elucidating a variety of aspects of a character such as appearance and behaviour.
- Catalysts facilitate the increase of reaction rates of otherwise slow reactions without being consumed in the reaction itself. This is achieved by lowering the activation energy threshold in the rate-determining step of the reaction. As observed in Figure 2.1, the activation energy threshold of a catalysed reaction (E_{a2}) is distinctively lower than that of an uncatalysed reaction (E_{a1}). As a result,

the reaction rate is increased; products are formed quicker and with greater yields over time, upon the addition of a catalyst [1].

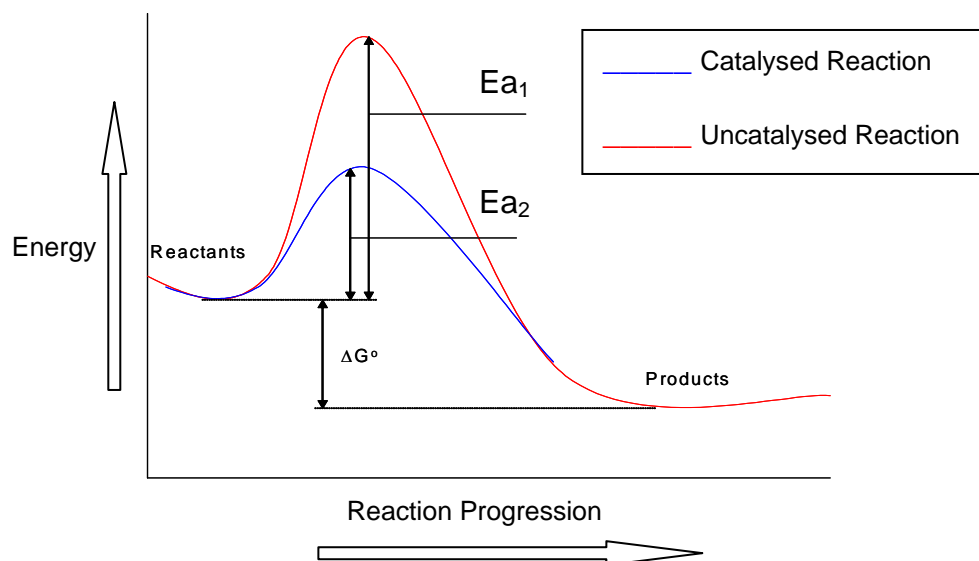


Figure 2.1. Potential-energy curve illustrating the lowering of the activation-energy threshold upon the addition of a catalyst to a generalised reaction [1]

- Heterogeneous catalysis is defined as the use of catalysts which are in a different physical state than the reactant. This type of catalysis involves the transport of reactant species to the catalyst surface where they are chemisorbed. Chemical interaction occurs between surface adsorbates followed by the breaking of chemisorption bonds between adsorbates and the catalyst surface and the liberation of products which are transported away from the catalyst surface [1].
- Electrocatalysis entails increasing the reaction rate and selectivity at electrodes, in electrochemical cells, using materials exhibiting high catalytic activity towards the electrode processes. Electrocatalysts act directly at interfaces by anchoring reagent species to their catalytic centres or active sites. Suitable electrocatalysts have good corrosion stability over extended periods, good electrical conductivity to minimize resistance loss, and low cost [2].

-
- Pt-group metal (PGM) catalysts are typically used in electrocatalysis in the DMFC and SPE electrolyser and reducing the particle size to the nanometre domain can further enhance their catalytic activities.
 - For the purpose of material cost reduction, suitable fabricated nanophase electrocatalysts are usually dispersed on inert conductive support materials.
 - Membrane electrode assemblies are the “heart” of the fuel cell. They consist of two catalyst layers, dispersed on gas-diffusion layers, and are separated by a proton-conducting barrier.

2.3. PHYSICO-CHEMICAL PROPERTIES AND GENERAL PRINCIPLES IN THE PREPARATION OF NANOPHASE ELECTROCATALYSTS

2.3.1. STRUCTURE OF NANOMATERIALS

The nanometre (nm) is a unit of measurement equivalent to one-billionth of a metre or 1×10^{-9} m. Therefore, materials with dimensions in the nanometre domain can be considered *nanomaterials*. More specifically, nanomaterials should have particles or structures with dimensions ≤ 100 nm. The class *nanomaterials* may include nanowires, nanorods and nanotubes, each with their own specific advantages and applications. An example is carbon nanotubes which have tubular structures with diameters 2-30 nm and lengths a few micrometres in size. Carbon nanotubes are principally used as catalyst support and H₂ storage materials. Nanoparticles can be ultrasonically dispersed in liquids, are water insoluble, and the suspension of nanoparticles in air is not easily achievable due to strong cohesion between particles. Nanoparticles with sizes ≥ 10 nm are composed of 10^3 - 10^5 atoms with the majority of these atoms existing on the surface [3]. The keen interest in nanomaterials is the peculiar behaviour of particles as their sizes approach the atomic or Angstrom (Å) domain. When the size of particles is in the 1-100 nm domain it becomes comparable

with the critical length scales of physical phenomena, resulting in size and shape effects. Deviations in behaviour arise when the number of surface atoms becomes comparable to that of the interior of the particle. With decreasing particle size larger numbers of surface atoms can be found, thus increasing the interfacial region where their behaviour differs from that of interior atoms (increasing surface-to-volume ratio) due to higher instability and reactivity. As a result surface atoms dictate the chemical behaviour of nanomaterials. The increase in the surface area-to-volume ratio also increases the surface energy of nanoparticles. This behaviour makes the use of nanophase catalysts in surface-sensitive reactions feasible, where catalytic reactivity is a function of the exposed surface of the catalyst and the interface between the reactant and the catalyst.

Metal nanoparticles are polycrystalline with many crystal facets (Figure 2.2). They possess higher densities of edges, kinks, steps, and defects in their surface structure compared to bulk materials which ultimately influences the deviation in their chemical behaviour. Separating facets are face boundaries which contain atoms of deviated coordination which have different chemical and thermodynamic behaviour from facial atoms due to differences in atomic densities. Therefore, high densities of face boundaries also explain the unique behaviour of metal nanoparticles compared to their corresponding bulk materials [4-6].

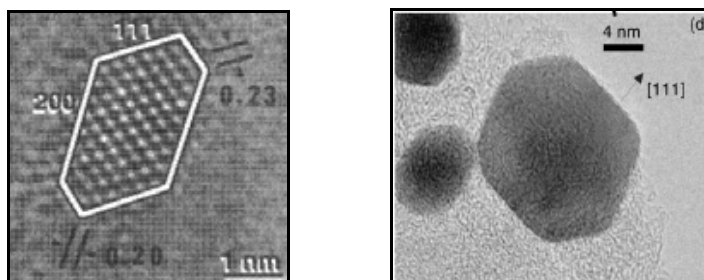


Figure 2.2. Truncation of Pt nanoparticles by (111) and (200) crystal facets

Nanophase metals also exhibit a phenomenon known as *technological polymorphism*, where characteristics of the nanomaterial are dependent on their preparation history. Properties exhibited by materials are enhanced once particles are reduced to the nanoscale or entirely new properties are developed. These properties may include electrical resistance/conductivity, specific heat capacity, thermal expansion, magnetism, lower thermal conductivity, and catalytic activity. Physical properties that may change upon reducing the particle size to the nanoscale include melting point, hardness, and tensile strength and may all stem from a change in the atomic environment of the material. Geometry and electronic structure are also strongly affected by decreasing the particle size. An example of the effect of reducing the particle size to the nanoscale is the decrease in the melting points of metals which can be attributed to the increased surface energy of nanomaterials [5, 7-11].

The unique properties of nanomaterials present an opportunity to use them in novel applications and devices. Phenomena occurring on this length scale are of interest to physicists, chemists, biologists, electrical and mechanical engineers, and computer scientists making research in nanomaterials a frontier activity in materials science. Nanomaterials find considerable use in a wide spectrum of applications and many new applications are currently being developed. Moreover, extensive research in nanomaterial fabrication is primarily conducted in the field of catalysis of industrially-important processes.

2.3.2. ELECTROCATALYTIC APPLICATION OF NANOMATERIALS

Generally in electrocatalysis, the greater the surface area of the material the greater is the decrease in the activation energy threshold and the greater is the catalytic activity. Therefore, high-surface area, highly active materials are sought for enhanced electrocatalysis. Logically, as electrocatalytic activity is a function of the exposed surface area of materials, nanomaterials should induce optimised reaction activity as they possess high surface areas and enlarged surface-to-volume ratios. When

nanomaterials are used in electrocatalytic applications they are termed “*nanophase electrocatalysts*”. High surface area-to-volume nanophase electrocatalysts are extensively employed in electrochemical devices such as fuel cells. Rigorous research is conducted to further increase the active surface area of nanophase electrocatalysts, as well as increasing catalytic efficiency and catalyst utilization [10, 12-14].

Finally, prospective nanophase electrocatalysts should be stable in the environment of the electrochemical cell, where platinum (Pt) has become the standard material among electrochemists, engineers, and parties requiring effective electrocatalysis in acidic environments [15]. Other PGM's have also been used as electrocatalysts in a wide range of electrochemical devices, particularly fuel cells and water electrolyzers.

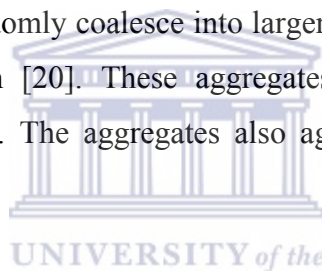
2.3.3. GENERAL PRINCIPLES IN THE PREPARATION OF SUPPORTED NANOPHASE ELECTROCATALYSTS

2.3.3.1. Support Materials

Ideally, electrochemists demand maximum catalytic activity with low catalyst loading so as to reduce material costs. The catalytic activity can be enhanced and electrocatalyst loading lowered by increasing the surface area via high dispersion of nanophase electrocatalysts on inert support materials, such as carbon or metal oxides. The support material should be electro-conductive and stable in the presence of acidic/alkaline electrolytes, reactants, and reaction products [16]. The surface microstructure of the support may also influence the availability of reactant to active surface sites of the catalyst and the removal of reaction products formed at electrocatalyst surfaces. Typical support materials include activated carbon, alumina (Al_2O_3), silica (SiO_2), carbon black, titania (TiO_2), zirconia (ZrO_2), calcium carbonate (CaCO_3), and barium sulphate (BaSO_4). Carbon blacks, such as Vulcan XC-72[®], are typically used to support fuel cell electrocatalysts and offer various advantages including:

- High electrical conductivity
- Good corrosion resistance
- High thermal conductivity and low thermal expansion coefficient.
- Mechanical stability and strength

Carbon black is formed by the thermal decomposition of hydrocarbons and consists of primary carbon particles which are spherical and of colloidal size. These primary particles have sizes between 12-75 nm and surface areas between 25 m²/g and several hundred m²/g, depending on the grade. Jordan *et al* [17] have described Vulcan XC-72[®] as having particle sizes typically 30-50 nm with surface areas ranging 250-300 m²/g. Easton [18] and Li *et al* [19], however, described Vulcan XC-72[®] as having surface areas of 195 m²/g and 237 m²/g, respectively. During formation, primary carbon black particles randomly coalesce into larger branched aggregates which once formed cannot be broken [20]. These aggregates have large densities of voids between primary particles. The aggregates also agglomerate under van der Waals forces between aggregates.



To illustrate the influence of high metal dispersion, it was noted that carbon black-supported nanophase Pt (Pt/C) had specific surface areas of $\pm 60 \text{ m}^2 \cdot \text{g}^{-1}$ compared to unsupported nanophase Pt blacks, which had specific surface areas of $\pm 35 \text{ m}^2 \cdot \text{g}^{-1}$ [13, 21-23]. Notably, Maillard *et al* [24] observed that low catalyst loadings on Vulcan XC-72[®] produced narrow particle size distributions with 10-30% Pt on Vulcan XC-72[®] producing the most homogeneous particle size distributions. Prabhuram *et al* [25] described Vulcan XC-72[®] as producing the largest Pt nanoparticle dispersion on its surface, compared to other commercially available carbon blacks.

Unfortunately, carbon black supports are known to contain impurities which may poison the metal phase. Johnson Matthey[™] [26] also stated that impurities from the support may deactivate the metal catalyst. From an energy-dispersive spectroscopic (EDS) analysis of Vulcan[®] XC-72, it was found that the support contained a trace

quantity of sulphur which was added by the manufacturer to improve durability and life expectancy of the support (Figure 2.3). Cherstiouk *et al* [27] and Holister *et al* [4] suggested that the presence of sulphur may result in difficulties when studying the electrochemical behaviour of supported nanophase electrocatalysts.

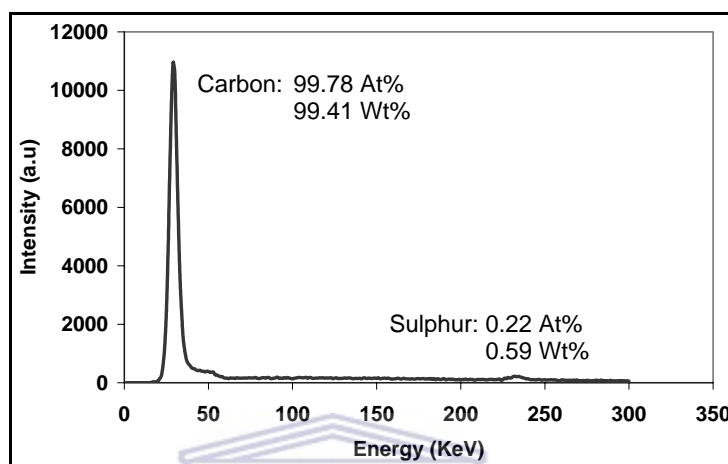


Figure 2.3. Energy-dispersive spectrum (EDS) of Vulcan[®] XC-72

2.3.3.2. Metal-Support Interactions

The interactions between metal nanoparticles and support material particles help determine the electrocatalytic abilities of supported nanophase electrocatalysts as they influence the electrochemically-active surface areas and acid-base properties. Metal-support interactions involve chemical bonding between surface functional groups of the support and that of metal nanoparticles. Carbonyl (-CO) or hydroxyl (-OH) functionalities of the carbon support interact with metal surface atoms to form strong bonds which adhere the electrocatalyst to the support. The nature of the metal-support interaction also influences reactivity, such as in the methanol oxidation reaction (MOR) of the DMFC, where Pt supported on oxidized carbon exhibits higher activities for the MOR than does Pt supported on unoxidized carbon. This is due to the metal-support interaction being governed by the technological polymorphism of the material. The interaction also aids the reduction of MOR overpotential on

Pt [13, 24]. The interaction may also influence surface metal oxidation states, where strong interactions result in high numbers of metal oxidation states on the carbon support surface thus influencing the catalytic activity of the material [13, 28].

2.3.3.3. Nanophase Electrocatalyst Preparation

In terms of nanophase electrocatalyst preparation, multitudes of preparation methods such as inert gas condensation; electro-deposition; electric arc discharge; and ion exchange have been used to prepare nanophase electrocatalysts. Vacuum thermal evaporation in inert gas atmospheres is a standard dry technique while a sol-gel process is a typical wet method. Further, binary nanophase electrocatalysts, such as PtRu, can be prepared by chemical deposition, electrodeposition, sputter deposition, ball-milling, and arc melting [18]. Many researchers also preferred an organometallic route for the preparation of nanophase electrocatalysts involving the synthesis of colloidal precursors. Each preparation has its own advantages and disadvantages, which have been well-documented [9, 13, 18, 24]. Essentially, the determining factor between the techniques, for the selection of a suitable preparation method, is that most of the methods produce nanophase electrocatalysts with different particle size distributions; average particle sizes; and particle dispersions in the case of supported catalysts.

Supported nanophase electrocatalysts for fuel cell applications were best prepared using an impregnation-reduction method, as presented by Zhou *et al* [29, 30]. Firstly, support materials were treated to increase the proton-conductivity of the electrocatalyst by the formation of surface carboxylic acid groups [18, 19]. Support materials such as SiO₂; α -Al₂O₃; MgCl₂; or treated carbon were then suspended and continuously stirred in a pH-buffered colloidal solution containing a metal salt precursor and a suitable solvent. A reducing agent, typically hydrazine; sodium borohydride; or formaldehyde was added at 80-100°C to reduce metal ions from solution onto the support surface. H₂ reduction in a quartz tube furnace could also be

used for the reduction of metal ions. Finally the supported materials were collected by vacuum filtration and dried. This technique produced very small nanoparticles in the size range of 3-7 nm. Unfortunately, it may produce unfavourably wide particle size distributions. The biggest advantages of the impregnation-reduction method are the simplicity of the method and its applicability to the preparation of a large number of supported nanophase electrocatalysts. Advantageously, the metal loading can be controlled by varying the quantity of the metal salt precursor added to the colloidal solution. Also, metal location and metal dispersion can be controlled during preparation. Metal nanoparticles can preferentially be deposited at the exterior surface of the support to produce surface-loaded nanophase catalysts [26]. In contrast, Paulus [31] described the incipient wetness impregnation method as being the preparation technique of choice in commercial supported nanophase electrocatalyst fabrication. This preparation technique is described as impregnation when the volume of the metal precursor was empirically determined as corresponding to a point at which the dry support material appears wet.

Factors determining the reactivity of electrocatalysts depend on the preparation of metal precursors, nature of the supports, metal-support interactions, and surface properties. This dependency is a result of the technological polymorphism of nanoparticles. This said, the choice of metal salts/precursors and preparation conditions affect the dispersion and compositional homogeneity of nanophase catalyst particles [32].

2.4. ROLE OF PHYSICO-CHEMICAL AND ELECTROCHEMICAL CHARACTERIZATION OF NANOPHASE ELECTROCATALYSTS

Current research trends in nanophase electrocatalysts focus mainly on three critical areas: fabrication of new materials, new characterization tools, and new applications. Progress from fabrication to commercialisation is often derailed by the difficulties associated with characterizing nanophase electrocatalysts. This is due to the size of

nanophase electrocatalysts hampering the use of many well-established analytical techniques and fundamental methods. Also, the translation of *nano*-properties to *macro*-properties is still poorly understood. New techniques and approaches must be developed to meet the significant challenges of nanophase electrocatalyst characterization. The elements of a characterization strategy are clear, but the detailed approach requires attention.

As material characterization can sometimes be a tedious and time-consuming operation it is important to identify the minimum set of relevant properties which have an influence on the behaviour of nanophase electrocatalysts.

Physico-chemical properties which may influence nanophase electrocatalyst behaviour include particle size; shape; surface composition; surface area; dispersion; and catalytic activity.

According to the Centre for Nanotechnology at the University of Washington [33], physical properties which require characterization include surface structure, atomic structure, shape, composition, and particle distribution. These properties can be investigated using a multitude of analytical techniques including electron microscopy, dynamic light scattering, scanning probe microscopy, diffractometry, and a large host of spectroscopies.

According to Johnson Matthey™ [26], critical properties of the support material includes the surface area, pore volume, particle size, acid-base properties, and the ability to promote metal-support interactions.

According to Zhang [34], the most important information regarding nanophase electrocatalysts is gathered in an electrochemical characterization study incorporating voltammetry.

Oberdöster *et al* [35] recommended that the following physico-chemical properties be characterized: size distribution; agglomeration state; particle shape; crystal structure; surface area; surface chemistry; and porosity. They also recommended that characterization beyond information given by the suppliers be conducted.

According to Haber [36], the following structural properties require investigation when dealing with supported nanophase electrocatalysts: total surface area, porosity, surface structure, active surface area, and catalytic activity.

In this study the important physico-chemical properties of nanophase electrocatalysts, governing the observed chemical behaviour, which require characterization include:

- crystalline/atomic structure
- crystalline symmetry
- agglomeration/aggregation state
- surface structure
- metal particle size and particle size distribution
- surface area and porosity
- thermal stability
- chemical state at the surface
- electrocatalytic activity
- electrochemically-active surface area

Before these physico-chemical properties can be investigated it is important to define these properties, discuss how they influence the behaviour of supported nanophase electrocatalysts, and generally discuss how they can be characterized.

Crystalline structure can be described as the degree of structural order in a solid and is a measure of the likelihood of atoms or molecules to be arranged in a regular

pattern. According to the International Union of Pure and Applied Chemistry (IUPAC), crystallinity can be described as the presence of a regular three-dimensional order on the atomic level. This atomic order will determine the properties of nanophase electrocatalysts or their deviations from that of the corresponding bulk materials. It can be directly studied using diffraction techniques such as x-ray, electron, or neutron diffraction [37].

Symmetry of crystalline solids, as exhibited by their crystal facets, is due to the ordered internal arrangement of atoms in a crystal lattice. Appearance of symmetry is opposite to crystal distortion and signifies the absence of lattice imperfections in the crystal structure of materials. Crystal symmetry can be monitored by observation of x-ray, electron, or neutron diffraction patterns.

Metal nanoparticles are thermodynamically unstable and have a tendency to agglomerate. Agglomeration entails the attachment of particles at edges or corners. It is described as a number-reducing process which promotes mass-conservation and which increases the particle size distribution. In doing so, agglomeration decreases the particle surface area available for chemical reaction. For this reason, agglomeration is undesired in both the metal phase and the support material in supported nanophase electrocatalysts as the catalytic functions of these materials are dependent on the exposed surface area. Therefore, agglomeration should be characterized and rated in supported nanophase electrocatalysts [38]. Agglomeration can be directly studied using electron microscopic techniques.

Aggregation is a result of van der Waals attractions existing between particles of similar composition. Unfortunately, in the case of carbon black primary particles of the fuel cell electrocatalyst support material the aggregation is irreversible and occurs spontaneously in the manufacturing process. Aggregation alters the volume, particle size, particle size distribution, porosity and surface area of materials. Changes in surface area and volume may influence the chemical reactivity, electro-optical, and

thermal properties of nanophase electrocatalysts [20]. Aggregation can be qualitatively studied using electron microscopy and semi-quantitatively studied using light-scattering techniques.

Surface structure defines the size, shape, and surface features of structured nanophase electrocatalysts. In the case of supported nanophase electrocatalysts it may include the size of metal nanoparticles, the metal particle size distribution, the metal particle shape, and the metal dispersion on support materials. As fuel cell and water electrolysis electrode processes are surface sensitive and exhibit a particle size effect characterization of the metal particle size, metal particle size distribution, metal particle shape, and metal dispersion are of extreme importance for catalytic efficiency. Metal particle size directly affects the metal-support interaction which influences the catalytic activities of supported nanophase catalysts. Metal particle size plays an important role in catalytic efficiency due to the relationship between catalytic activity and surface electronic structure. Metal particle size is influenced by the preparation method (technological polymorphism) and nature of the support material. Increased metal dispersion on the support material and decreased metal particle size generally result in increased catalytic activity. Metal particle size distribution is largely influenced by the metal-support interaction. In addition, very broad metal particle size distributions may lead to inefficient metal utilization. Metal particle size and shape, particle size distribution, and metal dispersion are best studied using a fundamental characterization tool such as electron microscopy [36, 39].

Total surface area is the measure of the exposed surface of a solid on the molecular scale. Total surface area is the sum of the internal and external surface areas of supported catalysts and should be distinguished from each other. External surface area defines the complete boundary surrounding particles, whereas internal surface area defines the boundaries occupied by pore walls and cavities. Surface area is an important property in supported nanophase electrocatalysts as metal dispersion

increases with increasing support surface area [36]. Surface area can best be investigated using gas-adsorption techniques.

Porosity is the fraction of the total volume of a material that is occupied by pores and voids. The pore volume can be described as the total internal volume per unit mass of the material. It is important to determine the pore size and the pore size distribution. The porosity of the support influences the diffusion of reactants and products on the surface and the metal dispersion [36]. Porosity can best be investigated using gas-adsorption techniques.

Thermal stabilities of materials decrease with decreasing particle size which restricts the applicability of nanophase electrocatalysts to low and moderate temperatures. This may be related to the decrease in melting point upon decreasing the particle size to the nanometre domain. Also, differences in the thermal stabilities of materials can be associated with differences in their atomic structures, and higher crystallinity can be associated with higher thermal stability [5, 7-11]. Thermal stability is best investigated using a thermal analysis technique such as thermogravimetry.

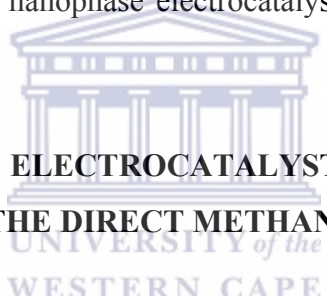
Supported nanophase catalysts may have both reduced and unreduced metal species on their support surfaces. Reactive species at the surface modify the reactivity of supported nanophase electrocatalysts. Therefore the requirement to speciate surface metal species of supported nanophase electrocatalysts. It is important to have knowledge of the chemical state on the surface of supported materials before application. This can be done by a chemical speciation study of the electrocatalyst surface [26]. Nanophase electrocatalysts can be chemically speciated using temperature-programmed techniques.

Catalytic activity can be defined as the rate of chemical change brought about by a catalyst. It can therefore be regarded as a true reflection of the catalytic abilities of nanophase electrocatalysts. In the context of this study, it can best be determined using electro-analytical techniques such as voltammetry [36].

The active surface area can be described as the fraction of the surface area of the active metal phase which participates in a heterogeneous reaction. Active surface area is best determined using electro-analytical methods, which unfortunately are limited by the assumptions of the stoichiometry of the reaction [36].

The properties discussed comprise the minimum set of properties which should be addressed in the characterization of nanophase electrocatalytic materials. Both the structural and electrochemical characterization approaches to the study address the research drive for nanophase electrocatalysts with low metal loadings, highly active surface areas, high metal dispersion, and high catalytic activity.

The analytical tools used in characterizing the identified properties, which influence the chemical behaviour of nanophase electrocatalysts, will be reviewed in detail in *Chapter 3*.

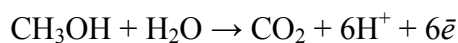


2.5. NANOPHASE ELECTROCATALYSTS FOR ELECTRODE PROCESSES IN THE DIRECT METHANOL FUEL CELL

DMFC operation is comprised of the methanol oxidation reaction (MOR) and oxygen reduction reaction (ORR) at the anode and cathode, respectively. Methanol (CH_3OH) serves as the anode fuel while air serves as the cathode fuel. The anode and cathode electrocatalysts are typically nanophase PtRu on carbon (PtRu/C) and nanophase Pt on carbon (Pt/C), respectively. In Sections 2.5.1 and 2.5.2, the principles of the MOR and the ORR, and the applications of Pt/C and PtRu/C nanophase electrocatalysts in these reactions, are discussed.

2.5.1. NANOPHASE ELECTROCATALYSTS IN THE METHANOL OXIDATION REACTION

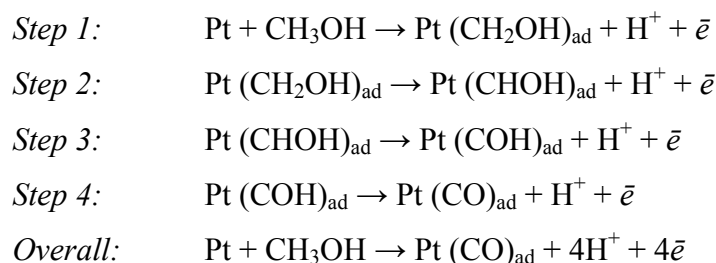
The methanol oxidation reaction (MOR) at the DMFC anode is given as follows:



In this reaction 1 mole methanol reacts with 1 mole water to produce 1 mole carbon dioxide, 6 protons which are transported through the proton-conducting membrane towards the cathode, and 6 electrons which flow through an external circuit. The reaction is slow and requires high overpotential to drive it at industrially-satisfactory rates. CH₃OH is also known to have poor reactivity in acidic media and therefore requires effective electrocatalysis. In acidic media, only Pt-based catalysts are stable enough to dissociate CH₃OH at sufficiently low potentials and at satisfactory rates. This is because Pt-based electrocatalysts have the ability to cleave the C-H bond (dehydrogenation) of CH₃OH by activating the bond itself [40]. The MOR is surface sensitive and is easily influenced by modifications in the surface chemistry of electrocatalysts. For example, the onset potential for the MOR is lowest, with the highest activity, on Pt(111), compared to other crystal facets and is therefore favoured in the MOR [41]. To produce large densities of Pt(111) facets the electrocatalyst should be reduced to the nanometre size range thereby ensuring high reactivity.

The MOR involves two surface processes: the adsorption of methanol fragments after methanol dehydrogenation, and the oxidative removal of surface species after water decomposition.

CH₃OH dehydrogenation and adsorption of molecular fragments proceed stepwise on nanophase Pt/C and is given in the following reaction mechanism:



Four protons and electrons are liberated in the reaction with the formation of Pt surface species. From the mechanism, molecular fragments such as formaldehyde (-HCHO); carbon monoxide (-CO); hydroxymethyl radicals (-CH₂OH[•]); formic acid (-HCOOH) and -COH[•] adsorb onto Pt surface sites [42-44]. The potential window for the process is 0.45-0.9V_{SHE} [45].

The oxidative removal of Pt surface species (i.e. Pt-CO_{ad}) is completed in two sub-steps: firstly the decomposition of water, and secondly the donation of surface-adsorbed hydroxyl groups (-OH_{ad}) by a Langmuir-Hinshelwood mechanism for the formation of CO₂.

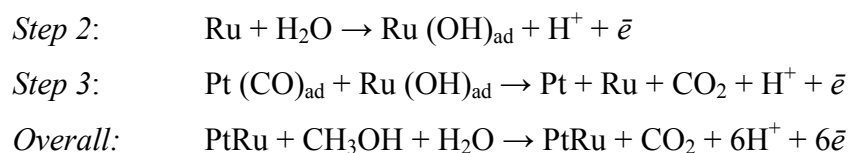
Water decomposition is given as follows, where *M* denotes an active surface site:



Pt cannot effectively remove surface adsorbates under normal DMFC operating conditions due to its low tolerance to accumulative CO_{ad}-poisoning [45]. To reduce the poisoning effect a water decomposition promoter such as ruthenium (Ru) is added to form a binary catalyst [40]. Ru fosters the formation of -OH_{ad} species by water decomposition at low potential without being poisoned and is stable under DMFC operating conditions. In addition, Ru lowers the overpotential for the MOR.

The oxidative removal of Pt surface adsorbates involves a Langmuir-Hinshelwood mechanism. The mechanism involves the chemical interaction between surface adsorbates to form products and incorporates a surface reconstruction upon strong adsorption of -CO_{ad} [46]. An important criterion for the Langmuir-Hinshelwood mechanism to occur between -OH_{ad} and -CO_{ad} is for Pt and Ru surface sites to be adjacent to each other, as is the case in alloys or solid solutions. The full mechanism for the MOR on nanophase PtRu is given as follows:





Step 1 involves dehydrogenation of CH_3OH and the formation of $\text{Pt}(\text{CO})_{\text{ad}}$. In *Step 2*, $-\text{OH}_{\text{ad}}$ species produced by water decomposition are adsorbed to oxophilic Ru surface sites. Finally, in *Step 3* $-\text{CO}_{\text{ad}}$ is oxidized by $-\text{OH}_{\text{ad}}$ following a Langmuir-Hinshelwood mechanism to produce CO_2 , which is evolved from the surface.

In conclusion, ideal MOR electrocatalysts should fulfil the following criteria:

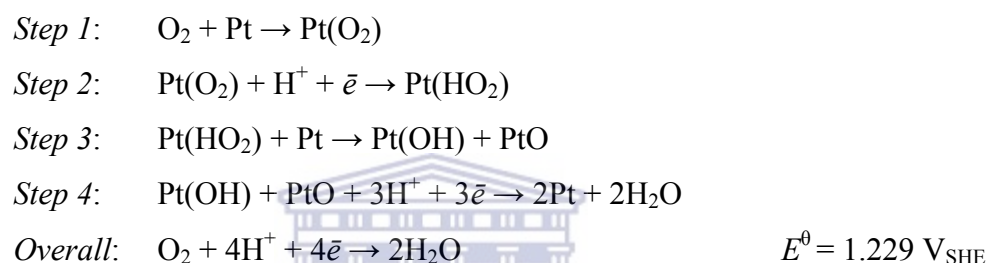
- High Pt content for increased catalytic activity
- Supplementary Ru in catalyst composition for CO-poisoning tolerance
- Pt and Ru particle size reduced to nanoscale to increase surface-to-volume ratio and surface area
- High dispersion of Pt and Ru on inert conductive carbon support materials for increased surface area
- Complete alloying of Pt and Ru on the carbon support surface

2.5.2. NANOPHASE ELECTROCATALYSTS IN THE OXYGEN REDUCTION REACTION

In the oxygen reduction reaction (ORR) the protons that were transported through the proton-conducting membrane, after the MOR at the anode, are combined with O_2 at the cathode to form water. ORR is the reverse reaction of the oxygen evolution reaction. ORR occurs at the cathode of practically all fuel cells and it occurs at the cathode of many corrosion cells. High surface area nanophase Pt/C is typically used as the electrocatalyst at the cathode since theoretically no CO is produced there [2].

The complicated kinetics of the ORR is a limiting factor in the progress of the DMFC. This is due to sluggish reaction rates on noble metals leading to subsequent power and efficiency loss (up to 25% cell voltage loss) in the DMFC. Slow reaction rates on noble metal electrocatalysts are due to the high overpotential associated with these materials, originating from the electron-demand of positively-charged noble metal surfaces for O₂.

ORR on high-surface area nanophase Pt/C occurs by a step-wise reaction mechanism [47]:



In *Step 1*, O₂ adsorbs onto the Pt surface where it dissociates and is hydrated (*Steps 2-3*) to form Pt-hydroxide and Pt-oxide surface species. These surface species interact and recombine in *Step 4* by reduction with H⁺ to form water. The adsorption of O₂ (*Step 1*) onto the nanophase Pt/C surface is the rate-determining step in the ORR.

ORR is a structure sensitive reaction and is known to exhibit a particle size effect on nanophase Pt/C electrocatalysts. This particle size effect plays a vital role in the reaction efficiency, where maximum ORR activity has been observed when Pt particles sizes are 3-4 nm on carbon black supports [48].

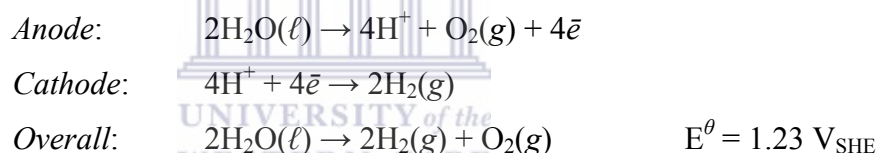
In conclusion, ideal ORR electrocatalysts should fulfil the following criteria:

- Low Pt loadings possibly with the incorporation of Cr, Co, or Fe for high catalytic activity and material cost-reduction

- Pt particle size reduced to nanoscale to increase surface-to-volume ratio and active surface area
- Optimum particle size domain = 3-4 nm for high ORR catalytic activity
- High dispersion of Pt on carbon supports for increased surface area

2.6. NANOPHASE ELECTROCATALYSTS FOR ELECTRODE PROCESSES IN THE SOLID-POLYMER ELECTROLYTE ELECTROLYSER

The major obstacle to the commercialisation of the SPE-electrolyser is the large overpotential associated with the oxygen evolution reaction (OER) at the anode, resulting in high cell voltages. This overpotential can be reduced with the use of high-surface area nanophase iridium oxide electrocatalysts. Half-cell and overall reactions for water electrolysis in the SPE-electrolyser are given as follows [49, 50]:



2.6.1. NANOPHASE ELECTROCATALYSTS IN THE OXYGEN EVOLUTION REACTION

Much of the difficulty experienced in water electrolysis and the SPE-electrolyser can be attributed to the complicated kinetic behaviour and low irreversibility of the oxygen evolution reaction (OER). High surface-area, high activity nanophase electrocatalysts are required to address this shortcoming [51].

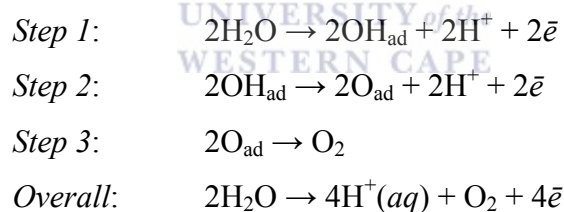
The OER occurs at high positive potentials in 0.5M H₂SO₄. In the OER oxygen, protons, and electrons are produced by the oxidation of hydroxyl (OH⁻) ions or the

oxidation of the water molecules of an aqueous solution [51]. It is the reverse reaction of oxygen reduction.

The anode catalyst of choice is nanophase IrO₂ due to its high catalytic activity, high stability, and high corrosion-resistance in acidic media. IrO₂ also decreases the overpotential for the OER making its application advantageous. Rasten *et al.* [52] found that annealing IrO₂ increases the crystallinity leading to an increase in the electroconductivity and a decrease in the OER electro-activity, with increasing temperature. The best OER activity was found when annealing IrO₂ at 490°C. Thamahane [53] found the best OER activity when annealing IrO₂ at 450°C.

Although electrode material cost-reduction; high surface areas; and lowered catalyst loadings are envisaged, IrO₂ is typically unsupported as a result of the high corrosion of carbon black in the OER reaction in acidic media.

The reaction mechanism for the OER in water electrolysis is given as follows:



In *Steps 1-2* water is decomposed to form surface-adsorbed hydroxide species which are further oxidised to form stable surface oxide species and protons which are transported towards the cathode by the proton-conducting membrane. Finally in *Step 3*, surface oxide adsorbates interact to form O₂ which desorbs from the surface. Cyclic voltammetry can be used in the study of surface oxidation transitions in IrO₂ with increasing oxidation of the oxide layer.

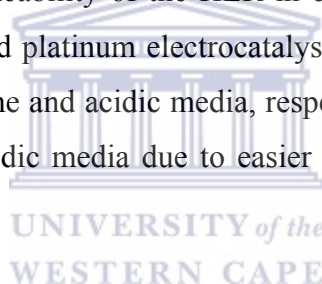
To summarise, ideal OER electrocatalysts should fulfil the following criteria:

- IrO₂ particle size reduced to nanoscale to increase surface-to-volume ratio and active surface area
- IrO₂ unsupported due to the corrosion of carbon under OER conditions
- IrO₂ annealed at high temperatures 450-490°C for optimal OER activity

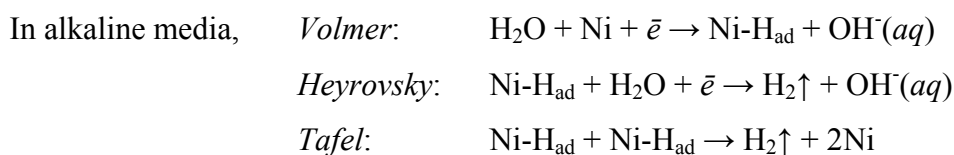
2.6.2. NANOPHASE ELECTROCATALYSTS IN THE HYDROGEN EVOLUTION REACTION

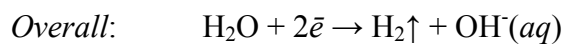
Protons produced in the OER at the SPE-electrolyser anode are transported through the proton-conducting membrane towards the cathode where they are reduced in the hydrogen evolution reaction (HER) to evolve H₂.

Advantageous, is the applicability of the HER in either acidic or basic electrolytes. Also, nanophase nickel and platinum electrocatalysts exhibit high catalytic activities towards the HER in alkaline and acidic media, respectively. However, faster reaction rates were observed in acidic media due to easier evolution of H₂ from hydronium ions, H₃O⁺ [54].

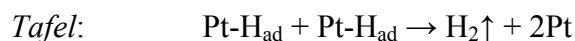
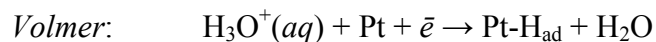


HER occurs via a Volmer-Heyrovsky-Tafel reaction mechanism in which two pathways exist: the Volmer-Heyrovsky and Volmer-Tafel pathways. The Volmer step is an initial electrochemical discharge in which hydride species are formed on surface sites by simultaneous reduction and adsorption of protons. The Heyrovsky step is an electrochemical desorption process in which hydride reduction occurs at surface sites already occupied by hydride species. The Tafel step is a chemical recombination process in which H₂ is evolved via the interaction of adjacent hydride surface species. The Volmer-Heyrovsky-Tafel mechanism can be written as follows [54, 55]:





In acidic media,



In both pathways the Volmer step is the rate-determining step and either pathway can occur depending on reaction conditions and applied potential. They may even occur simultaneously during the reaction. HER generally starts at low negative potentials, depending on electrolyte composition, and continues through large negative potentials. At low negative potential the Volmer-Tafel pathway is favoured, followed by the Volmer-Heyrovsky pathway at large negative potential.

A surface-sensitivity effect is exhibited in the HER, in acidic media, on Pt single crystal facets. HER activities on Pt low-index single crystals have been observed to increase in the order: $\text{Pt}(100) \leq \text{Pt}(111) \leq \text{Pt}(110)$ [54, 56].

To summarise, ideal electrocatalysts for the HER in acidic media should fulfil the following criteria:

- Pt particle size reduced to nanoscale to increase surface-to-volume ratio and active surface area
- High Pt content for increased activity
- High dispersion of nanophase Pt on carbon for decreased loadings and increased surface area
- High densities of low-index Pt(110) and Pt(111) crystal facets for increased reactivity

2.7. CONCLUSIONS OF THE LITERATURE REVIEW

In electrocatalysis high-surface area, highly-active materials are sought. The current research drive is the preparation, characterization, and application of highly-active nanophase electrocatalysts with reduced metal loadings. Nanophase electrocatalysts are prepared by a multitude of techniques. However, the impregnation-reduction method produces particles 3-7 nm in size; is relatively simple to use; large numbers of catalysts can be prepared; and the metal loading can be controlled.

Based on the literature review, the minimum set of physico-chemical properties in supported nanophase electrocatalysts which warrant characterization include:

- Crystalline/atomic structure and symmetry of supported nanophase electrocatalysts
- Agglomeration state, aggregate size, and aggregate size distribution of supported nanophase electrocatalysts
- Surface structure/topography of supported nanophase electrocatalysts
- Metal particle size, metal particle size distribution, and metal dispersion of supported nanophase electrocatalysts
- Total surface area and porosity of supported nanophase electrocatalysts
- Thermal stability of supported nanophase electrocatalysts
- Chemical state of metal nanoparticles on the surface of supported nanophase electrocatalysts
- Electrocatalytic activity of supported and unsupported nanophase electrocatalysts
- Electrochemically-active surface area of supported nanophase electrocatalysts

Ultimately, the electrocatalytic activities determine the applicability of fabricated and commercial supported nanophase electrocatalysts to direct methanol fuel cell and SPE-electrolyser electrode processes.

2.8. EXPERIMENTAL TASKS

Based on the literature review and the minimum set of physico-chemical properties of supported nanophase electrocatalysts for investigation, the following experimental tasks were approached in the study:

- Structural, thermal, and chemisorptive characterization of commercial Pt/C and PtRu/C nanophase electrocatalysts using fundamental characterization techniques (electron microscopy, x-ray diffraction) and more specialised analytical techniques (gas-adsorption, thermal analysis, and temperature-programmed techniques).
- Electrochemical characterization of commercial Pt/C; PtRu/C; and IrO₂ nanophase electrocatalysts using available electro-analytical techniques, such as voltammetry.
- Electrochemical screening of mesoporous silica-templated carbon analogues; carbon nanotube-supported electrocatalysts; and fabricated Pt/C; PtRu/C; and IrO₂ catalysts. The electrocatalytic activities of these fabricated materials should be compared to that measured for the commercial nanophase electrocatalyst used in the study.

The minimum set of physico-chemical properties in the characterization strategy were identified and summarised in the literature review and a detailed experimental approach was designed. The research design and methodologies which address the minimum set of characterization properties of nanophase electrocatalysts, and the

experimental tasks used in their investigation are described in detail in *Chapter 3*. Analytical tools employed in the characterization study are discussed and reviewed in detail in *Chapter 3*. The principles in their operation, sample preparation, and experimental parameters will also be discussed.



CHAPTER 3

METHODOLOGY

The characterization of nanophase electrocatalysts is the logical step after their preparation and prior to their application. The characterization of physico-chemical properties forms the starting point of the optimisation in order to achieve the envisaged cost-reduction and high electrocatalytic performance of nanophase catalysts. The research design therefore makes an important contribution to the investigation of the applicability of standard protocols for the characterization of nanophase electrocatalysts. Various techniques are used as will be further specified.

As was reviewed in *Chapter 2*, the physico-chemical properties of materials change upon decreasing their particle size to the nanometre domain and because of this it becomes important to understand and measure the new or enhanced properties. *Chapter 2* defined the minimum set of properties which governs the behaviour of these materials. The experimental tasks were also set out in *Chapter 2*.

Chapter 3 is dedicated to designing the experimental approach to the characterization of nanophase electrocatalysts. The chapter starts with the introduction of detailed methodologies for the preparation of nanophase electrocatalysts used in the study. This is followed by a detailed literature review and validation of characterization techniques used in the study. Sample preparation and experimental parameters used in the investigation are also detailed.

3.1. MATERIALS AND METHODS

3.1.1. MATERIALS

The materials used in the study and their suppliers are listed in Table 3.1.

Table 3.1. Nanophase electrocatalysts and support materials used in the study

Nanophase Electrocatalyst	Supplier
Vulcan [®] XC-72	Cabot Corporation [™]
Commercial JM Pt/C	Johnson Matthey [™]
Commercial JM Pt ₃₀ Ru ₁₅ /C, Pt ₂₀ Ru ₁₀ /C	Johnson Matthey [™]
Commercial JM IrO ₂	Johnson Matthey [™]
Fabricated HMS-templated carbon analogues	SAIAMC
Fabricated carbon-supported Pt	SAIAMC
Fabricated carbon-supported PtRu	SAIAMC
Fabricated IrO ₂	SAIAMC
Fabricated carbon nanotubes (CNT)	University of Johannesburg

SAIAMC = South African Institute for Advanced Materials Chemistry

3.1.2. METHODS OF SYNTHESIS

Nanophase electrocatalysts and supports used in the investigation were prepared using the methodologies given in the following subsections. All methodologies are fully referenced, but may have been adapted for the purposes of the investigation [53, 57-59].

(i) *Commercial nanophase electrocatalysts*

Johnson Matthey[™] Pt/C, PtRu/C (as Pt₃₀Ru₁₅/C), and IrO₂ commercial fuel cell electrocatalysts served as standardized, well-characterized model materials of known properties in this study. These materials are currently used in methanol oxidation, oxygen reduction, oxygen evolution, and hydrogen evolution in the DMFC and SPE-electrolyser due to their superior electrocatalytic performance. Their use in the study allowed for the evaluation of the applicability of various analytical techniques for the characterization of nanophase electrocatalysts. Their structural properties served as benchmarks against which all fabricated materials could be compared. Reference information obtained for Johnson Matthey[™] catalysts were exclusively of a structural

nature (particle size, lattice parameters, metal surface area) and electrochemical data were not available from the supplier [26]. Cost-effective fabricated nanophase electrocatalysts should ideally exhibit structural properties of a similar or enhanced nature to be considered for application in the DMFC or SPE-electrolyser.

In terms of the electrochemical characterization of nanophase electrocatalysts, all materials were characterized relative to Johnson Matthey™ fuel cell electrocatalysts. Ideally, fabricated nanophase electrocatalysts should exhibit electrocatalytic activities comparable or better than those of the Johnson Matthey™ materials.

Johnson Matthey™ Pt and PtRu fuel cell electrocatalysts were supported on Vulcan® XC-72. Johnson Matthey™ fuel cell electrocatalysts were henceforth denoted as JM Pt/C, JM PtRu/C, and JM IrO₂. The high price of these electrocatalysts warranted the preparation of cost-effective electrocatalysts possessing higher or similar activity.

(ii) Preparation of carbon-supported nanophase Pt electrocatalysts

Carbon-supported nanophase Pt electrocatalysts (Pt/C) were prepared in-house by a method given by Li *et al* [19] and Zhou *et al* [29]. Pt/C was prepared by an impregnation-reduction technique by suspending treated Vulcan® XC-72 in a solvent (glycol/*iso*-propanol), a metal precursor (H₂PtCl₆.6H₂O), and a pH-regulator (H₂SO₄ or NaOH). Pt was deposited onto treated Vulcan® XC-72 supports by formaldehyde reduction. Vulcan® XC-72 was treated prior to the preparation by washing in 2M HCl and oxidising in 5M HNO₃ for 3 hours. Also, a hexagonal mesoporous silica-supported Pt catalyst (Pt/HMS/lpg/pH₂) for the ORR was prepared using the same methodology (Section 5.2.4). These electrocatalysts were prepared as cost-effective materials for use in the ORR at the DMFC cathode and the HER at the SPE-electrolyser cathode. Pt/C electrocatalysts were prepared and structurally characterized by Q.Ying [57].

(iii) Preparation of carbon nanotubes and carbon nanotube-supported nanophase Pt electrocatalysts

Multi-walled carbon nanotubes (CNT) were prepared by a method presented by Pinault *et al* [60]. Multi-walled CNT were prepared by nebulised spray pyrolysis of a ferrocene-toluene (20.00 g/L) solution at 900 °C in a quartz tube reactor. Argon was used as the carrier gas. The nebuliser frequency was 1.6 MHz and the total reaction time was 45 minutes. CNT-supported Pt electrocatalysts were prepared in-house using an impregnation-reduction technique [19, 29]. Firstly, CNT was treated by washing in 2M HCl and oxidised in 5M HNO₃ for 3 hours. The treated CNT was then suspended in 1-propanol, H₂PtCl₆.6H₂O, and H₂SO₄. Pt was deposited onto CNT by formaldehyde reduction. CNT-supported nanophase Pt electrocatalysts were compared to Pt-plated CNT electrocatalysts, prepared using an electroless-plating technique adapted from a patent by Rhoda and Vines [61]. These electrocatalysts were prepared as cost-effective materials for use in the ORR at the DMFC cathode and HER at the SPE-electrolyser cathode. CNT and Pt-plated CNT were prepared by L.Cele of the University of Johannesburg, and CNT-supported Pt electrocatalysts were prepared and structurally characterized by Q.Ying [57].

(iv) Preparation of carbon-supported nanophase PtRu electrocatalysts

Carbon-supported nanophase PtRu electrocatalysts (PtRu/C) were prepared in-house by a method presented by Qin *et al* [30]. PtRu/C was prepared using an impregnation-reduction technique in which H₂PtCl₆.6H₂O, RuCl₃.3H₂O, 25% (v/v) *iso*-propanol/H₂O, and treated Vulcan[®] XC-72 were mixed into a slurry and PtRu nanoparticles were reduced onto the carbon support using formaldehyde at 80 °C for 30 minutes. Vulcan[®] XC-72 was treated prior to synthesis by washing in 2M HCl and oxidising in 5M HNO₃ for 3 hours [29]. These electrocatalysts were prepared as cost-effective materials for use in the MOR at the DMFC anode. PtRu/C electrocatalysts were prepared and structurally characterized by X.Wang [58].

(v) Preparation of nanophase iridium oxide electrocatalysts

Nanophase iridium oxide was prepared in-house by a method presented by Rasten *et al* [52]. IrO₂ was prepared by oxidation of IrCl₃ in a sodium nitrate melt. The solvent was evaporated at 350 °C for 30 minutes and the collected solid was then annealed in a furnace at 450 °C for 4hrs. These electrocatalysts were prepared as cost-effective materials for use in the OER at the SPE-electrolyser anode. Iridium oxide electrocatalysts were prepared and structurally characterized by T.Thamahane [53].

(vi) Preparation of mesoporous silica-templated carbon analogues

Mesoporous silica-templated carbon analogues (CA) were prepared in-house by a method presented by Zhang *et al* [62]. HMS (hexagonal mesoporous silica) was synthesized by the drop-wise addition of tetraethoxysilane to a mixture containing 1-hexadecylamine and an ethanol/water solution. The mixture was filtered, washed, refluxed, dried and the solid finally calcined at 550 °C for 8 hours. The HMS templates were then carbonized using liquefied-petroleum gas (LPG) pyrolysis at 800 °C in a quartz tube furnace followed by methanol/formaldehyde reduction of Pt, from H₂PtCl₆.6H₂O, using an incipient-wetness impregnation technique. The silica supports were finally removed by NaOH etching at 75 °C. These electrocatalysts were prepared for use in the HER at the SPE-electrolyser cathode. Mesoporous silica-templated carbon analogues were prepared and structurally characterized by Z.Godongwana [59].

3.2. LIMITATIONS IN THE CHARACTERIZATION OF NANOPHASE ELECTROCATALYSTS

Fundamental and fairly novel analytical techniques, in a nanophase electrocatalyst characterization context, are not without limitations or restrictions in their resolution or applications. Techniques based on scanning probe microscopy, such as scanning electrochemical microscopy, have sufficient resolution to visualize nanoparticles but

are only able to image the surface and not the interior. They also suffer from difficulties associated in extracting chemical information from images. Their use in material characterization studies is therefore limited to a qualitative nature.

Electron microscopy may allow for the imaging of nanophase electrocatalysts, but suffers from the time taken in statistical sampling of data, preparation artefacts, and the destructive nature of these techniques.

In terms of XRD particle sizing, the use of the Scherrer equation may lead to inconsistencies in particle sizing data. This is due to the Scherrer equation being developed for spherical particles, whereas many metal nanoparticles are cubo-octahedral in shape.

3.3. STRUCTURAL CHARACTERIZATION OF NANOPHASE ELECTROCATALYSTS

3.3.1. X-RAY DIFFRACTOMETRY

X-ray diffractometry (XRD) is a powerful tool in the study of crystallinity and atomic structure of materials and forms an integral part in a comprehensive characterization study of nanophase electrocatalysts. It is widely considered the gold-standard in material characterization studies. It is used extensively in the determination of Bravais lattice types and unit cell dimensions. The dimensions of x-ray wavelengths are in the same order as nanoparticle sizes, hence its application in this study. For the purposes of this study XRD was used in the investigation of crystal/atomic structure, particle size, and lattice parameters. In addition, metal surface area of Pt catalysts (SA_{Pt}) could be determined using particle sizes obtained via XRD. SA_{Pt} was calculated using an equation presented by Prabhuram *et al* [25] and is given as:

$$SA_{Pt} = 6000 / [(d)(\rho)]$$

Where d = density of Pt (21.4 g/cm³); and ρ = particle diameter (nm).

Pt nanoparticles are polycrystalline and anisotropic. These properties necessitate a crystallographic study of Pt-based electrocatalysts. XRD allows for the study of crystal anisotropy and the correlation between structural features and observed chemical properties [1]. The pivotal role XRD plays in the structural characterization of nanophase electrocatalysts cannot be overstated. No comprehensive materials characterization study is complete without an XRD investigation and information gained from XRD analysis can be used in conjunction with chemical information to establish a structure-chemical relationship in surface sensitive reactions.

In XRD, crystalline solids are bombarded with a collimated x-ray beam which causes crystal planes atoms, serving as diffraction gratings, to diffract x-rays in numerous angles. Each set of crystal planes (hkl) with inter-planar spacing (d_{hkl}) can give rise to diffraction at only one angle. The diffractions are defined from Bragg's Law ($n\lambda = 2d \sin \theta$), where the intensities of diffracted x-rays are measured and plotted against corresponding Bragg angles (2θ) to produce a diffractogram. The intensities of diffraction peaks are proportional to the densities or abundance of the corresponding crystal facets in the material lattice. Diffractograms are unique for different materials and can therefore qualitatively be used in material identification. XRD can also be used quantitatively for the determination of average particle size by use of the Scherrer equation, given as:

$$D = 0.9\lambda / \beta \cos \theta$$

where D = particle size, 0.9 = shape factor; λ = x-ray wavelength, β = peak-width at half peak-height (radians); θ = angle of reflection [63-66].

Lattice parameters (a_0) could also be calculated using the following equation:

$$a_0 = d [(h^2 + k^2 + l^2)]^{1/2}$$

Where h , k , and l constitute the Miller indices of a crystal facet, and d is the interplanar spacing determined using Braggs' Law.

In the XRD analysis, dry nanophase electrocatalyst samples were mounted in plastic sample holders and the surface was flattened to allow maximum x-rays exposure. Experimental parameters for the XRD analysis are given as follows:

X-ray Diffractometer:	Bruker AXS D8 Advance
Tube:	Copper
Detector:	Sodium Iodide
Monochromator:	Graphite
Generator operation:	40 kV and 40 mA
Electron Intensity (kV)	40
X-ray source	Cu K_{α} ($\lambda = 1.5418 \text{ \AA}$)
Current (mA)	30
Scan range ($2\theta^{\circ}$):	5-100
Scan rate ($^{\circ}/\text{min}$)	0.05

3.3.2. SELECTED-AREA ELECTRON DIFFRACTION

Selected-area electron diffraction (SAED) can be used in the qualitative measure of crystallinity and symmetry in materials. In this investigation, SAED was limited to a rapid qualitative measure of the crystallinity and symmetry of commercial nanophase electrocatalysts. In SAED, electrons are scattered by electric fields associated with atoms in thin sample films. Diffraction patterns produced give single-crystal diffractive contributions from multitudes of crystallographic facets. In addition, highly polycrystalline materials may display concentric Debye-Scherrer rings in the pattern. The appearance of the diffraction pattern is dependent on the crystallinity of the sample material and may become more complex as the degree of polycrystallinity increases. Also, amorphous materials result in patterns that are diffused, or blurry.

Sample grids from the transmission electron microscopic (TEM) analysis were retained for SAED analysis. The SAED pattern was obtained using a spot analysis with a TEM (Hitachi H-800 EM) and patterns were recorded on photographic film.

3.3.3. SCANNING ELECTRON MICROSCOPY

Scanning electron microscopy (SEM) is a versatile imaging technique capable of producing three-dimensional profiles of material surfaces. SEM is used in this study to extract quantitative and qualitative information pertaining to agglomerate size/shape, particle morphology, and surface appearance of supported nanophase electrocatalysts.

The basic operation in SEM entails the interaction of an accelerated highly mono-energetic electron beam, originating from a cathode filament, with the atoms at a sample surface. The electron beam is focused into a fine probe which is rastered over the sample surface. The scattered electrons are collected by a detector, modulated, and amplified to produce an exact reconstruction of the sample surface and particle profile [27, 67-71].

The nanophase electrocatalysts of interest were supported on double-sided conductive carbon tape and mounted on a sample stub. No sputter-coating was required as all the nanophase electrocatalysts in the study were electron-conductive. Samples were fitted into the vacuum chamber of the microscope (Hitachi X-650 EM and LEO S440). Parameters for the SEM analysis are given as follows:

Working distance (mm):	15
Accelerating gun filament:	Tungsten
Filament current (μA):	75-80
Accelerating voltage (KeV):	25

3.3.4. TRANSMISSION ELECTRON MICROSCOPY

Transmission electron microscopy (TEM) probes the internal structure of solids and gives access to micro-structural detail. In nanophase electrocatalyst characterization studies, TEM is almost exclusively used in the investigation of average particle size, particle shape, and particle size distribution of supported nanophase electrocatalysts. In this investigation, TEM was utilized in the direct examination of metal nanoparticle size; nanoparticle size distribution; homogeneity of dispersion; and agglomeration of the metal phase in supported nanophase electrocatalysts. Further structural information including the number of atoms constituting particles and the metal surface area (SA_{Pt}) could be formulated using TEM data. The metal surface area was obtained using an equation presented by Prabhuram *et al* [25] and is given as: $SA_{Pt} = 6000 / [(d) (\rho)]$, where d = density of Pt (21.4 g/cm^3); and ρ = particle diameter (nm).

In TEM operation, a narrow electron beam originating from a tungsten filament is concentrated onto ultra-thin sample surfaces using a series of magnetic lenses. The electrons interact with sample atoms while penetrating the thin sample structure leading to the transmittance of electrons and the production of secondary electrons. Secondary electrons pass through an aperture to produce an image on a fluorescent screen. For carbon-supported metal electrocatalysts, metal particles appear as dark areas and low atomic weight carbon supports appear as light areas in the resultant micrographs due to differences in electron transmittance with increasing atomic weight [27, 48, 72-80]. The obtained information is often complemented by quantitative information such as total surface area and porosity.

TEM samples were prepared by dispersion of a spatula-tip of the catalyst of interest in 5ml methanol solution, followed by sonication of the suspension. One drop of the suspension was deposited on a carbon/Formvar[®] film-coated copper grid. The methanol was allowed to evaporate at room temperature. Samples were mounted in a

sample holder, which was introduced directly into the shaft of the microscope (LEO EM 912 and Hitachi H-800 EM). Experimental parameters are given as follows:

Accelerating voltage (kV):	200
Current (μA):	20
Condenser aperture:	1
Objective aperture:	3
Exposure time (seconds)	3

3.3.5. AGGREGATE SIZE ANALYSIS BY DYNAMIC LIGHT SCATTERING

Near-nanoscale particle sizing is achievable using dynamic light scattering in a high performance particle size analyser (HPPS). In this investigation, near-nanoscale particle size analysis of nanophase electrocatalyst aggregates could be conducted using the dynamic light scattering technique. These aggregates constituted the smallest units into which the carbon supports could be separated, as primary carbon particles cannot be separated after manufacture [20]. The technique could also be used to determine the aggregate size distribution, but not that of the individual supported electrocatalyst.

The technique entails the measurement of the Brownian motion of nanoparticles, using laser-irradiation, while they are suspended in a suitable dispersant. The measurement was then correlated to the average size of the sample particles by relating the speed of particle motion, in the dispersant, to light scattering. Scattering phenomena for a specific material is unique for its size [36].

Samples were dispersed in a suitable dispersant, which was first filtered to remove dust particles, at a concentration of 0.1 mg/L and sonicated for 30 minutes to break agglomerates into aggregates. Approximately 2 cm³ of the sample dispersion was pipetted into a sample cuvette which was then loaded into the high performance

particle size analyser (Malvern Instruments). All measurements were conducted at 25 °C. Refractive indices of dispersants were gathered using an Abbé refractometer. Calibration was conducted prior to each analysis using a 200 nm sized latex calibration standard.

3.3.6. SURFACE AREA AND POROSITY DETERMINATION BY N₂ PHYSISORPTION

Haber [36] stated that the Brunauer-Emmett-Teller (BET) method, in gas-adsorption, was best suited for the determination of total surface area and porosity of catalysts. In this investigation the surface area and porosity of supported nanophase electrocatalysts could be determined with high sensitivity using an accelerated surface area and porosity analyser (Micromeritics ASAP 2010). This information can be used to demonstrate how the surface microstructure, surface area, and porosity may affect the reactivity of catalysts and the distribution of reagents and products on the catalyst surface. The technique is particularly useful when the surface morphologies of materials are unknown [81, 82].

The accelerated surface area and porosity analyser consisted of a mercury manometer; gas-tight burette, thermostat; liquid N₂-cooled Dewar flask, and a high-vacuum oil pump. High pressures and cryogenic temperatures are used to increase the adsorption rate onto solid surfaces [83].

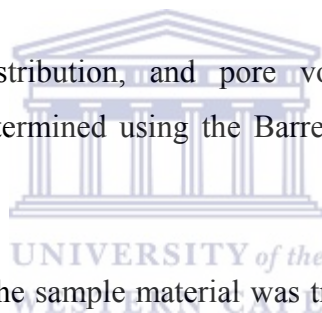
In the basic operation, solid samples are placed in an evacuated sample holder at constant temperature ≈ 110 °C. The sample holder is filled with helium to flush contaminating gases from the sample surface and pores. The helium is then purged from the system. Evacuated samples are cooled to -196 °C in a liquid N₂ bath while the sample holder is filled with ultra-pure N₂ gas. Pressure within the sample holder is monitored over time, and then rapidly reduced to reach an equilibrium state where the quantity of gas adsorbed onto the surface is equivalent to the quantity of gas

removed from the gas phase. By plotting the quantity of N₂ adsorbed versus the equilibrium pressure an adsorption isotherm is obtained, which together with the BET equation can be used to determine the sample surface area. This adsorption isotherm can be defined as the plot of the dependence of the fractional coverage of surface-adsorbed molecules on pressure, at constant temperature [84-86]. The BET equation can be given as follows:

$$\frac{1}{W[(P_0/P) - 1]} = \frac{1}{W_m C} + \frac{(C-1)}{W_m C} \frac{P}{P_0}$$

Where W is the weight of N₂ adsorbed at a given relative pressure (P/P₀), W_m is the weight of gas producing monolayer coverage, and C is a constant related to the heat of adsorption.

Pore size, pore size distribution, and pore volume of supported nanophase electrocatalysts can be determined using the Barrett-Joyner-Halenda (BJH) method [83].



Approximately 20 mg of the sample material was transferred and sealed in a sample tube. Calibration with a silica-alumina standard was conducted prior to analysis.

3.3.7. PROTON-INDUCED X-RAY EMISSION SPECTROSCOPY

While energy dispersive spectroscopy (EDS) is able to investigate the relative surface elemental composition of a given sample, proton-induced x-ray emission spectroscopy (*micro*-PIXE) has the ability to determine elemental distributions of a multitude of elements over large sample areas. *Micro*-PIXE is a trace analytical technique capable of yielding both qualitative and quantitative information non-destructively and without chemical separation. This is achieved by the detection of characteristic x-rays emitted by a sample surface upon bombardment with accelerated protons originating from a nuclear microprobe and a particle accelerator.

Using dynamic analysis, images yielding information pertaining to the chemical composition and elemental distribution of a sample surface can be constructed. An advantageous feature of *micro*-PIXE is the ability to study samples of unknown compositions. The technique has very low detection limits (1 ppm observed upon bombardment with 2-3 MeV protons) and large amounts of sample matrices are not necessary as 2-3 MeV beams have the ability to sample layers less than 75 μm thick [87-90].

Micro-PIXE, in this investigation, is used in mapping the surface elemental distribution on electrocatalyst cast-films supported on HOPG, which are identical to the cast-films studied in scanning electrochemical microscopy and cyclic voltammetry. The technique could potentially be used to map the surface elemental distribution on DMFC and SPE-electrolyser electrodes prior to their incorporation into a membrane electrode assembly.

Samples were mounted into a sample holder and loaded into the *micro*-PIXE spectrometer. After a Rutherford Backscattering Spectroscopic (RBS) analysis of cast-film thickness the surface composition was studied by dynamic analysis. Experimental parameters for *micro*-PIXE analysis of electrocatalyst cast-films are given as follows:

Sample area (m^2):	1×10^{-6}
Proton accelerating velocity (MeV):	3
Proton probe resolution (mm):	3
Total charge collected (mC):	1
Number of pixels:	128 x 128
X-ray analysis line:	L-shell

3.4. THERMAL CHARACTERIZATION OF NANOPHASE ELECTROCATALYSTS BY THERMAL ANALYSIS

Thermal analysis monitors the properties of materials as they change with temperature. Important thermodynamic, kinetic, and physical properties, including thermal stability, can be monitored using thermal analysis. In this investigation the thermal stability of supported nanophase electrocatalysts was studied using thermal analysis.

Thermal characterization of nanophase electrocatalysts was conducted using thermogravimetry (TGA). TGA involves the continuous weighing of solids, using a thermo-balance, while they are heated at a constant rate. Samples are generally heated in inert environments and undergo increases in kinetic motion resulting in physical and chemical changes which result in the thermal decomposition of solids to form products that are detectable. The output signal is a thermogram which is a plot of weight loss, or change in weight, as a function of increasing temperature. Weight loss or changes in weight may be credited to thermal events such as phase transition, melting, volatilisation, thermal decomposition, sublimation, oxidation, or dehydration. Information on thermal decomposition stages, sample composition, and thermal stability range of products can be obtained using TGA.

In terms of the microstructure of carbon-supported catalysts, structural defects and porosity have pronounced influences on thermal behaviour. In addition, the morphology of nanomaterials leads to thermal behaviour that deviates from that of bulk materials. This deviation is manifested in a detectable particle-size effect in TGA. Thermal decomposition temperatures of solids decrease with a decrease in particle size due to a relationship where thermal conductivity increases with a decrease in particle size. Typical thermograms for carbonaceous solids have three distinct regions. Firstly, is the evaporation of surface moisture; secondly, the

evaporation of volatile adsorbed molecules from micropores, and lastly the thermal decomposition of the carbon matrix [91-95].

TGA was conducted using a simultaneous thermal analyzer (Rheometric Scientific STA 1500) and a N₂ atmosphere. Samples were ramped from ambient to 850 °C at a 15 °C/min heating rate. Sample weights were kept to a minimum.

3.5. CHEMISORPTIVE SPECIATION OF NANOPHASE ELECTROCATALYSTS BY TEMPERATURE-PROGRAMMED REDUCTION

Chemisorption is a strong chemical interaction between solid surfaces and gaseous adsorbates where electrons are shared between active surface sites and adsorbates to form strong chemical bonds [83]. Chemisorptive analysis allows for the characterization of nanophase electrocatalysts under working conditions. The basic principle involves the detection of changes to the thermal conductivity of a known gas mixture after flowing through a heated sample. Information gathered includes reduction temperature, number of oxidation states, acidity/basicity, strength, and type of active sites on catalytic surfaces [96].

Temperature-programmed reduction (TPR) uses the reducing properties of catalysts to speciate metal oxidation states and evaluate stability and catalytic ability. Its technical simplicity and high analytical sensitivity is advantageous, making it a powerful tool in the characterization of nanophase electrocatalysts [97, 98]. The degree of reduction might be related to reactivity, where greater reducibility is indicative of higher reactivity. TPR also gives insight into the metal-support interactions of supported materials, where the reduction temperature is dependent on the strength of this interaction, with stronger interactions yielding higher reduction temperatures [99]. In this investigation, TPR is used to speciate the number of oxidation states, evaluate the catalytic ability in terms of reduction temperature, and

investigate the strength of the metal-support interactions in supported nanophase electrocatalysts.

Basic operation in TPR involves purging a sample vessel, containing a solid sample, with argon while heating to remove organic surface adsorbates. The sample is then saturated with a mixture of 10% H₂ in argon at 25°C. The sample temperature is then ramped at a slow rate while the H₂ consumption, by adsorption to the sample surface, is simultaneously monitored. The general reaction mechanism is given as follows:



Changes in the thermal conductivity of the gas stream are detected by a thermal conductivity detector (TCD) and the output signal is a plot of H₂ consumption reported against temperature.

For Pt-based catalysts, two distinct phases are observed (Figure 3.1): Pt⁴⁺ (as PtO₂) as a highly-active phase with reduction to PtO occurring below 0 °C; and Pt²⁺ (as PtO) as the dominant phase with reduction to Pt occurring above 100 °C [100].

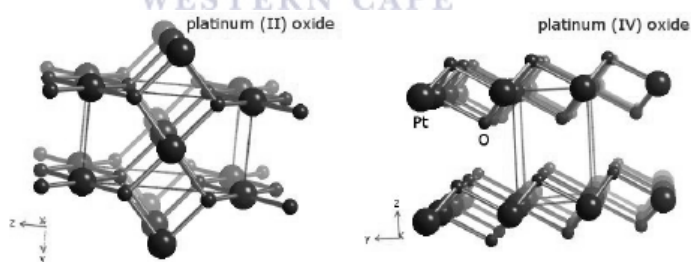


Figure 3.1. Wirework structure of Pt²⁺ (as body-centred tetragonal PtO) and Pt⁴⁺ (as tetragonal PtO₂) oxides

All TPR analyses were conducted using a Micromeritics Autochem 2910 analyser. 20-30 mg sample was weighed and sealed in a sample tube. The cold-trap was cooled to -20 °C using an acetone/dry ice slurry. The sample tube was cooled to -80 °C using an *iso*-propanol/liquid-N₂ cold-gel. Experimental parameters are given as follows:

Temperature ramp (°C):	-80 to 900
Ramp rate (°C.min ⁻¹):	15
Preparation gas:	Argon
Analysis gas:	10% H ₂ in Argon
Flow rate (ml.min ⁻¹):	50

The instrument was calibrated prior to the analysis using a silver oxide standard.

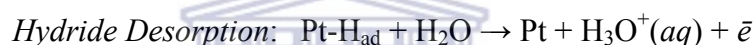
3.6. ELECTROCHEMICAL CHARACTERIZATION USING CYCLIC AND LINEAR-SWEEP VOLTAMMETRY

Cyclic voltammetry (CV) can be used in the study of electrode surface reactions, the behaviour of electrochemically-active species, and to investigate the quality of electrocatalysts. CV provides information on the thermodynamics of redox processes and the kinetics of heterogeneous electron-transfer reactions. It plays an integral role in a comprehensive characterization of nanophase electrocatalysts. CV can be used advantageously to probe surface reactions *in-situ* under well-controlled conditions, giving insight into the catalytic mechanisms and the catalytic activity of nanophase electrocatalysts [40, 101].

CV entails cycling a potential applied to an electrode immersed in a quiescent electrolyte solution, containing an analyte species, through a defined potential range and measuring the resultant current. The measured current is a result of electron flow through the electrochemical circuit and is due to diffusional mass transfer of electro-active species as migration and convection are minimised. The applied potential is swept back and forth between two designated potentials, at a constant rate, by a potentiostat. Typically, a three-electrode system consisting of a working electrode, reference electrode, and counter electrode is used. The working electrode is the electrode of interest at which potential is applied. The reference electrode experiences zero current and has a known standard potential against which all other potentials are

measured. The counter electrode completes the circuit and is usually Pt wire, graphite, or glassy carbon [40]. The output signal is called a voltammogram which represents a plot of current in amperes, versus potential in volts.

CV was also used in the determination of the electrochemically-active surface area of carbon-supported nanophase Pt electrocatalysts. The method required the hydrogen underpotential deposition (H_{upd}) region in the electrolysis of dilute acid on Pt. The H_{upd} region corresponds to Pt-hydride monolayer formation and removal near the reversible H_2 potential ($0.0 V_{\text{SHE}}$). The H_{upd} region consists of cathodic hydride adsorption and anodic hydride desorption surface reactions, which can generally be given as follows (Figure 5.12):



The hydride desorption peaks (Figure 5.12) were integrated to yield a charge (Q_{H^+}), which was used to calculate the electrochemically-active surface area. The approach was based on the assumption that a complete monolayer corresponded to a surface charge of $210 \mu\text{C}/\text{cm}^2$ [102].

Mass transfer is related to the movement of ions in solutions. Mass transfer in the quiescent electrolytes used in cyclic and linear voltammetric experiments is due to diffusion. Diffusion describes the mass transfer due to the random motion of ions and results from a gradient in the electrochemical potential [103]. The diffusion coefficient can be described a proportionality constant which relates the flux of ions to a concentration gradient and can be related to the availability of a reagent species to the surface reaction [104].

The Randles-Sevcik equation can be used in determining the diffusion coefficient (D) of an analyte on an electrode surface and predicts that measured peak currents,

extracted from cyclic voltammograms, are proportional to the square root of the sweep rate applied. The equation can be given as follows [105]:

$$i_p = 0.4463 nFAC (nFvD/RT)^{1/2}$$

Where: n = number of electrons v = sweep rate ($V.s^{-1}$)
 F = Faradays' constant ($96485 C.mol^{-1}$) A = electrode area (cm^2)
 R = universal gas constant ($8.314 J.mol^{-1}.K$) T = temperature (K)
 D = diffusion coefficient (cm^2/sec)

The peak currents from a series of voltammograms were recorded at increasing sweep rates. A plot of peak current versus the square root of the sweep rate was prepared and a linear least squares analysis of the data was performed to determine the slope. The slope and the Randles-Sevcik equation were then used to estimate the diffusion coefficient.

Formal potentials ($E^{0'}$) of catalysts are related to the potentials of electrochemical cell reactions and are simply the average between the anodic (E_{PA}) and cathodic peak potentials (E_{PC}). E_{PA} and E_{PC} can be measured directly using cyclic voltammetry. The equation for the calculation of formal potentials is given as [106]:

$$E^{0'} = (E_{PA} + E_{PC})/2$$

Linear-sweep voltammetry (LSV) involves the application of a single excitation signal to the working electrode. Simply, the applied potential is swept at a fixed sweep rate from an initial potential to an end potential. Unlike CV, the potential is not swept back to the initial potential, but the single excitation signal is repeated from the initial potential to the end potential.

In this investigation, CV and LSV were used to study the electrocatalytic activity of nanophase electrocatalysts and the electrocatalytic action of electrocatalysts towards

DMFC and SPE electrolyser electrode processes. CV and LSV experiments on nanophase electrocatalysts were conducted at 25 °C. Generally all experiments were run for 10-20 measurements. Electrochemical experimental parameters are given as follows:

Voltammetric assembly:	Metrohm
Potentiostat:	Eco-Chemie Autolab PGSTAT 30
Working electrodes:	Glassy Carbon and Pt (surface area = 0.07 cm ²)
Reference electrode:	Saturated Calomel (SCE)
Counter electrode:	Platinum-wire basket

All methodologies for the electrochemical characterization of electrocatalysts were similar to that stated by Liu, *et al* [107]. Glassy carbon and Pt working electrodes were polished prior to ink deposition using 0.05 and 0.1 μm alumina (Al₂O₃) pastes. Cast-film electrodes were prepared by depositing 10-μl electrocatalyst ink volumes onto a glassy carbon disk electrode and drying at 60°C, similar to the methodology used by Prabhuram *et al* [25]. In the determination of electrochemically-active surface areas 25-μl of the ink was deposited on a glassy carbon electrode.

Ink and electrolyte preparations for the electrochemical characterization are given in Table 3.2. All electrolyte and supporting electrolyte solutions were prepared using deionised water (17 MΩ, Millipore®).

Table 3.2. Ink and electrolyte preparation methods used in the study

<i>Experiment</i>	<i>Electrolyte</i>	<i>Supporting electrolyte</i>	<i>Deaeration (30 minutes)</i>	<i>Saturation (30 minutes)</i>	<i>Catalyst mass-loading (%)</i>	<i>Technique</i>
Electrocatalytic activity	0.01M K ₄ [Fe(CN) ₆]	0.1M KCl	-	-	70	CV
MOR activity	0.5M H ₂ SO ₄ + 1M CH ₃ OH	-	N ₂ (AR)	-	86	CV
ORR activity	0.5M H ₂ SO ₄	-	-	O ₂ (AR)	86	CV
OER activity	0.5M H ₂ SO ₄	-	-	-	63	CV
HER activity	0.5M H ₂ SO ₄	-	N ₂ (AR)	-	70	LSV
Active surface area	1M H ₂ SO ₄	-	-	-	86	CV

Intermediate electrocatalyst mass-loading (70%) inks were prepared by suspending 0.02g of the electrocatalyst in 4ml ethanol with the drop-wise addition of 200µl 5% Nafion[®] solution. Inks were sonicated for 30 minutes to form a homogeneous mixture. This procedure was similar to that used by Prabhuram *et al* [25]. This type of ink was used where only small amounts of electrocatalysts were available.

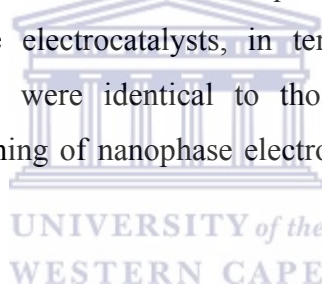
Low electrocatalyst mass-loading (63%) inks were prepared by mixing 0.05g electrocatalyst; 125 µl deionised water; 250 µl *iso*-propanol; and 0.6 g 5% Nafion[®] solution. The inks were allowed to stir mechanically overnight. This type of ink was similar to that prepared by Rasten *et al* [52] for the study of the oxygen evolution reaction on nanophase IrO₂.

High electrocatalyst mass-loading (86%) inks were prepared by suspending 0.21g electrocatalyst in 1g deionised water with drop-wise addition of 0.67g 5% Nafion[®] solution. Inks were agitated to homogeneity using overnight magnetic stirring. This type of ink was similar to the ink composition used in the preparation of fuel cell electrodes and was used where large amounts of catalysts were available.

High electrocatalyst mass-loading (86%) inks for determination of electrochemically-active surface area were prepared by suspending 0.005g electrocatalyst in 1g deionised water with drop-wise addition of 0.016g 5% Nafion[®] solution. The inks were sonicated for 30 minutes to obtain a homogeneous mixture.

3.7. SCANNING ELECTROCHEMICAL MICROSCOPY

Scanning electrochemical microscopy (SECM) is a versatile *in-situ* analytical technique able to simultaneously visualize surface activity and topography by directly probing solid-liquid interfaces. It is also employed to perform voltammetric analyses and determine electron-conductivity of sample surfaces. The technique has been widely used to study the electro-activity and permeability of membranous materials. In this investigation, SECM was used to qualitatively characterize cast-films, prepared from nanophase electrocatalysts, in terms of topography and surface activity. These cast-films were identical to those used in the electrochemical characterization and screening of nanophase electrocatalysts, by cyclic voltammetry [108-112].



The SECM instrument consists of a bipotentiostat which applies potential to two working electrodes in an electrochemical cell: a substrate supporting the sample, and an ultra-microelectrode (UME). The electrochemical cell also contains a reference and counter electrode. The UME is probed over the substrate surface by x , y , z translation motors. The instrument is enclosed inside a Faraday cage to block external electrical fields, due to the sensitivity of the UME.

In the *imaging mode* of SECM, current at the UME (Figure 3.2) is measured upon application of a polarization potential on both the UME and the cast-film [124]. The UME rasters, or probes at close proximity, over the cast-film surface immersed in an electrolyte solution while monitoring variations in the UME tip current [114-118]. Imaging is conducted using the diffusion-controlled cycling of a probe redox couple

between the UME and the substrate. As the UME rasters over the cast-film surface a hemispherical diffusion of the electro-active species towards the UME tip perturbs the tip current at infinite distance ($I_{T\infty}$). The current perturbation is a function of tip-substrate separation and this relationship can be used to gather information regarding the surface profile and activity. Three- or two-dimensional representations of the cast-film surface, and its activity, are ultimately produced [119, 120].

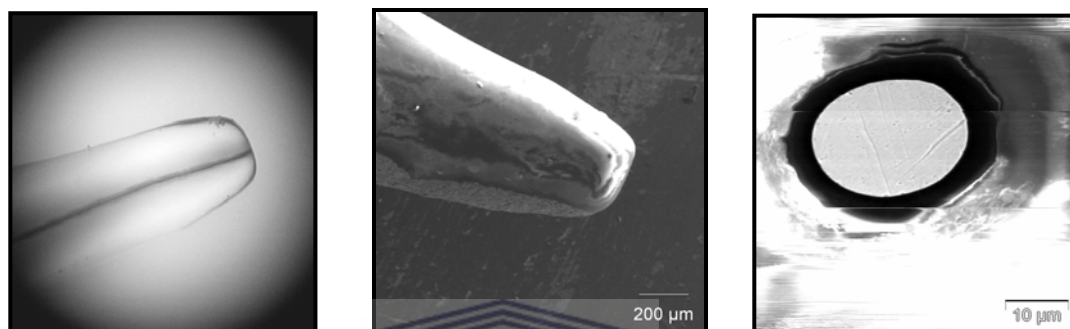


**Figure 3.2. Self-fabricated ultramicro-electrode (UME) construction
(Disk-diameter, $\text{\O} = 25 \mu\text{m}$)**

The *approach-curve* mode in SECM is used to study the electro-conductivity of cast-films or membranes and is conducted prior to imaging. Ideally, the cycling is accompanied by an increase in the UME tip current (I_T), relative to $I_{T\infty}$, leading to an effect known as positive-feedback. This positive-feedback is indicative of electron-conductive materials, making the imaging process feasible. In negative-feedback, a decrease is observed in I_T , relative to $I_{T\infty}$, and is indicative of materials of an insulating nature.

Voltammetric analysis in SECM can be conducted on cast-films and membranous materials. The UME allows for the measurement of very small currents and kinetically fast heterogeneous reactions under diffusion-controlled conditions, with the result that reactions with high mass-transfer rates can easily be studied.

The topography of electrocatalyst cast-films were studied using a Uniscan Instruments SECM 270. Cast-films were prepared according to the methodology given in Section 3.6, and were supported on HOPG. Cast-film topography was studied in 5mM H₂SO₄ electrolyte solution, which allowed for higher measured feedback currents [121]. The reference and counter electrodes were Ag/AgCl and Pt-wire coil, respectively. Mapping was conducted at a constant raster speed of 5 μm/sec, and a tip-substrate separation of 5 μm.

UME were fabricated by sealing 10 mm lengths of Pt micro-wire (Ø = 25 μm) in evacuated borosilicate glass capillary tubes. The end of the tube was then polished, using diamond emery paper and alumina pastes, to produce a fine truncated tip with an exposed Pt disk (Figure 3.2). UME were characterized in 0.02M K₄[Fe(CN)₆] supported in 0.2M KCl. The potential range was scanned between -0.5 V_{Ag/AgCl} and 0.8 V_{Ag/AgCl} at a sweep rate of 20 mV.s⁻¹.

3.8 OVERVIEW OF MAIN POINTS

Characterization studies were initiated by the investigation of structural properties using the fundamental characterization techniques, namely scanning and transmission electron microscopy and x-ray diffractometry. A range of other analytical techniques were utilised in the investigation for the characterization of nanophase electrocatalysts. These analytical tools addressed the minimum set of physico-chemical properties identified in the literature review. Structural and chemical information and the characterization techniques used in their determination can be summarised as follows:

- Crystal/atomic structure and metal particle size of nanophase electrocatalysts can qualitatively and quantitatively be studied using XRD.
- Crystallinity and crystal symmetry of nanophase electrocatalysts can qualitatively be studied using SAED.

- Topography, surface micro- and macrostructure, and the degree of agglomeration of supported nanophase electrocatalysts can qualitatively be studied using SEM.
- Aggregate size and aggregate size distribution of nanophase electrocatalysts can qualitatively and quantitatively be studied using HPPS.
- Metal particle size, particle size distribution, metal surface area, and metal dispersion/agglomeration on supported nanophase electrocatalysts can qualitatively and quantitatively be studied using TEM.
- Total surface area and porosity of supported nanophase electrocatalysts can quantitatively be studied using N₂-physisorption.
- Topography and surface elemental distribution of electrocatalyst cast-films can qualitatively be studied using PIXE.
- Topography and surface activity of electrocatalyst cast-films can qualitatively be studied using SECM.
- Thermal stability of nanophase electrocatalysts can quantitatively be studied using TGA.
- Surface oxidized species (metal chemical state) of nanophase electrocatalysts can qualitatively be studied using TPR.
- Electrocatalytic activity and electrochemically active surface area of nanophase electrocatalysts can quantitatively be studied using CV and LSV.

Methodologies for the preparation of nanophase Pt/C, PtRu/C, IrO₂, CNT, CNT-supported Pt, HMS-supported materials, and carbon analogues were described in *Chapter 3*. Also, ink formulations for the fabrication of cast-film electrodes in the electrochemical study were detailed.

The minimum set of nanophase electrocatalyst properties and experimental tasks were identified and formulated after a literature review in *Chapter 2*. The methodology detailed in *Chapter 3* addressed the approach by which the minimum set of properties of nanophase electrocatalysts would be characterized. The results of

the experimental tasks that were conducted for evaluating the characterization tools discussed in *Chapter 3* are presented in *Chapters 4* and *5*.



CHAPTER 4

RESULTS AND DISCUSSION: STRUCTURAL, THERMAL, AND CHEMISORPTIVE CHARACTERIZATION OF NANOPHASE ELECTROCATALYSTS

In this chapter the structural, thermal, and chemisorptive characterization of nanophase electrocatalysts will be investigated. The investigation was initiated by a structural, thermal, and chemisorptive characterization study of commercial JM Pt/C and JM PtRu/C nanophase electrocatalysts that can be employed in the DMFC and SPE-electrolyser. This chapter evaluates the investigation of structural properties of such electrocatalysts using the experimental tasks formulated in the literature review of *Chapter 2*, and the methodologies given in *Chapter 3*.

4.1. STRUCTURAL CHARACTERIZATION OF NANOPHASE ELECTROCATALYSTS

The structural characterization of nanophase electrocatalysts was conducted by following the experimental tasks formulated in Section 3.8. Unless specified, the commercial JM Pt₄₀/C and JM Pt₃₀Ru₁₅/C electrocatalysts were used in the study.

4.1.1. CRYSTALLINITY, SYMMETRY, AND PARTICLE SIZING OF NANOPHASE ELECTROCATALYSTS

The crystallinity and particle size of JM Pt/C and JM PtRu/C electrocatalysts were determined using XRD, following the procedure given in Section 3.3.1. Vulcan[®] XC-72 was analysed in order to isolate observations unique to Pt and PtRu nanoparticles, both of which were supported on Vulcan[®] XC-72 carbon. The corresponding diffractograms for JM Pt/C, JM PtRu/C, and Vulcan[®] XC-72 are presented in Figure 4.1.

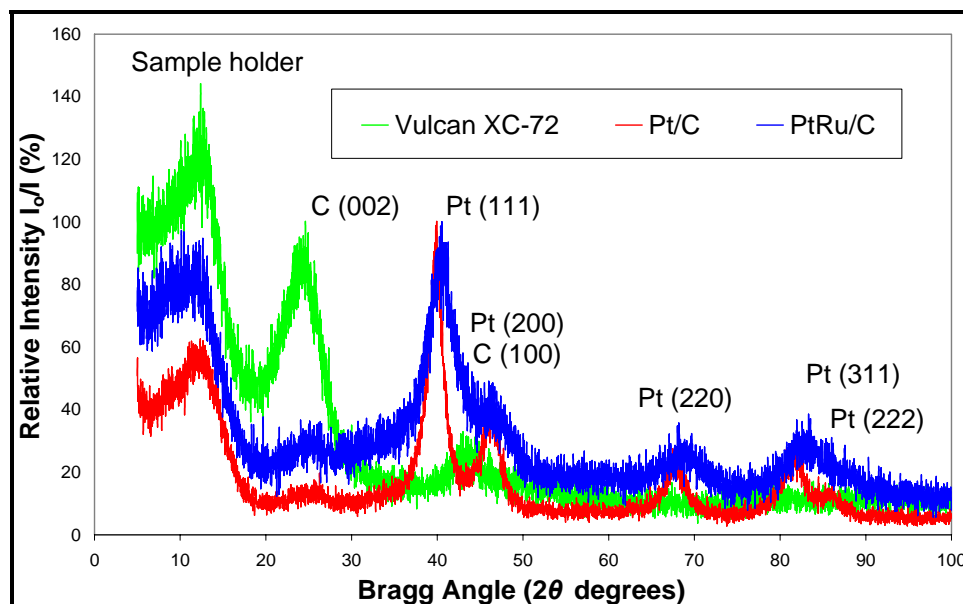


Figure 4.1. Diffractograms of Vulcan[®] XC-72; JM Pt/C; and JM PtRu/C

The peak at 13° 2θ could be credited to the x-ray beam striking the XRD sample holder and this artefact peak was observed in all three diffractograms.

Despite displaying a small degree of crystallinity due to its slightly graphitic nature, with the appearance of low-index diffraction peaks (002) at 24° 2θ and (100) at 43° 2θ , Vulcan[®] XC-72 was generally accepted to be amorphous in nature. The observation of the slight crystallinity of Vulcan[®] XC-72 was similar to that of Wong *et al* [122]. These low-index diffraction peaks will always be observed when analyzing carbon-supported nanophase electrocatalysts.

Broad diffraction peaks were observed in the diffractograms of both nanophase JM Pt/C and JM PtRu/C catalysts in Figure 4.1, and was indicative of a decrease in the particle size to the nanometre domain. The face-centred cubic (FCC) structures of JM Pt/C and JM PtRu/C were confirmed by the alternation of singlet and doublet diffraction peaks in the corresponding diffractograms. JM Pt/C and JM PtRu/C therefore had space-filling efficiencies of 74% (cubic-closest packing), meaning 26%

of the crystal lattice was occupied by atomic voids. Pt(111) crystal facets exhibited the highest intensity in the diffractograms, suggesting high densities of (111)-orientated crystals. (111) facets may be the most reactive in JM Pt/C and JM PtRu/C, and it has been stated by Cattaneo *et al* [41] that Pt (111) crystals have the lowest onset potential for methanol oxidation and the lowest CO_{ad}-poisoning rate in single-crystal analysis. This makes high (111) facet densities favourable for high methanol oxidation catalytic activities. For JM PtRu/C in Figure 4.1, diffraction peaks corresponding to the characteristic hexagonal-closest-packing (HCP) structure of Ru were absent, confirming the complete alloying of Ru atoms into the Pt lattice and the absence of isolated Ru [123, 124]. Also, lower peak intensities in the diffractogram for JM PtRu/C confirmed the alloying of Ru atoms into the Pt lattice. Slight Bragg angle shifts in diffraction peaks towards higher angles were observed in JM PtRu/C compared to JM Pt/C and were indicative of a high degree of alloying, similar to that observed by Tsou *et al* and Guo *et al* [125, 126]. The values for the shifts can be observed in Table 4.1

Inter-planar spacings (d_{hkl}) were calculated from Bragg's Law ($n\lambda = 2d \sin \theta$), where $n = 1$ (first-order diffraction), λ (Cu K α) = 1.5418 Å, and are given in Table 4.1.

**Table 4.1. Inter-planar spacings (d) in JM Pt/C and JM PtRu/C
(EXP = Experimental value, REF = Reference value)**

FCC facet	$2\theta_{Pt/C}$	$\theta_{Pt/C}$	Pt/C d_{EXP} (Å)	Pt _{BULK} d_{REF} (Å)	$2\theta_{PtRu/C}$	$\theta_{PtRu/C}$	PtRu/C d_{EXP} (Å)
(111)	39.94	19.97	2.26	2.27	41.28	20.64	2.19
(200)	46.80	23.40	1.94	1.96	47.05	23.53	1.93
(220)	67.94	33.97	1.38	-	69.50	34.75	1.35
(311)	82.10	41.05	1.17	1.18	83.74	41.87	1.15
(222)	86.24	43.12	1.13	-	88.34	44.17	1.11

Calculated JM Pt/C d_{hkl} -values were compared to bulk Pt reference values [123]. Differences in d_{hkl} were a result of peak-broadening upon decreasing the particle size to the nanoscale. The shift in 2θ upon alloying with Ru led to a slight decrease in d_{hkl} . In addition, lattice parameters (a_0) decreased upon alloying with Ru, indicative of a contraction in the atomic structure and may account for differences in chemical behaviour between JM Pt/C and JM PtRu/C. d_{REF} values for pure Ru were 3.343Å for Ru(002) at 42° 2θ ; and 2.142Å for Ru(101) at 44° 2θ ; and 2.056Å for Ru(102) at 58° 2θ [123, 124]. This further confirmed the absence of isolated Ru and the high degree of alloying in the commercial JM PtRu/C.

Lattice parameters (a_0) could be calculated using the following equation:

$$a_0 = d\sqrt{h^2 + k^2 + l^2}$$

Where h , k , and l are obtained from the (111) diffraction peak for JM Pt/C and JM PtRu/C, and d = the inter-planar spacing obtained using Bragg's Law.

Particle size could be calculated using the Scherrer equation, given as:

$$D = 0.9\lambda/\beta\cos\theta$$

Where, 0.9 = shape factor; λ = x-ray wavelength = 1.5418 Å; β = peak-width at half peak-height (radians); θ = angle of reflection.

Calculated lattice parameters and particle sizes for JM Pt/C and JM PtRu/C based on the XRD analysis performed in this study were compared to literature values and supplier specifications and are presented in Table 4.2.

Table 4.2. Experimental and literature lattice parameters and nanoparticle sizes

Material	Lattice parameter a_0 (Å)					XRD particle size (nm)		
		Guo	Tripković	Johnson	Bulk Pt		Guo	Johnson
	Experimental	<i>et al</i>	<i>et al</i>	Matthey™		[66]	Experimental	<i>et al</i>
		[126]	[127]	[26]			[126]	[26]
JM Pt/C	3.91	3.916	-	-	3.924	4.23	3.8	4.5
JM PtRu/C	3.79	-	3.86	3.90	-	3.48	3.2	4.0

In Table 4.2, it is shown that the crystal structure of Pt was observed to contract upon decreasing the particle size to the nanoscale, as evidenced by the deviation in the a_0 between nanophase JM Pt/C and bulk Pt. As a_0 is a dimension expressing the distance between two lattice points of the Pt unit cell and is related to inter-atomic distance, it may explain the deviation in chemical behaviour upon decreasing the particle size to the nanoscale. The calculated a_0 for JM Pt/C and that determined by Guo *et al* [126] were similar. The calculated a_0 for JM PtRu/C was smaller than the value determined by the supplier, Johnson Matthey™, and the value determined by Tripković *et al* [127]. A decrease in a_0 upon alloying Ru into Pt was also observed by Radmilović, *et al* [32] and supported the idea of a solid solution rather than a physical mixture of the two metals. A large decrease in the a_0 was observed upon alloying Ru into the Pt structure, explaining the differences in their chemical behaviour. Also, the atomic radii of Pt and Ru are 1.38 Å and 1.33 Å respectively, further confirming a contraction in the atomic structure upon alloying Ru atoms into the Pt crystal lattice. This could lead to a “tight” atomic arrangement resulting in the deviation in the chemical behaviour observed between JM Pt/C and JM PtRu/C.

In terms of JM Pt/C particle size, the value of 4.23 nm calculated using the Scherrer equation and XRD line-broadening compared well to the size of 4.5 nm specified by the supplier, Johnson Matthey® [26]. Similarly, the JM PtRu/C nanoparticle size was calculated as 3.48 nm, comparing well to the size of 3.2 nm determined by Guo *et al* [126] and 4 nm maximum specified by the supplier, Johnson Matthey® [26]. The

smaller sizes of PtRu/C particles, compared to Pt/C, were a result of a contraction of the lattice parameters upon the alloying of smaller Ru atoms into the Pt nanoparticle atomic structure.

SAED patterns were used qualitatively to confirm the crystallinity and symmetry of Vulcan[®] XC-72, JM Pt/C, and JM PtRu/C electrocatalysts and are presented in Figure 4.2.

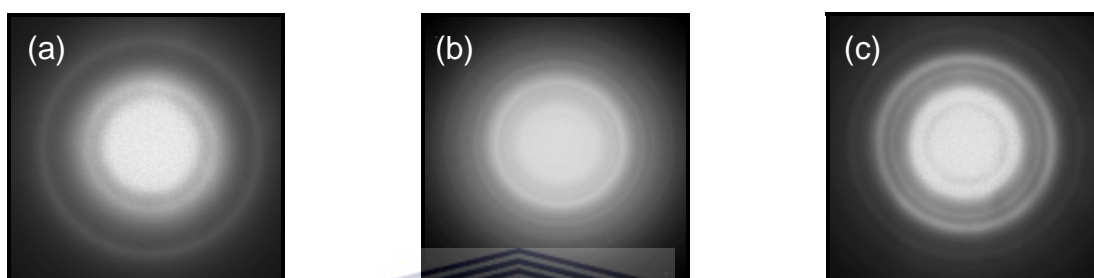


Figure 4.2. Selected-area electron diffraction patterns of (a) Vulcan[®] XC-72; (b) JM Pt/C; and (c) JM PtRu/C nanophase electrocatalysts

Vulcan[®] XC-72 (Figure 4.2 a) generally exhibited an amorphous nature with a slight degree of crystallinity, as evidenced by the appearance of C(002) and C(100) diffraction rings. The crystallinity may be attributed to the slightly graphitic nature of Vulcan[®] XC-72. This observation was similar to that of Wong *et al* [122]. The amorphous nature of Vulcan[®] XC-72 accounted for the diffused nature of the SAED patterns for carbon-supported JM Pt/C and JM PtRu/C.

The appearance of several diffraction rings signified the polycrystallinity of JM Pt/C (Figure 4.2 b). It was observed that the (200) and (222) rings could not be resolved from the (111) and (311) rings, respectively. The SAED pattern of JM PtRu/C (Figure 4.2 c) was similar to that of JM Pt/C with no additional rings observed. This observation further confirmed the complete alloying of Ru into the Pt lattice. The appearance of the diffraction rings suggested good crystalline symmetry in JM Pt/C

and JM PtRu/C. A simplified depiction of the rings in SAED patterns for JM Pt/C and JM PtRu/C electrocatalysts is given as Figure 4.3.

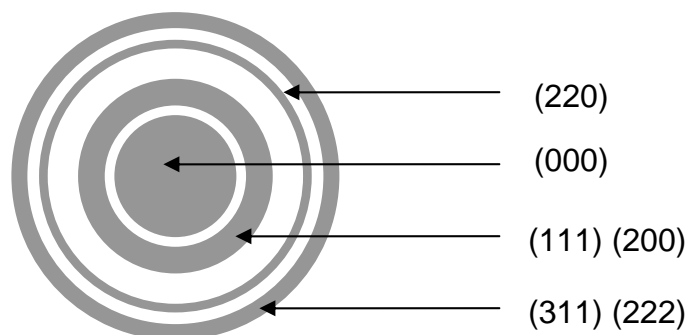


Figure 4.3. Simplified diagram of JM Pt/C and JM PtRu/C selected-area electron diffraction patterns

In conclusion, XRD confirmed the FCC structure of JM Pt/C and JM PtRu/C with Ru completely alloyed into the Pt structure in the latter electrocatalyst. High densities of (111) crystal facets confirmed the potential for the high reactivity of JM Pt/C and JM PtRu/C in surface sensitive reactions. Observed shifts in 2θ , lower peak intensities, changes in a_0 and d_{hkl} confirmed the complete alloying of Ru into the Pt structure. JM Pt/C and JM PtRu/C have metal particle sizes of 4.23 nm and 3.48 nm, respectively. These particle sizes corresponded well to sizes determined in literature, demonstrating the accuracy of the technique. A decreased particle size in fabricated nanophase electrocatalysts compared to commercial Johnson Matthey™ electrocatalysts may favour increased activity and should be investigated using XRD. XRD could therefore be used quantitatively and qualitatively in the characterization of nanophase electrocatalysts and produced reliable and reproducible results. Lastly, SAED studies confirmed the polycrystallinity and symmetry in JM Pt/C and JM PtRu/C. The polycrystallinity and symmetry of fabricated materials can thus potentially also be monitored using SAED. The technique was limited to a qualitative characterization tool as quantitative information was difficult to extract from the SAED patterns.

4.1.2. AGGLOMERATION AND AGGREGATION OF SUPPORTED NANOPHASE ELECTROCATALYSTS

The agglomeration and aggregation states in supported nanophase electrocatalysts were investigated using SEM and HPPS, respectively. An SEM study was conducted on JM Pt/C and JM PtRu/C catalysts to investigate the agglomeration of these supported electrocatalysts. The procedure was given in Section 3.3.3. An SEM study of Vulcan[®] XC-72 was also conducted for comparison to JM Pt/C and JM PtRu/C. Micrographs for JM Pt/C, JM PtRu/C, and Vulcan[®] XC-72 are presented in Figure 4.4.

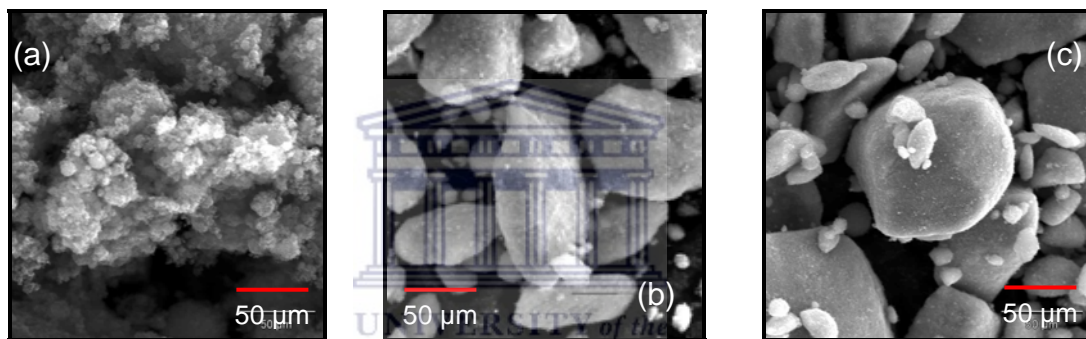


Figure 4.4. Scanning electron micrographs of nanophase electrocatalysts (a) Vulcan[®] XC-72; (b) JM Pt/C; (c) JM PtRu/C, (magnification = 500 X)

Metal nanoparticles could not be resolved from the carbon support materials using SEM and the technique was limited to the study of the agglomerate size distribution of the carbon support material.

In Figure 4.4(a), a wide agglomerate size distribution, ranging between 100 and 400 μm , was observed in Vulcan[®] XC-72. Jordan *et al* [17] stated that Vulcan[®] XC-72 consisted of spherical primary carbon particles, with sizes ranging between 30-50 nm. The primary carbon particles and their sizes could not be resolved using SEM. This demonstrated the high agglomeration of the nanophase JM Pt/C electrocatalyst and the weaknesses of the SEM in a characterization study of carbon-supported

nanophase electrocatalysts. In Figures 4.4(b) and 4.4(c), wide agglomerate size distributions (20-200 μm) were observed for JM Pt/C and JM PtRu/C, respectively. Koper *et al* [5] have suggested that smaller carbon support particle sizes resulted in enhanced electrocatalysis of the MOR and ORR, and that physical properties of the carbon support may affect the activity of Pt for the MOR and its reaction kinetics. Holister *et al.* [4] suggested that wide carbon support size distributions resulted in difficulties when studying the electrochemical behaviour of supported electrocatalysts and emphasized that agglomeration of Pt/C may result in a change of reactivity.

According to Cabot™ Corporation [20], primary carbon black support particles aggregate spontaneously after manufacture and cannot be broken down after aggregation. The aggregate size and aggregate size distribution of nanophase JM Pt/C and JM PtRu/C electrocatalysts were therefore studied using HPPS analysis using the procedure given in Section 3.3.5. A range of dispersants were screened prior to the collection of analytical data using JM Pt/C as a benchmark for the aggregate size evaluation. Refractive indices of dispersants were determined by Abbé refractometer and viscosities were obtained from literature. Results of the dispersant validation are given in Table 4.3.

Table 4.3. Screening of dispersants for JM Pt/C aggregate size analysis by HPPS

<i>Dispersant</i>	<i>Viscosity (cP), 25 °C</i>	<i>Refractive index η_D^{25}</i>	<i>Aggregate size (nm)</i>
Acetic acid	1.13	1.372	598.8
Toluene	0.62	1.496	Corrosive
Tetrahydrofuran	0.46	1.409	Corrosive
Methanol	0.55	1.326	307.7
Water	0.89	1.332	319.7
Ethanol	1.26	1.359	287.5
Acetone	0.30 (at 20 °C)	1.356	Corrosive
<i>Iso</i> -propanol	2.04	1.377	295.3

Aggregate size data was not collected when using tetrahydrofuran, toluene, and acetone as these strong solvents corroded the sample cuvettes due to their high affinity for the branched-chain lower-density polyethylene, which constituted the sample cuvettes. The best particle size data and the narrowest particle size distribution ranges were collected when using ethanol as the dispersant. Ethanol was henceforth used in the HPPS analysis.

HPPS analysis was conducted on JM Pt/C in an ethanol dispersant. An HPPS analysis on JM PtRu/C was assumed to produce similar results to that of JM PtRu/C. Results were tabulated in Table 4.4. Replicate samples were identified as Samples A-G. An HPPS analysis was also conducted on Vulcan[®] XC-72 and the analytical data is presented as APPENDIX A. The smaller aggregate size for JM Pt/C (266 nm) compared to Vulcan[®] XC-72 (366 nm) demonstrated the reduction in aggregation with the introduction of a metal phase. The Pt nanoparticles in JM Pt/C may plug the pores or voids of the carbon black aggregates in the preparation step leading to a decrease in the carbon black aggregate size. Platinum nanoparticles may also coat the surfaces of the carbon support thereby decreasing the interparticulate attraction between carbon support particles and resulting in smaller aggregates.

Table 4.4. Pt/C aggregate size data (ethanol dispersant)

Sample identification	Analysis number and particle size (nm)					Mean particle size (nm)
	1	2	3	4	5	
<i>A</i>	275.2	273.0	282.9	272.6	274.3	275.6
<i>B</i>	252.2	261.6	261.1	263.5	261.2	259.9
<i>C</i>	267.3	257.9	259.5	255.8	259.7	260.0
<i>D</i>	279.6	282.3	271.4	279.5	283.1	279.2
<i>E</i>	260.1	255.0	279.3	293.3	295.5	276.6
<i>F</i>	260.4	262.4	263.2	263.0	264.3	262.7
<i>G</i>	257.7	252.9	248.5	249.0	246.8	251.0
Population mean = 266.4 nm						
Population deviation (precision) = 10.7 nm						

From Table 4.4, the mean aggregate size was determined as 266 nm, credited to the smallest JM Pt/C aggregates attainable in the analysis. Jordan *et al* [17] stated that Vulcan[®] XC-72 consisted of spherical primary particles, with sizes ranging between 30-50 nm. This demonstrated the high aggregated state of JM Pt/C, which occurred spontaneously after the manufacture of the Vulcan[®] XC-72 carbon supports. Also, SEM particle sizes ranged between 20-200 μm , demonstrating the high agglomeration of the electrocatalyst in the “*as-received*” form, which may influence the chemical behaviour of JM Pt/C.

The calculated standard deviation on the analytical data (10.7 nm) illustrated the fairly good analytical precision of the HPPS analysis.

The aggregate size distribution of JM Pt/C is presented in Figure 4.5. The aggregate size distribution ranged between 150-300 nm illustrating a fairly wide aggregate size distribution in JM Pt/C electrocatalysts.

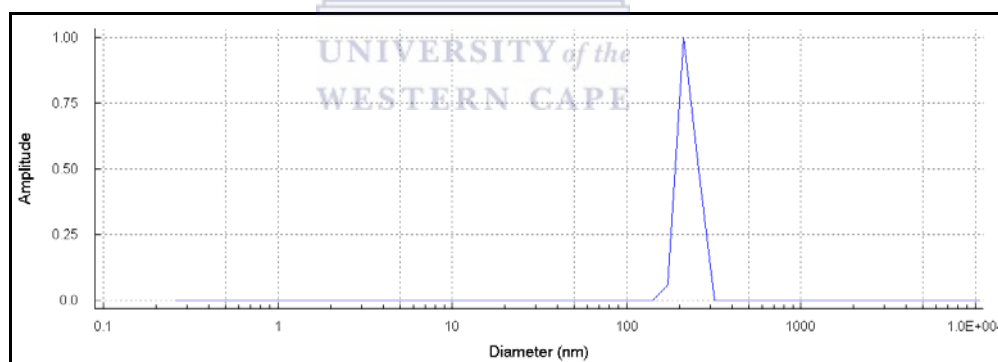


Figure 4.5. Aggregate size distribution graph of JM Pt/C dispersed in ethanol

In conclusion, metal nanoparticles could not be resolved using SEM and the technique was limited to the study of the agglomerate size distribution of the carbon support material in nanophase electrocatalysts. JM Pt/C and JM PtRu/C were determined to have wide agglomerate size distributions of 20-200 μm . This demonstrated the high agglomeration of the “*as-received*” materials. In the HPPS

analysis, a mean JM Pt/C aggregate size of 266 nm and a wide aggregate size distribution of 150-300 nm were observed. Also, a mean aggregate size of 366nm in Vulcan[®] XC-72 indicated that metal loading increased the separation of agglomerated carbon. The high precision of the HPPS analysis also confirmed the advantages of using this technique in the determination of aggregate size and aggregate size distribution of carbon-supported nanophase electrocatalysts. Finally, the best aggregate sizes and aggregate size distributions were obtained when using ethanol as the sample dispersant. HPPS analysis can therefore quantitatively be used in the determination of aggregate size and aggregate size distribution in fabricated carbon-supported nanophase electrocatalysts.

4.1.3. METAL PARTICLE SIZE AND METAL PARTICLE SIZE DISTRIBUTION OF SUPPORTED NANOPHASE ELECTROCATALYSTS

It was necessary to discriminate between the carbon support and the electrocatalyst particle size, which could not be achieved using SEM or HPPS. These techniques were unable to discern between the support and the catalyst as was shown in Section 4.1.2. Moreover, XRD could not be used to determine the average carbon support particle size. For this reason a transmission electron microscopic (TEM) analysis was conducted.

TEM analysis was conducted on carbon-supported nanophase JM Pt/C and JM PtRu/C to investigate the metal particle size and metal particle size distribution using the procedure given in Section 3.3.4. Vulcan[®] XC-72 was analysed in order to distinguish the carbon support from the metal catalyst. Micrographs for the TEM analysis of JM Pt/C and JM PtRu/C and Vulcan[®] XC-72 are presented in Figure 4.6.

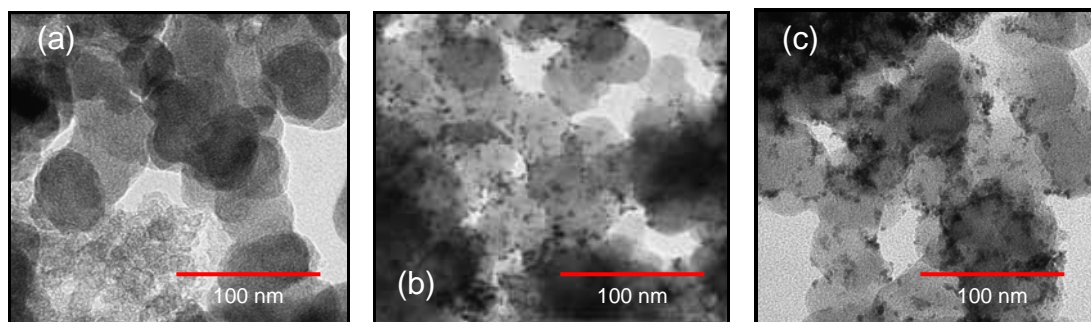


Figure 4.6. Transmission electron micrographs of (a) Vulcan[®] XC-72; (b) JM Pt/C; and (c) JM PtRu/C nanophase electrocatalysts

In Figure 4.6 (a), Vulcan[®] XC-72 primary particles appeared oval and had average particle sizes \approx 50-60 nm, which compared well with the range of 30-50 nm determined by Jordan *et al* [17] and 12-75 nm specified by the supplier, CabotTM Corporation [20]. The high degree of aggregation, agglomeration, and high density of voids were observed similar to that reported by CabotTM Corporation [20], as determined using HPPS and SEM analysis in Section 4.1.2.

Pt nanoparticles, in JM Pt/C, were well-dispersed on the carbon support (Figure 4.6b). Large Pt agglomerates were also observed in certain portions of the sample. Pt nanoparticles generally ranged between 2-7 nm in size and were dispersed on carbon particles which were generally 50-60 nm in size. The average Pt particle size was 4.2 nm, representing a metal surface area of 66.7 m²/g [25]. These particles were comprised of about 2577 constituent atoms, which was calculated using an equation given by Mukerjee [48]:

$$N(t) = [d/(1.11 \times d_{at})]^3$$

where $N(t)$ = number of atoms in Pt cluster

d = diameter of particle = 4.2 nm

d_{at} = diameter of a Pt atom = 0.276 nm

The average JM Pt/C metal particle size specified by the supplier Johnson Matthey™ was 4.5 nm with a metal surface area of 62.3 m²/g [26]. Experimental values were thus in good agreement with the values determined by the manufacturer. In contrast, the average Pt particle size in JM Pt/C determined by Prabhuram *et al* [25] was ±3.5 nm with a particle size distribution ranging between 3-4 nm. Prabhuram *et al* [25] also stated that the 3-4nm size range produced the highest activities towards the MOR among Pt/C electrocatalysts. JM Pt/C therefore should have a high activity towards the MOR.

The metal particle sizes in PtRu electrocatalysts with different atomic ratio compositions, namely JM Pt₂₀Ru₁₀/C and JM Pt₃₀Ru₁₅/C catalysts, were studied to determine the influence of the chemical weight ratio on the metal nanoparticle size. Results are tabulated in Table 4.5.

Table 4.5. Metal particle size data of JM Pt₂₀Ru₁₀/C and JM Pt₃₀Ru₁₅/C catalysts

JM Pt ₂₀ Ru ₁₀ /C	JM Pt ₃₀ Ru ₁₅ /C
Number of measurements = 20	Number of measurements = 20
Mean metal particle size = 3.15 nm	Mean metal particle size = 3.07 nm
Standard deviation = 1.18 nm	Standard deviation = 0.70 nm

Average metal particle sizes of 3.15 nm and 3.07 nm were measured for JM Pt₂₀Ru₁₀/C and JM Pt₃₀Ru₁₅/C, respectively. It was concluded that the chemical weight ratio of PtRu does not exhibit a significant influence on the size of carbon-supported PtRu nanoparticles. Generally, PtRu nanoparticles in JM Pt₃₀Ru₁₅/C were smaller than Pt nanoparticles in JM Pt/C and appeared more agglomerated on the carbon support. The particle size distribution ranged between 2-5 nm with PtRu nanoparticles well dispersed over the 50-60 nm carbon supports. In comparison, Guo *et al* [126] determined JM PtRu/C as having TEM particle sizes of 3.1 nm and a

particle size distribution between 2-4 nm. Johnson Matthey™, however, determined the average particle size as being 4 nm [26].

In conclusion, Vulcan® XC-72 was observed by TEM to have a primary carbon particle size range between 50-60 nm. JM Pt/C had an average metal particle size of 4.2 nm, with a particle size distribution between 2-7 nm, corresponding to a specific surface area of 66.8 m²/g. In contrast, JM Pt₃₀Ru₁₅/C had an average particle size of 3.07 nm, with a 2-5 nm particle size distribution. The atomic ratio composition, in PtRu/C, was not found to have a significant influence on the particle size. TEM exhibited both high precision and accuracy in that the particle sizes determined were reproducible (small measured particle size range) and the particle sizes agreed well with those determined in literature [20, 26, 126]. In comparison, there was a good agreement in the particle sizes determined using XRD and TEM. XRD produced particle sizes of 4.23 nm for JM Pt/C and 3.48 nm for JM PtRu/C. However, the metal particle size distribution and the degree of metal dispersion upon the support can only be determined using TEM. The time-consuming sampling in TEM limits its use in the determination of average metal particle size and XRD should be used for this type of analysis. TEM should be limited to the determination of particle size distribution and particle dispersion in carbon-supported nanophase electrocatalysts.

4.1.4. DETERMINATION OF SURFACE AREA AND POROSITY OF SUPPORTED NANOPHASE ELECTROCATALYSTS

The surface area and porosity of JM Pt/C and JM PtRu/C were determined using N₂ physisorption and the procedure is given in Section 3.3.6. The results obtained are presented in Table 4.6. Vulcan XC-72® was analysed in order to determine the contribution of the support to the overall porosity and surface area of the supported JM Pt/C and JM PtRu/C electrocatalysts. Adsorption isotherms are presented as APPENDICES B1-3.

Table 4.6. Surface area and porosity of JM Pt/C and JM PtRu/C electrocatalysts

Material	Single-point BET surface area (m ² /g)	External surface area (m ² /g)	Internal pore area (m ² /g)	Pore volume (cm ³ /g)	Average pore diameter (nm)
Vulcan [®] XC-72	242.35	189.56	52.79	0.024	9.53
JM Pt/C	132.09	118.12	13.97	0.006	15.59
JM PtRu/C	106.34	83.62	22.71	0.01	17.31

According to Jordan *et al* [17] and Cabot[™] Corporation, Vulcan XC-72[®] supports with particle sizes $\text{\O} = 30\text{-}50$ nm or $\text{\O} = 12\text{-}75$ nm corresponded to a surface area of 250-300 m²/g. In contrast the measured BET surface area of Vulcan XC-72[®] was 242.35 m²/g, corresponding to particle sizes of 50-60 nm, determined via TEM. Measured BET surface areas corresponded well with that obtained by Jordan *et al* [17], Li *et al* [19], and Prabhuram *et al* [25] which were 250-300 m²/g, 237 m²/g, and 250 m²/g, respectively. The measured Vulcan[®] XC-72 BET surface area did not correspond well to the value obtained by Easton [18], which was determined as 195 m²/g. Vulcan XC-72[®] can be described as consisting of small particles with a porous network between aggregates. In APPENDIX B1, the gas adsorption and desorption plots were observed to be mainly due to an external surface area as there was very little separation between the adsorption and desorption isotherm plots, indicative of a macroporous structure. This observation was in agreement with that of Prabhuram *et al* [25] who described Vulcan XC-72[®] as containing macropores. Also, the low pore volume (0.024 cm³/g) suggested that Vulcan XC-72[®] particles were relatively dense with a very small porous structure.

The BJH pore size distribution plot for Vulcan XC-72[®] is presented in Figure 4.7.

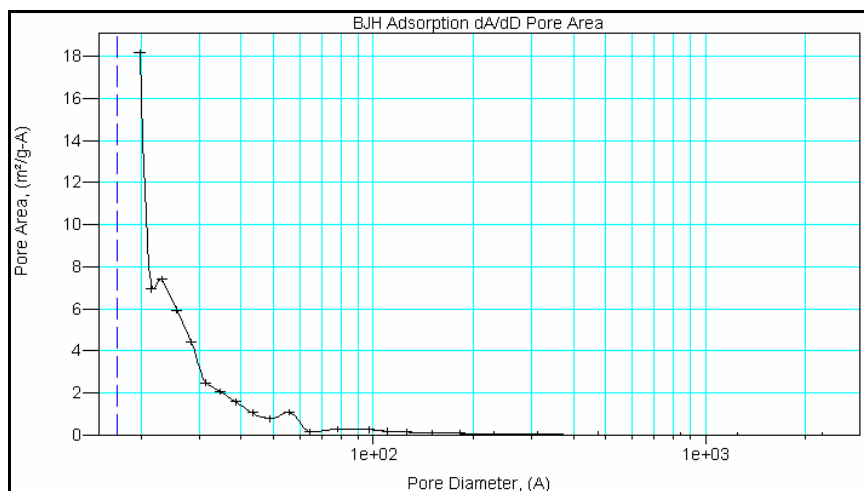


Figure 4.7. Barrett-Joyner and Halenda (BJH) pore size distribution plot of Vulcan[®] XC-72 using N₂-physisorption

From the BJH pore size distribution plot of Vulcan XC-72[®] (Figure 4.7), micropores (≤ 2 nm) and mesopores (≤ 50 nm) were observed to constitute a very small fraction of the internal pore area. Most of the internal pore area was not detected in the BJH pore size distribution plot and was concentrated outside the upper detection limit of the BJH pore size distribution plot (≥ 100 nm). Also, the isotherm plot (APPENDIX B1) illustrated that most of the total surface area was credited to the external surface and that the pore structure was on the macro-scale. The average pore size was determined as 9.53 nm (Table 4.6). This erroneous average pore size illustrated the inconsistencies in the determination of the average pore size using BET N₂-physisorption.

JM Pt/C had a relatively small surface area (132.09 m²/g), compared to Vulcan[®] XC-72. A lowered internal pore area was observed in JM Pt/C with a relatively large external surface area of 118 m²/g. The relative density of the JM Pt/C particles and a very small porous structure were confirmed by the low pore volume (0.006 cm³/g). The macroporous structure of JM Pt/C was confirmed in APPENDIX B2 by the low separation between the adsorption and desorption isotherm plots. This may mean that

very little of the Pt salt pre-cursor can be reduced in the pore structure during preparation and most of the Pt particles will be present at the surface [26].

The BJH pore size distribution plot for JM Pt/C is presented in Figure 4.8.

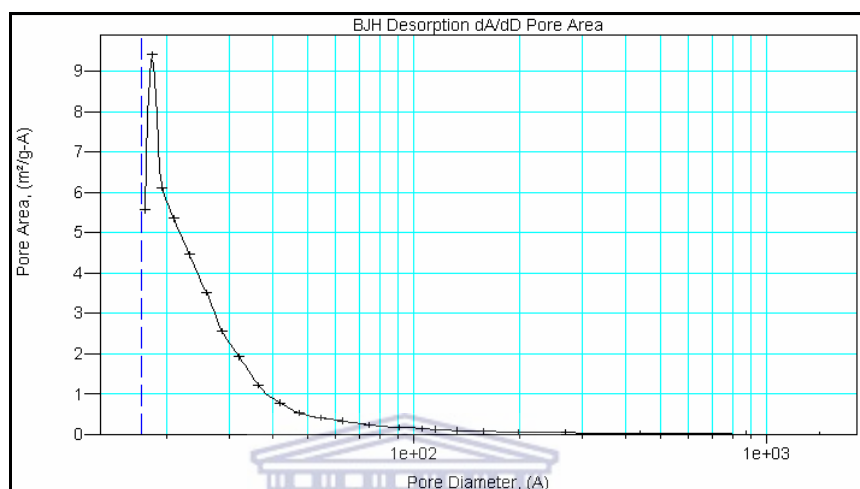


Figure 4.8. Barrett-Joyner and Halenda (BJH) pore size distribution plot of a JM Pt/C nanophase electrocatalyst using N₂-physisorption

From the BJH pore size distribution plot of JM Pt/C (Figure 4.8) micropores (≤ 2 nm) and mesopores (≤ 50 nm) were observed to constitute a very small fraction of the internal pore area. Most of the internal pore area was not detected in the BJH pore size distribution plot and was concentrated outside the upper detection limit of the BJH pore size distribution plot (≥ 100 nm). Also, the isotherm plot (APPENDIX B2) illustrated that most of the total surface area was credited to the external surface and that the pore structure was on the macro-scale. The average pore size was determined as 15.59 nm (Table 4.6). This erroneous average pore size again illustrated the inconsistencies in the determination of the average pore size using BET N₂-physisorption.

Lastly, JM PtRu/C exhibited a small surface area of 106.34 m²/g. A lowered internal pore area was observed in JM PtRu/C with a relatively large external surface area of

83.6 m²/g. The pore volume (0.01 cm³/g) suggested that JM PtRu/C particles were relatively dense and possessed a very small porous structure. The macroporous structure of JM PtRu/C was also confirmed, in APPENDIX B3, by the low separation between the adsorption and desorption isotherm plots.

The BJH pore size distribution plot of JM PtRu/C is presented in Figure 4.9.

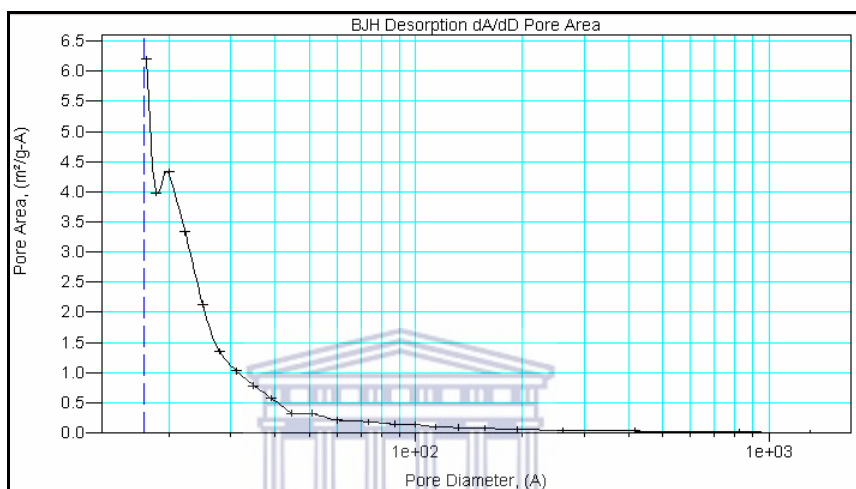


Figure 4.9. Barrett-Joyner and Halenda (BJH) pore size distribution plot of a JM PtRu/C nanophase electrocatalyst using N₂-physisorption

From the BJH pore size distribution plot of JM PtRu/C (Figure 4.9), micropores (≤ 2 nm) and mesopores (≤ 50 nm) were observed to constitute a very small fraction of the internal pore area. Most of the internal pore area was not detected in the BJH pore size distribution plot and was concentrated outside the upper detection limit of the BJH pore size distribution plot (≥ 100 nm). Also, the isotherm plot (APPENDIX B3) illustrated that most of the total surface area was credited to the external surface and that the pore structure was on the macro-scale. The average pore size was determined as 17.31 nm (Table 4.6). This erroneous average pore size again illustrated the inconsistencies in the determination of the average pore size using BET N₂-physisorption.

For JM Pt/C and JM PtRu/C, the total surface area of carbon black supports were reduced upon the addition of Pt and PtRu nanoparticles in the preparation step. This led to a reduction in the external surface area and could be related to the formation of larger particles or aggregates in the sample preparation step, where metal salts and high metal loadings were used. This may have caused aggregation and the loss of external surface area. Also, the pore volume and pore areas were reduced upon the introduction of Pt and PtRu nanophase electrocatalysts to the carbon support. This may be due the nanophase metal particles plugging the carbon black macroporous structure.

It should be noted that the pores in Vulcan XC-72[®], JM Pt/C, and JM PtRu/C can be classified as macropores (≥ 50 nm), according to the definition given by Haber [36]. This classification of macropores was confirmed by IUPAC. Prabhuram *et al* [25] described Vulcan XC-72[®] supports as containing mainly macropores and this study confirmed the macroporosity of JM Pt/C and JM PtRu/C. The IUPAC definition of macropores is pores with diameters exceeding 50 nm [128].

In conclusion, the measured BET surface areas had a good correlation with the values obtained by other investigators [17, 19, 25]. This demonstrated the high accuracy of the technique. JM Pt/C had a relatively small surface area ($132 \text{ m}^2/\text{g}$), compared to Vulcan[®] XC-72 ($242 \text{ m}^2/\text{g}$), while JM PtRu/C had an even lower surface area ($106 \text{ m}^2/\text{g}$) compared to Vulcan[®] XC-72. All materials analysed possessed macroporous structure. BET N₂-physisorption can quantitatively be used in the characterization of the surface area of carbon-supported nanophase electrocatalysts. The determination of the average pore size produced erroneous results with poor correlation obtained between average pore size, BJH pore size distribution range, and the isotherm plot. The poor correlation illustrated the inconsistencies in the determination of the average pore size of nanophase electrocatalysts using BET N₂-physisorption.

4.2. THERMAL AND CHEMISORPTIVE CHARACTERIZATION OF SUPPORTED NANOPHASE ELECTROCATALYSTS

The thermal characterization of supported nanophase electrocatalysts was conducted using thermogravimetric analysis (TGA). The experimental technique and parameters were given in Section 3.4

The chemisorptive characterization of supported nanophase electrocatalysts was conducted using temperature-programmed reduction (TPR). The experimental technique and parameters were given in Section 3.5.

4.2.1. THERMAL STABILITY OF NANOPHASE ELECTROCATALYSTS

Thermogravimetric analyses were conducted, under a N₂ flow, to study the thermal stability of nanophase JM Pt/C and JM PtRu/C electrocatalysts and that of the support material. Vulcan[®] XC-72 was analysed in order to discriminate between the behaviour of the carbon support and that of the metal nanoparticles. The ability of the metal nanoparticles to catalyze the thermal decomposition of the carbon support has been demonstrated [129]. Thermograms of Vulcan[®] XC-72, JM Pt/C and JM PtRu are presented in Figure 4.10.

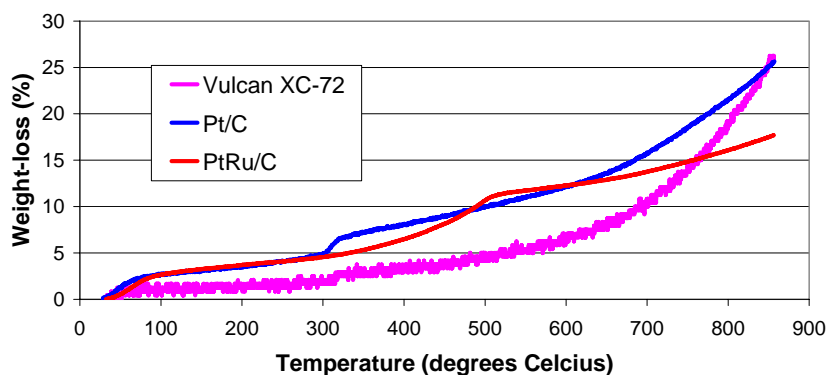


Figure 4.10. Weight-loss thermograms for the thermal decomposition of Vulcan[®] XC-72; JM Pt/C; and JM PtRu/C (ramp rate = 15 °C.min⁻¹)

In Figure 4.10, gradual evaporation of water from the pores and surface of the electrocatalysts and the carbon support were observed from the onset of the heating program: $C \cdot xH_2O \rightarrow C + xH_2O \uparrow$. The gradual weight-loss was indicative of a bond-breaking activation in which electrostatic attractions of water to the carbon support were weakened with increasing temperature. Moisture was also detected in a FTIR analysis with -OH functionalities appearing at about 3400 cm^{-1} , indicative of the presence of water on the surface or in the pores of the supported electrocatalysts. The gradual weight-loss observed between room temperature and 300°C was more pronounced for the metal loaded electrocatalysts than for the Vulcan[®] XC-72 support. This indicated a greater volatile content in the metal loaded electrocatalysts than for the Vulcan[®] XC-72 support, which may originate from their preparation using organic solvents during the incipient wetness impregnation preparation technique [31]. Vulcan[®] XC-72 experienced gradual thermal decomposition ascribed to slow carbon pyrolysis in the N_2 atmosphere [129]. Also, Vulcan[®] XC-72 exhibited good thermal stability. The overall weight loss was approximately 26% due to evaporation of water and volatile species and pyrolysis between room temperature and 850°C .

The JM Pt/C weight-loss thermogram was indicative of a 2-step thermal decomposition with the formation of a fairly stable intermediate, confirmed by a well-defined weight loss at 300°C . Between room temperature and 300°C , moisture and volatile species are evaporated from the pore structure and surface of the supported electrocatalyst. The dehydration of JM Pt/C is followed by a thermal event between 300°C and 325°C , attributed to the thermal decomposition of the carbon support into a fairly stable molecular fragment, and which was catalyzed by Pt [129]. The evolution of decomposition products, by pyrolysis of the carbon support, steadily continued to the end of the heating program. The overall rate of JM Pt/C thermal decomposition was 1.09 mg/hour , with a 26% overall weight-loss due to pyrolysis of the carbon support in the N_2 atmosphere, similar to that of the carbon support itself.

The JM PtRu/C thermogram was also indicative of a 2-step thermal decomposition. The initial loss of volatile components occurred progressively between room temperature and approximately 400°C, with the formation of a fairly unstable decomposition product at 500 °C. The gradual increase in weight loss at around 400-500°C could be ascribed to Ru not catalyzing the pyrolysis and thermal decomposition of the carbon support as efficiently as Pt and that served to retard the pyrolysis process. This was confirmed by the lowered overall decomposition rate of JM PtRu/C (18% weight loss at 0.76 mg/hour), compared to JM Pt/C. Another combustion-retarding factor may be the formation of a eutectic mixture between Pt and Ru at high temperature. This assumption may be valid considering the lowered melting points of metals upon decreasing the particle size to the nanometre domain [5, 7-11].

It was noteworthy that since the experiment was conducted in a N₂ atmosphere complete combustion of the carbon support was not achieved. Further, TGA in an oxygen atmosphere can be used in the determination of the weight composition of fabricated nanophase electrocatalysts.

In conclusion, the thermal transition at 500°C in JM PtRu/C, compared to that at 300°C in JM Pt/C, suggested the higher thermal stability of JM PtRu/C. The weight loss in all cases was ascribed to the slow decomposition of the carbon support material since the overall weight-loss in the case of JM Pt/C and JM PtRu/C did not exceed that of the Vulcan[®] XC-72 support material, indicating that the nanophase metals do not volatilise in the temperature range probed. TGA can be used both qualitatively and quantitatively in the characterization of nanophase electrocatalysts. However, the DMFC and SPE-electrolyser are operated between 60-120 °C and not at such harsh temperatures. The results obtained in the thermal characterization of nanophase electrocatalysts, using TGA, are therefore not significant in the context of nanophase electrocatalysts in fuel cell and electrolyser operation. At most some

volatile matter could be released, but since the fuel cells and their catalysts are hydrated this is unlikely to occur at the temperature of operation.

4.2.2. CHEMISORPTIVE SPECIATION OF NANOPHASE ELECTROCATALYSTS

A chemisorptive speciation of JM Pt/C and JM PtRu/C was undertaken to ascertain the number of reducible species on the catalyst surface, the reduction temperature, and the strength of the metal-support interactions. Vulcan[®] XC-72 was analyzed as a background material to discriminate the contribution of the support from the observations made for the metal nanoparticles. TPR profiles are presented as Figures 4.11 - 4.13.

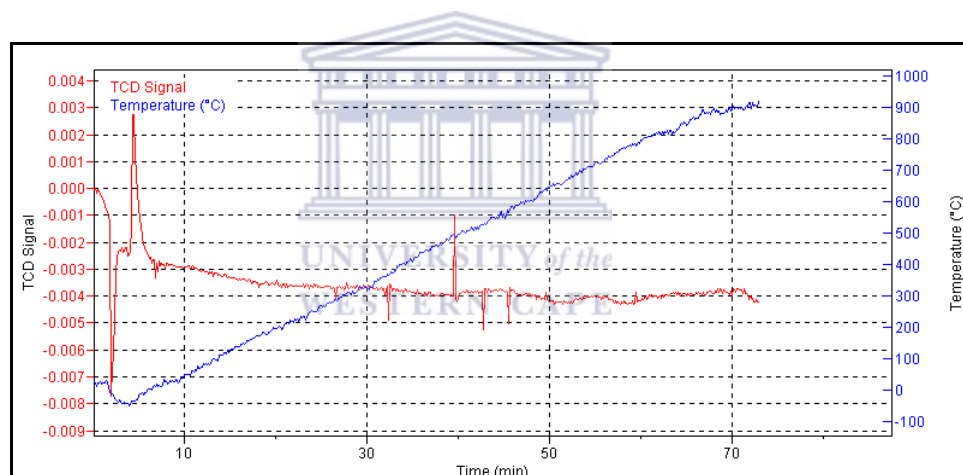


Figure 4.11. TPR profile of Vulcan[®] XC-72 (ramp rate = 15 °C.min⁻¹)

The expected absence of reducible species in the TPR profile of Vulcan[®] XC-72 was observed (Figure 4.11). The sharp artefact peaks observed at below ambient temperatures are due to the removal of the cold-gel and the sealing of the oven. Sharp artefact peaks observed in the temperature range 350-600°C are due to pressure fluctuations in the system as a consequence of the motion of the lightweight Vulcan[®] XC-72 particles within the sample tube under the flow of H₂.

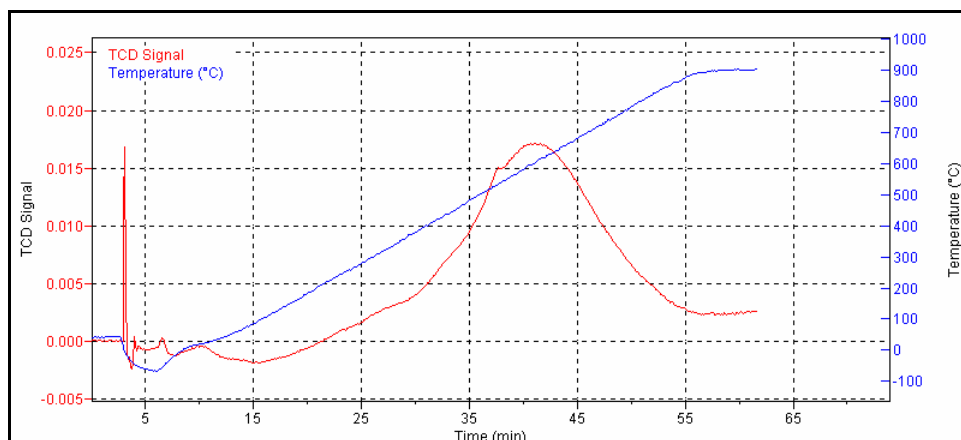


Figure 4.12. TPR profile of JM Pt/C (ramp rate = 15 °C.min⁻¹)

Two events occur in the TPR profile of JM Pt/C (Figure 4.12):

$\text{Pt}^{4+} \rightarrow \text{Pt}^{2+}$ transition at low temperature, given as: $\text{PtO}_2 + \text{H}_2 \rightarrow \text{PtO} + \text{H}_2\text{O}$

$\text{Pt}^{2+} \rightarrow \text{Pt}^0$ transition at high temperature, given as: $\text{PtO} + \text{H}_2 \rightarrow \text{Pt} + \text{H}_2\text{O}$

The high-temperature reduction peak of $\text{Pt}^{2+} \rightarrow \text{Pt}^0$ occurred at about 600 °C whilst the low-temperature reduction peak of Pt^{4+} to Pt^{2+} was observed at about 0 °C, representing a small portion of the total Pt present in JM Pt/C. The $\text{Pt}^{4+} \rightarrow \text{Pt}^{2+}$ transition was minimal and was poorly resolved from the baseline as the result of the rapid temperature change upon removal of the cold-gel, and the relative instability of the Pt^{4+} species compared to the Pt^{2+} species. Due to its instability Pt^{4+} readily decomposes to Pt^{2+} , hence the difficulty in its detection. The reduction of Pt^{2+} to Pt^0 was the major transition observed and was indicative of a measurable quantity of Pt^{2+} species existing on the carbon support of JM Pt/C. However, it was difficult to assign the chemical and catalytic behaviour of JM Pt/C to either Pt^{2+} or Pt^0 with certainty. Prabhuram, *et al* [25] showed by x-ray photoelectron spectroscopic (XPS) analysis of Pt/C that 60-74% of Pt was present in the metallic state, Pt^0 , the rest being in the Pt^{2+} state. Yang *et al* [130] suggested that the wetness-impregnation method in Pt/C preparation produced relatively low surface oxidation states, which is considered

suitable for the MOR. The reduction temperature maximum for JM Pt/C found in this study was 600 °C indicative of a fairly strong metal-support interaction [100].

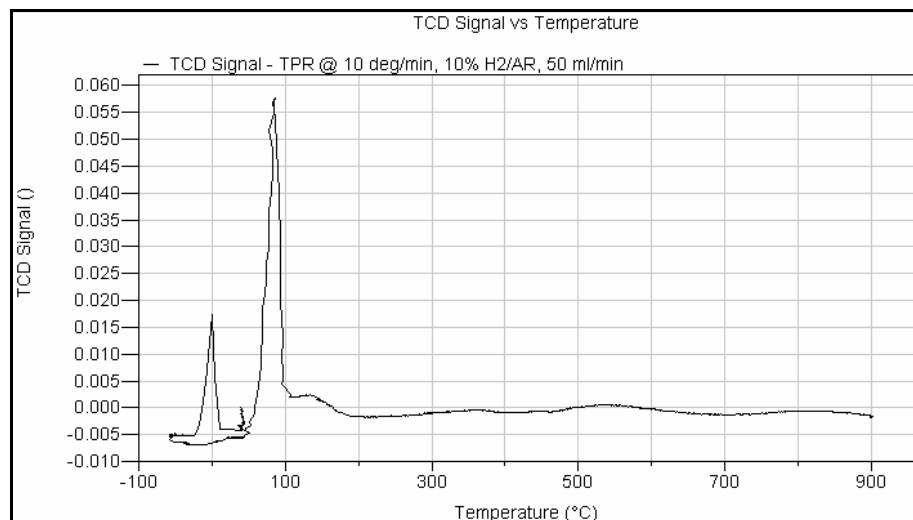


Figure 4.13. TPR profile of PtRu/C (ramp rate = 15 °C.min⁻¹)

In the TPR profile of JM PtRu/C (Figure 4.13), four peaks were observed. The first low temperature peak at 0°C could be ascribed to the reduction of Pt⁴⁺ to Pt²⁺. The greater part of the Pt component of JM PtRu/C was not in the most oxidised state since only a small broad peak for the Pt²⁺ to Pt⁰ transition could be detected at 600°C. Low temperature peaks at 90°C and 130°C were ascribed to Ru reductions in the PtRu-alloy [131]. The peak at about 90 °C may be the Ru⁴⁺ → Ru⁰ transition whereas the adjacent shoulder at 130 °C may be the Ru³⁺ → Ru⁰ transition, or the reduction of a less active Ru species. The presence of isolated Pt metal is hardly observable, whose major transition (Pt²⁺ → Pt⁰) appears at 600 °C, confirming the high degree of alloying in JM PtRu/C and the absence of isolated metals. The virtual absence of isolated Pt in PtRu/C catalysts was also observed by Kenvin [100]. It was also difficult to attribute the MOR-promoting action of Ru, in JM PtRu/C, to Ru³⁺; Ru⁴⁺; or Ru⁰ species as their concentrations were difficult to quantify. The quantity of each Ru oxidized species may be determined using a suitable chemical speciation methodology utilising a sequential extraction technique. This was not achievable in

this study, as a suitable sequential extraction methodology and leaching solutions could not be found in literature. Lastly, the metal-support interactions for JM PtRu/C are significantly weaker than that of JM Pt/C as the reduction temperature was much lower, indicative of the lower strength of the bond [99].

Johnson Matthey™ stated that deposited metal may be either in a reduced or unreduced form and that unreduced catalysts are often more active than pre-reduced catalysts [26]. It is generally understood that Pt and Ru in their zero-valent states perform better under fuel cell conditions than do their corresponding oxidized states. However, Long *et al* [131] claimed that Pt^0Ru^0 was much less active than PtRuO_xH_y towards the MOR, as PtRuO_xH_y promoted $\text{Ru}(\text{OH})_{\text{ad}}$ formation and is proton-conductive.

In conclusion, the $\text{Pt}^{4+} \rightarrow \text{Pt}^{2+}$ transition at low temperature and the $\text{Pt}^{2+} \rightarrow \text{Pt}^0$ transition at high temperature were observed on JM Pt/C. Thus Pt^{2+} and Pt^{4+} were determined to be the oxidised species on the JM Pt/C surface. In contrast, the $\text{Ru}^{4+} \rightarrow \text{Ru}^0$ and $\text{Ru}^{3+} \rightarrow \text{Ru}^0$ transitions were observed on JM PtRu/C. A small degree of Pt^{4+} was detected in JM PtRu/C. The metal-support interactions on JM Pt/C was significantly stronger than that of JM PtRu/C, as the reduction temperature was higher, indicative of the higher strength of the bond in Pt/C. The high metal-support interaction is favourable in fuel cell catalysts for long term durability. TPR can be concluded to be a qualitative and semi-quantitative analytical tool in the characterization of nanophase electrocatalysts. Observations in the TPR analysis are in good agreement with those in literature. TPR successfully speciated the surface chemical state and was able to qualitatively investigate the strength of the metal-support interaction of supported nanophase electrocatalysts.

4.3. SUMMARY OF MAIN RESULTS

The crystallinity, symmetry, atomic structure, and particle size of nanophase JM Pt/C and JM PtRu/C electrocatalysts were characterized using XRD. XRD was readily able to probe particles at the nanoscale. The following observations were made: (a) Pt and PtRu in JM Pt/C and JM PtRu/C, respectively, were polycrystalline and possessed face-centred cubic structure; (b) high densities of Pt(111) crystal facets confirmed the potential high reactivities of JM Pt/C and JM PtRu/C for surface sensitive reactions; (c) peak shifts, lowered peak intensities, changes in a_0 and d_{hkl} , and the absence of hexagonal closest-packing Ru peaks confirmed the complete alloying of Ru into the Pt structure and the absence of isolated Ru particles; (d) Pt nanoparticle size was determined as 4.23 nm, comparing well to the 4.5 nm specified by the supplier, Johnson Matthey™ [26]. Similarly, the PtRu nanoparticle size was calculated as 3.48 nm, with a satisfactory comparison to the 4 nm maximum specified by the supplier, Johnson Matthey™ [26]; (e) the calculated Pt a_0 compared well to the a_0 determined by Guo *et al* [126]. The differences in the calculated Pt a_0 compared to that of the bulk Pt material illustrated the deviation in the atomic structure characteristics upon decreasing the particle size to the nanometre domain [66]. The measured PtRu a_0 compared well to that specified by the supplier, Johnson Matthey® [26], and that determined by Tripković *et al* [127]. Based on the good comparison between the experimentally determined data and literature data (high accuracy), it is recommended that XRD be retained in the study of crystal/atomic structure, symmetry, and particle size of nanophase electrocatalysts using the procedure given in Section 3.3.1.

SAED studies confirmed the polycrystallinity and crystal symmetry in the JM Pt/C and JM PtRu/C electrocatalysts. It was difficult to extract quantitative information from the SAED patterns and the technique was therefore limited to a rapid qualitative analysis of polycrystallinity and crystal symmetry in nanophase electrocatalysts.

The agglomeration and aggregation states of JM Pt/C and JM PtRu/C particles were characterized using SEM and HPPS, respectively. SEM was unable to probe particles at the nanoscale and was unable to distinguish the metal nanoparticles from the carbon support. SEM was also unable to determine the size of the primary carbon particles of the Vulcan[®] XC-72 support. Carbon-supported JM Pt/C and JM PtRu/C electrocatalysts exhibited wide agglomerate size distributions of 20-200 μ m. HPPS was unable to distinguish between the particle size of the metal electrocatalyst and that of the carbon support. HPPS analysis gave a mean JM Pt/C aggregate size of 266 nm. This value was attributed to the size of the aggregates, which according to the supplier, cannot be broken down into primary particles [20, 26]. The high degree of agglomeration of the “*as-received*” materials was thus illustrated. The use of ethanol as dispersant proved optimal for the investigation of aggregation in supported nanophase electrocatalysts. HPPS demonstrated high precision in collecting analytical data, making its employment in a nanophase electrocatalyst characterization study favourable. Based on the observations, SEM and HPPS should be retained in the study of agglomeration and aggregation states of supported nanophase electrocatalysts using the procedures given in Section 3.3.3 and Section 3.3.5, respectively. The sample preparation step in HPPS analysis could potentially be further optimised by the use of various dispersants which were not utilised in the study.

Metal particle size and metal particle size distribution were characterized using TEM. The technique was readily able to probe particles at the nanoscale and could distinguish between the metal phase and the support material of the supported electrocatalysts. The following observations were made: (a) Vulcan[®] XC-72 primary carbon support particle size ranged between 50-60 nm, showing good correlation with values determined by the supplier, Cabot Corporation[™] [20]; (b) nanophase JM Pt/C had an average metal particle size of 4.2 nm, with a size distribution of 2-7 nm, corresponding to a metal surface area calculated to be 66.7 m²/g, in good agreement with values specified by the supplier, Johnson Matthey[™] [26]; (c) JM PtRu/C had an

average metal particle size of 3.07 nm, with a 2-5 nm size distribution, in good agreement with values specified by the supplier [26]; (d) The atomic weight ratio between Pt and Ru, in JM PtRu/C, was not found to have a significant influence on the PtRu particle size. Based on the observations, TEM should be retained for the determination of metal particle size and particle size distribution in supported nanophase electrocatalysts due to its high precision and accuracy in collecting analytical data using the procedure given in Section 3.3.4. It may also be used to determine the primary particle size of the carbon support material, which was unachievable using the other techniques in this study.

Total surface area and porosity of nanophase JM Pt/C and JM PtRu/C were determined using N₂-physisorption. The following observations were made: (a) The measured total surface area of the Vulcan[®] XC-72 compared well to the values determined in literature [17, 19, 25], thus illustrating the accuracy of the data collected and that of the technique; (b) JM Pt/C had a small surface area of 132 m²/g, while JM PtRu/C had an even smaller surface area of 106 m²/g; (c) JM Pt/C and JM PtRu/C possessed macroporous structure; (d) the average pore size measured did not correlate well to the BJH pore size distribution and the isotherm plot. This observation demonstrated the inconsistencies in measuring the average pore size using BET N₂-physisorption. Based on the observations, it was recommended that N₂-physisorption be maintained in the determination of total surface area of supported nanophase catalysts using the procedure given in Section 3.3.6. Pore size distribution determined from BJH data and the average pore size measurement should in future be considered with due caution as a generalised qualitative evaluation.

The thermal stabilities of JM Pt/C and JM PtRu/C were characterized using TGA. The following observations were made: (a) The thermal transition at 500°C in JM PtRu/C, compared to that at 300°C in JM Pt/C, suggests the higher thermal stability of JM PtRu/C. Based on the observations, it is recommended that TGA be maintained in the determination of thermal stability of nanophase electrocatalysts using the

procedure given in Section 3.4. However, thermal stability information has no great significance in the study of fuel cell electrocatalysts as the moderate operating temperatures of the DMFC and SPE-electrolyser range between 60-120°C and not at the high temperatures used in the thermogravimetric analysis.

Nanophase JM Pt/C and JM PtRu/C were chemically speciated using TPR. The following observations were made: (a) $\text{Pt}^{4+} \rightarrow \text{Pt}^{2+}$ transition at low temperature (0°C) and $\text{Pt}^{2+} \rightarrow \text{Pt}^0$ transition at high temperature (600°C) were observed on JM Pt/C. Pt^{2+} and Pt^{4+} were determined to be the oxidised species on the JM Pt/C surface; (b) $\text{Ru}^{4+} \rightarrow \text{Ru}^0$ and $\text{Ru}^{3+} \rightarrow \text{Ru}^0$ transitions were observed on JM PtRu/C; (c) small amounts of Pt^{4+} were detected in JM PtRu/C; (d) metal-support interactions on JM Pt/C were significantly stronger than those of JM PtRu/C as the complete reduction temperature (600°C for JM Pt/C compared to 130°C for JM PtRu/C) was higher. Based on the observations the following recommendations are made: TPR should be retained in the chemisorptive speciation of nanophase electrocatalysts and characterization of the strength of their metal-support interactions using the procedure given in Section 3.5.

For fabricated nanophase electrocatalysts to be considered applicable in the DMFC or SPE-electrolyser they should exhibit structural properties of a similar or enhanced nature, compared to that of the commercial Johnson Matthey™ electrocatalysts characterized in the investigation. Johnson Matthey™ electrocatalysts are currently employed in the DMFC and SPE-electrolyser and their structural properties serve as the benchmark, against which all fabricated materials are compared. Based on the structural, thermal, and chemisorptive characterization, nanophase electrocatalysts with catalytic performance potentially superior to that of the Johnson Matthey™ electrocatalysts can be designed by making the following structural modifications:

- Higher densities of Pt(111) facets for potentially higher catalytic activity. This requires a large reduction in the particle size to the nanoscale.

-
- In the case of PtRu/C catalysts, the Ru should be completely alloyed into the Pt structure. This allows for enhanced chemical interaction between adsorbates at the Pt and Ru active surface sites.
 - Smaller lattice parameters ($\leq 3.91\text{\AA}$ for JM Pt/C and $\leq 3.79\text{\AA}$ for JM PtRu/C) for potentially higher catalytic activity.
 - Smaller metal particle size ($\leq 4.23\text{ nm}$ for JM Pt/C and $\leq 3.48\text{ nm}$ for JM PtRu/C) for increased surface-to-volume ratios and a potentially higher catalytic activity.
 - Low degree of agglomeration in the metal nanophase electrocatalyst on the support material
 - Low degree of agglomeration and narrow agglomerate size distribution of carbon support for increased total surface area.
 - Smaller carbon support aggregate size ($\leq 266\text{ nm}$).
 - Narrow aggregate size distribution (JM Pt/C = 150-300 nm).
 - High reduction temperatures for high metal support interaction strength. This may potentially lead to increased reactivity and acid-base properties [13, 24].

After the characterization of the structural, thermal, and chemisorptive properties of commercial nanophase electrocatalysts an electrochemical characterization and screening of nanophase electrocatalysts was performed as set out in *Chapter 5*. The structural information gathered gave insight into the chemical nature of nanophase electrocatalysts. This is due to a direct relationship between the structural and chemical properties of nanophase electrocatalysts and their catalytic activity.

CHAPTER 5

RESULTS AND DISCUSSION: ELECTROCHEMICAL CHARACTERIZATION OF NANOPHASE ELECTROCATALYSTS

The structural, thermal, and chemisorptive characteristics of nanophase electrocatalysts were presented in *Chapter 4*. The electrochemical characterization and electrochemical screening of prospective nanophase electrocatalysts and their comparison to the commercial standard (i.e. JM Pt/C and JM PtRu/C) is presented in *Chapter 5*. The electrochemical properties subsequently characterized can be correlated to the structural, thermal, and chemisorptive properties established in the previous chapter.

Chapter 5 describes the development of a testing protocol for the electrochemical characterization and screening of materials used in the study. The characterization of nanophase commercial JM Pt/C; JM PtRu/C; and JM IrO₂ is presented. The testing protocol was used to determine the activity of novel electrocatalysts developed in parallel to this study. Finally, fabricated mesoporous silica-templated carbon analogues; Pt/C, PtRu/C, IrO₂, and CNT-supported Pt electrocatalysts were screened in terms of their electro-activities. These catalysts were prepared according to methods described in Section 3.1.2 [53, 57-59]. The electrochemical study was performed in order to evaluate the optimum application for these electrocatalysts.

5.1. ESTABLISHING A TESTING PROTOCOL FOR THE ELECTROCHEMICAL CHARACTERIZATION OF NANOPHASE ELECTROCATALYSTS

Prior to the electrochemical characterization and screening of commercial and fabricated nanophase electrocatalysts, it was imperative to design the electrochemical experiments necessary for the attainment of accurate data. For this reason parameters

such as experimental setup, electrode preparation, and electrolyte preparation were investigated before the electrochemical characterization of nanophase electrocatalysts could be addressed. The experimental parameters used in the electrochemical characterization of nanophase electrocatalysts were given in Section 3.6.

5.1.1. EXPERIMENTAL SETUP

The experimental setup used in the electrochemical characterization of nanophase electrocatalysts using cyclic and linear-sweep voltammetry is presented in Figure 5.1.

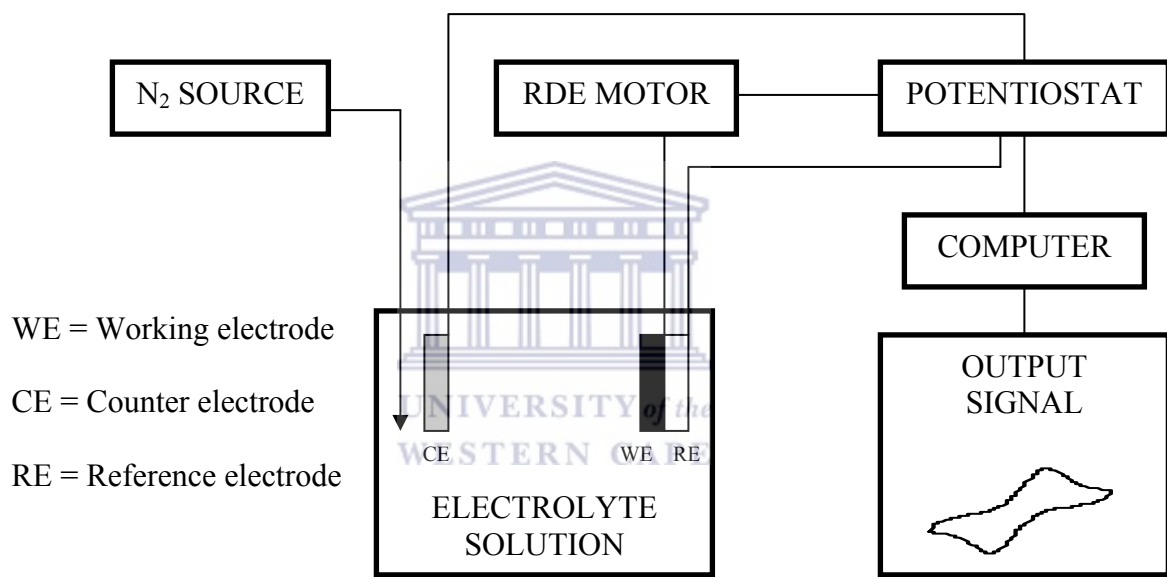


Figure 5.1. Experimental configuration for the electrochemical characterization and screening of nanophase electrocatalysts

The schematic of the electrochemical testing configuration as shown in Figure 5.1 allowed for the assessment of the electrocatalytic activity of nanophase electrocatalysts under well-defined mass transfer conditions. Typically, thin films of an electrocatalyst ink were deposited onto the working electrode (Section 5.1.3). With the unavailability of a Luggin capillary the reference electrode (RE) and working electrode (WE) were kept close together while the counter electrode (CE) was kept as

far away as possible from the working electrode to allow for sufficient current flow through the electrolyte. This configuration ensured that measurement errors related to the resistance of the test solution were kept to a minimum. Where applicable, the electrolyte solution was deaerated by purging with N_2 . The resistance across working electrodes was monitored prior to analysis, using a milli-ohmmeter, and test signals were run on the potentiostat prior to analysis using a dummy cell. Lastly, the standard potentials of all reference electrodes used were confirmed by testing relative to a self-fabricated standard hydrogen electrode (SHE). The experimental parameters were given in Section 3.6.

5.1.2. MODELLING THE SOLID-POLYMER ELECTROLYTE

It is difficult to conduct voltammetric analyses utilising a solid polymer electrolyte. For this reason, dilute acid solutions (e.g. $HClO_4$ and H_2SO_4) were used to model the solid polymer electrolyte. Typically 0.5-1.0 M H_2SO_4 solutions was used as electrolyte in the electrochemical characterization of nanophase materials as the pH of the acidic solution at these concentrations (pH = 1.3-1.2) is similar to the surface acidity or acid capacity (a measure of sulphonic acid equivalents in the polymer) of the Nafion[®] membrane. Unfortunately, the pH of the dilute acid solutions could not be compared to that of a Nafion[®] membrane as Nafion[®] is insoluble in water and can therefore not be assigned a pH value.

A dilute alcoholic solution of Nafion[®] is used to bind electrocatalysts to working electrodes and to increase the amount of metal catalyst particle exposed to the electrolyte.

5.1.3. ELECTROCATALYST CAST-FILM APPLICATION

The application of the electrocatalyst by a cast-film route to the glassy carbon working electrode was investigated using cyclic voltammetry. Cast-films were prepared using three different approaches. The first approach was to apply an aqueous

JM Pt/C catalyst layer over a Nafion[®] film layer (Pt/C on Nafion[®] film), the second approach was to homogeneously disperse the JM Pt/C catalyst in Nafion[®] solution to form an ink and then apply a film to the working electrode (Pt/C + Nafion[®] layer), and the third approach was to apply a Nafion[®] film over an aqueous JM Pt/C catalyst solution (Nafion[®] film on Pt/C). The working electrode was glassy carbon, the reference electrode was a saturated calomel electrode (SCE), and the counter electrode was a platinum wire basket. The resulting voltammograms (Figure 5.2) were recorded in 0.5M H₂SO₄ between -0.25 and 1.0 V_{SCE}, at a sweep rate of 20 mV.s⁻¹.

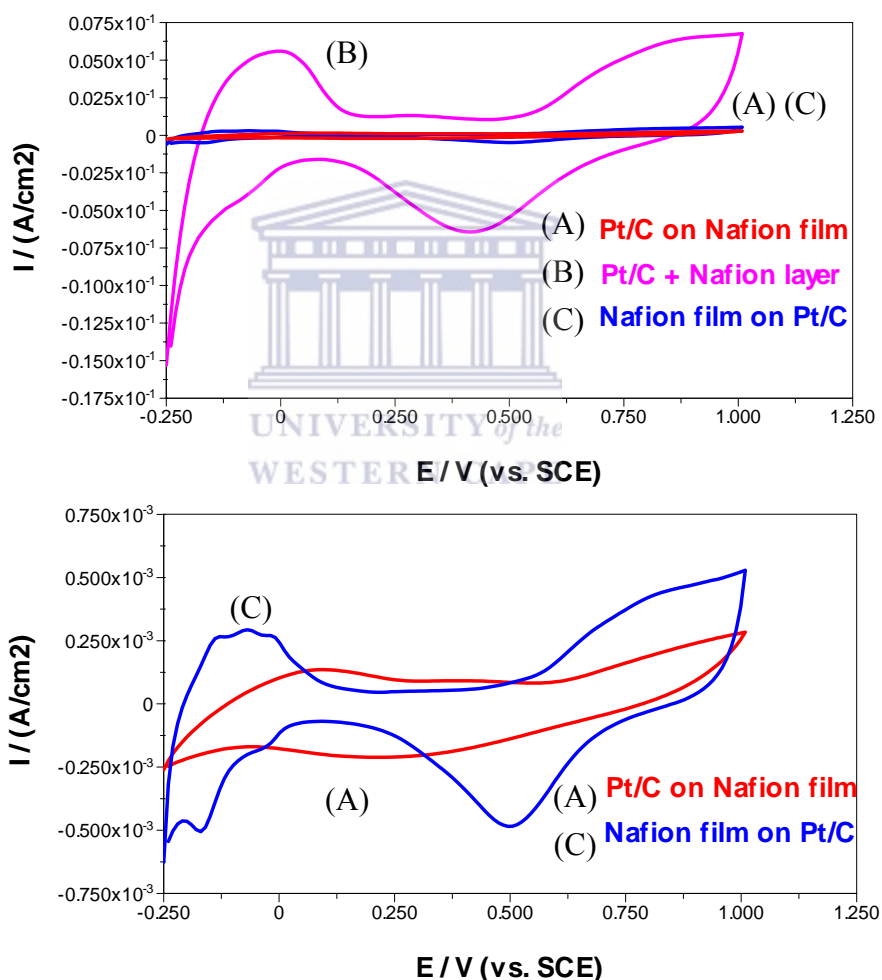
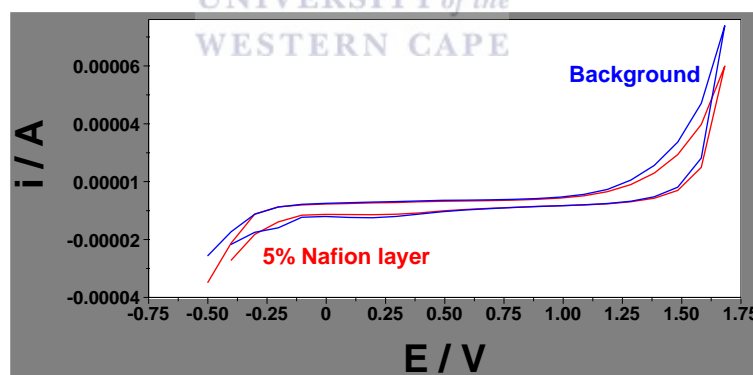


Figure 5.2. JM Pt/C electrocatalyst cast-film application experiment in 0.5M H₂SO₄ (sweep rate = 20 mV.s⁻¹)

In Figure 5.2, highest activity in the electrolysis of dilute acid on Pt was observed when the JM Pt/C electrocatalyst was dispersed in Nafion[®] solution to form an ink (B). This preparation technique was similar to that of Gojkovic *et al* [132]. In contrast, deposition of a Nafion[®] film on a Pt/C electrocatalyst layer (C) produced the distinctive wave-shape of dilute acid electrolysis on Pt, albeit with significantly lower activity. This preparation technique was similar to that of Schmidt *et al* [133]. The poorest analytical signal was recorded when the JM Pt/C electrocatalyst was deposited on a Nafion[®] film (A). The poor electrochemical signal, using the latter cast-film application, was due to the Nafion[®] film breaking the electrical connection between the glassy carbon disk and the catalyst. In this approach the characteristic wave-shape for dilute acid electrolysis on Pt was indistinguishable.

According to Tripković *et al* [127] Nafion[®] films do not significantly contribute additional mass-transfer resistance making its use as an electrocatalyst binder feasible. Nafion[®] films were also found to have no significant electro-activity when deposited on a glassy carbon electrode (Figure 5.3).



**Figure 5.3. 5% Nafion[®] film electro-activity in 0.5M H₂SO₄
(Sweep rate = 20 mV.s⁻¹)**

In conclusion, formulation of electrocatalyst inks with Nafion[®] solution and application of cast-film electrodes in cyclic and linear-sweep voltammetry provided

the best application method for the electrochemical characterization of nanophase electrocatalysts. This method was therefore applied in all electrochemical analyses.

5.1.4. TOPOGRAPHY OF NANOPHASE ELECTROCATALYST CAST-FILMS

As described in Section 5.1.3, the formulation of electrocatalyst inks with Nafion[®] solution and the application of cast-film electrodes were deemed suitable for the characterization of nanophase electrocatalysts. A study of the topography of these cast-film electrode surfaces, prepared from nanophase electrocatalysts, was conducted. These cast-films were similar to the films deposited on rotating-disk electrodes in the electrochemical characterization using cyclic and linear-sweep voltammetry.

The surface structure of a cast-film fabricated from the commercial JM Pt/C electrocatalyst, supported on HOPG, was studied using SEM, producing the micrograph presented as Figure 5.4.

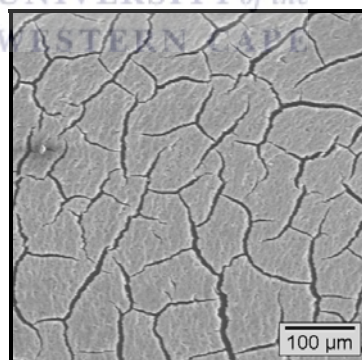


Figure 5.4. Scanning electron micrograph of a JM Pt/C electrocatalyst cast-film, supported on HOPG

In Figure 5.4, the surface of the cast-film deposited on HOPG was not homogeneous and a “dry-river bed” appearance was observed. The cracks in the JM Pt/C cast-film were about 2-μm in width. These cracks are thought to be due to differences in the

coefficient of expansion of the film as opposed to the HOPG during the drying step, whereby solvent is removed from the cast-film. The surface elemental distribution on the JM Pt/C cast-film supported on HOPG was studied using dynamic analysis in PIXE spectroscopy and the elemental distribution map was presented in Figure 5.5 using the experimental parameters presented in Section 3.3.7.

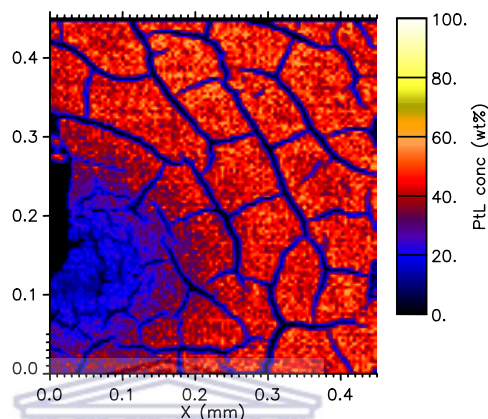


Figure 5.5. Surface elemental distribution map of a JM Pt/C electrocatalyst cast-films supported on HOPG

The surface elemental distribution map in Figure 5.5 shows that a homogeneous surface Pt distribution was attained without significant agglomeration on the JM Pt/C cast-film, but with a large density of cracks also observed. The Pt particles were concentrated in surface “islands” with almost negligible Pt distribution within the cracks on the cast-film surface.

The topography of the JM Pt/C electrocatalyst cast-film prepared as described in Section 5.1.3 was studied using the *imaging mode* in SECM given in Section 3.7. The UME and substrate were polarized under applied potentials to produce images.

A cyclic voltammogram was recorded on the JM Pt/C cast-film prior to the mapping process to determine suitable polarization potentials. The working electrode was the UME, the reference electrode was Ag/AgCl, and the counter electrode was a Pt-wire

coil. The voltammogram was recorded in 5mM H₂SO₄ at a sweep rate of 20 mV.s⁻¹ and is presented in Figure 5.6.

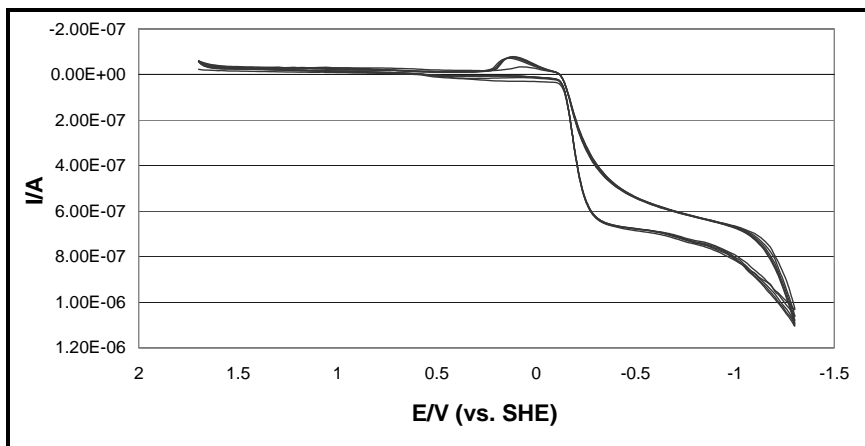


Figure 5.6. Voltammogram for the electrolysis of 5 mM H₂SO₄ on a JM Pt/C cast-film supported on HOPG (sweep rate = 20 mV.s⁻¹) using a Pt UME

Higher UME potentials ≥ -0.6 V_{Ag/AgCl} were found to produce SECM images with lower resolution, whereas potentials around -0.65 V_{Ag/AgCl} were found to produce the best images without rapid bubble formation.

An approach curve analysis was conducted to study the electro-conductivity of the cast-film supported on a HOPG substrate and determine whether imaging of the surface was feasible (Figure 5.7). Approach curves were discussed in Section 3.7.

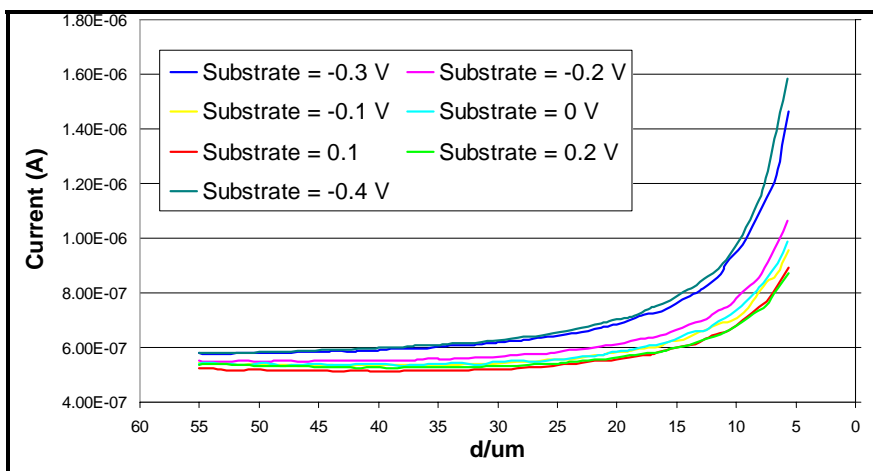


Figure 5.7. Approach curves on a JM Pt/C cast-film supported on HOPG in 5mM H₂SO₄, E_{UME} = 0 V_{Ag/AgCl} (approach speed = 1μm/sec)

From Figure 5.7, a positive feedback was observed on the JM Pt/C cast-film, indicative of an electron-conductive surface. The imaging process was thus confirmed to be feasible on the cast-film surface. Under applied potential the diffusional mass transfer began when the UME was about 30 μm from the substrate surface. At this distance the UME penetrated the hemispherical diffusion shell above the JM Pt/C cast-film. Therefore for an SECM image to be collected, the UME tip was rastered over the cast-film at a tip-substrate separation ≤ 30 μm.

The SECM imaging was conducted using the experimental parameters given in Section 3.7. The SECM map for the study of the topography of a JM Pt/C cast-film prepared as described in Section 5.1.3 is presented in Figure 5.8.

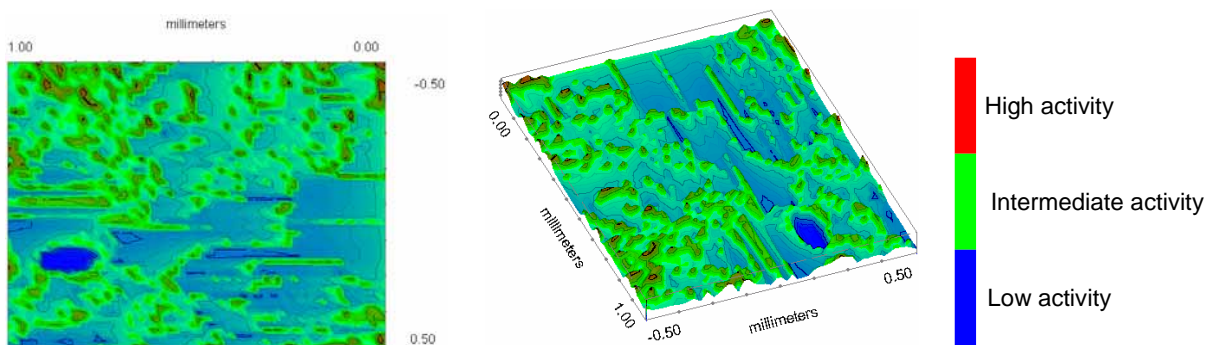


Figure 5.8. Topographical SECM map of a JM Pt/C cast-film on HOPG ($E_{\text{UME}} = -0.65 \text{ V}_{\text{Ag}/\text{AgCl}}$; $E_{\text{HOPG}} = 0.0 \text{ V}_{\text{Ag}/\text{AgCl}}$, scan area = $1000 \times 1000 \text{ }\mu\text{m}$, raster speed = $5 \text{ }\mu\text{m}/\text{sec}$, tip-substrate separation = $5 \text{ }\mu\text{m}$)

The activity, corresponding to the colour, increased in the following order: red (high-activity) > green (intermediate activity) > blue (low activity). The SECM map of the Pt/C cast-film, (Figure 5.8), exhibited large areas of agglomeration which appeared as high-activity areas (reddish-colour) in the map. This agglomeration was not previously observed in Figures 5.4 and 5.5. These agglomerated areas produced maximum perturbation in the UME tip current. Also, the point-of-contact at which the tip-substrate separation was zeroed was observed as a disk-like feature about $200 \text{ }\mu\text{m}$ in diameter. This was in good agreement with the tip diameter observed in Figure 3.2. The disk-like features were due to the removal of a portion of the film after contact was made between the cast-film and the UME. A diverse range of activities was observed over the length of the SECM map, indicative of a surface with heterogeneous activity.

The SECM map presented in Figure 5.8 did not exhibit a good correlation with the appearance of the cast-film surface observed in Figures 5.4 and 5.5. It was very difficult to extract quantitative chemical information from the SECM map. Many further images were collected without improvement in the quantitation. For this reason the technique should be limited to a qualitative role in the characterization of

nanophase electrocatalysts. Also, SECM and PIXE suffered from poor precision due to the inability to structurally reproduce cast-film electrodes. SECM and PIXE would be better utilised in the study of the surface elemental distribution on fuel cell electrodes. This type of information may help in the understanding of the chemical behaviour at the interface between the proton-conducting membrane and the catalyst layers.

5.1.5. INFLUENCE OF METHANOL CONCENTRATION ON THE METHANOL OXIDATION REACTION

Conditions in the voltammetric evaluation of the MOR were copied from the DMFC anode as far as possible in order to correlate data obtained to the behaviour at the DMFC anode. The composition of the electrolyte solution should be evaluated before conclusions can be drawn between the behaviour of the catalyst in the voltammetric experiments conducted and the behaviour of the catalysts in the DMFC. The use of 0.5M H₂SO₄ in the electrolyte has already been evaluated on the basis of the similarities between its pH and the acid capacity of a Nafion[®] solid polymer electrolyte. A range of methanol solution concentrations (0.01-2M) were evaluated in terms of the MOR electro-activity measured using a JM PtRu/C electrocatalyst cast-film deposited on a glassy carbon working electrode. The reference and counter electrodes were saturated calomel and a Pt-wire basket, respectively. The potential was swept from 0-1 V_{SCE} to 0 V_{SCE} at a sweep rate of 20 mV.s⁻¹. The corresponding voltammograms in each concentration of methanol on JM PtRu/C are presented as Figure 5.9.

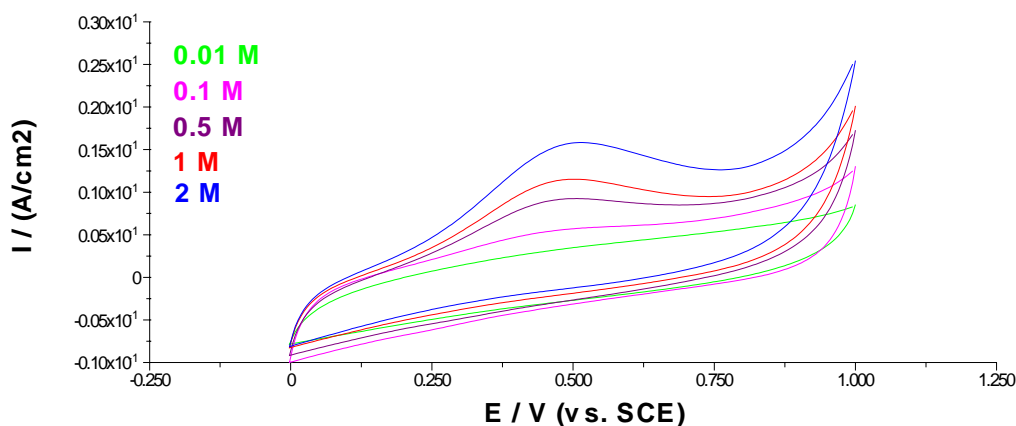


Figure 5.9. Methanol oxidation reaction activity on JM PtRu/C with increasing CH₃OH concentration in 0.5M H₂SO₄ (sweep rate = 20 mV.s⁻¹)

From Figure 5.9, the MOR activity on JM PtRu/C was found to increase with increasing methanol concentration. Also, the anodic peak potential (E_{PA}) moved very slightly to more anodic potentials with increasing methanol concentration, where $E_{PA} = 0.49 \text{ V}_{SCE}$ in 0.5M CH₃OH and $E_{PA} = 0.51 \text{ V}_{SCE}$ in 2M CH₃OH. This observation may be linked to the availability of reagent species with increasing concentration.

Concentrations of 1-2M CH₃OH solutions are typically used in DMFC performance testing, however 2M CH₃OH solutions and higher are associated with high methanol-crossover rates, significant cell potential degradation, and ORR performance-loss at the cathode. As stated by Choi *et al* [134], the problems with high CH₃OH concentrations can be attributed to the high methanol permeability of the Nafion[®] membrane. For these reasons 1M solutions are preferred in electrochemical characterization studies [135]. Also, Easton [18] discussed most DMFC aqueous methanol feeds as being 1M concentrations.

Therefore the MOR activity on nanophase electrocatalysts was determined using an electrolyte consisting of 1M CH₃OH and 0.5M H₂SO₄ in all further nanophase electrocatalyst characterization studies involving the MOR.

5.1.6. INFLUENCE OF NAFION[®] CONTENT ON ELECTROCATALYTIC ACTIVITY

The influence of Nafion[®] content, in electrocatalyst inks, on electrocatalytic activity was evaluated using the MOR. In the electrochemical characterization nanophase electrocatalysts were dispersed in 5% Nafion[®] solution and applied as cast-films to a glassy carbon working electrode as discussed in Section 5.1.3. However, it became important to determine the optimum ink composition for future characterization of nanophase electrocatalysts. The ink composition was optimised on the basis of the PtRu/C-to-Nafion[®] ratio. The ideal ratio was established by characterising JM PtRu/C in 1M CH₃OH and 0.5M H₂SO₄ at a sweep rate of 20 mV.s⁻¹. The working electrode was glassy carbon, the reference electrode was a saturated calomel electrode and the counter electrode was a Pt-wire basket. The corresponding voltammograms are presented in Figure 5.10.

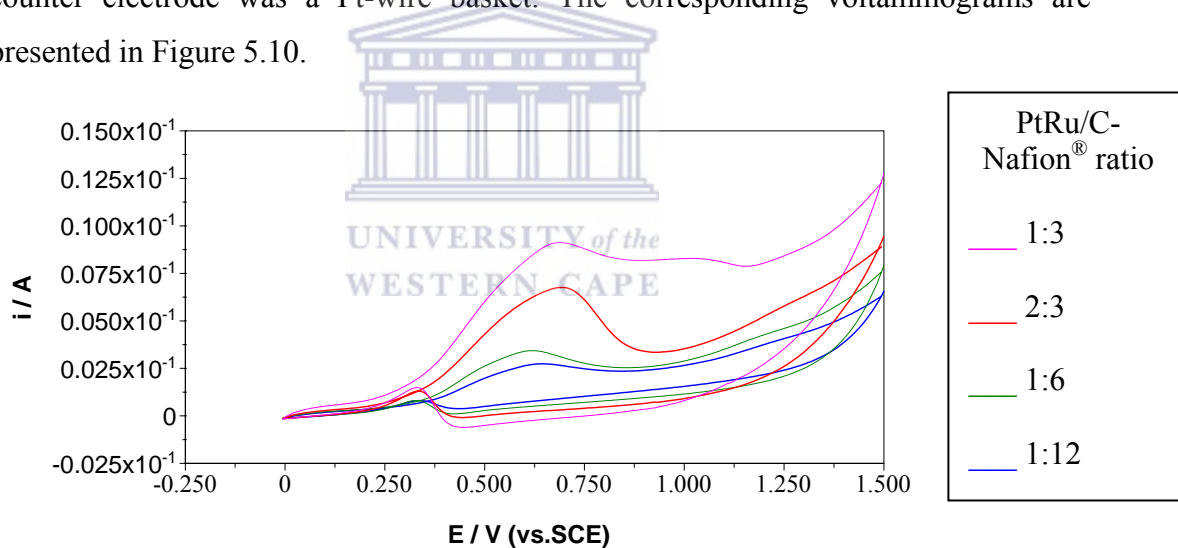


Figure 5.10. Influence of Nafion[®] content on the methanol oxidation reaction on JM PtRu/C in 1M CH₃OH + 0.5M H₂SO₄ (sweep rate = 20 mV.s⁻¹)

In Figure 5.10 it was demonstrated that 14% dry weight Nafion[®] content, corresponding to a PtRu/C-to-Nafion[®] ratio of 1:3, was the optimum ink formulation in the study of the MOR. This value corresponded closely to that determined by Easton [18] who described 15-20% dry weight Nafion[®] content as being optimum in

the MOR. Both i_{PC} ($E_{PC} = 0.31 \text{ V}_{SCE}$) and i_{PA} ($E_{PA} = 0.63\text{-}0.69 \text{ V}_{SCE}$) decreased with a deviation from the 1:3 ink formulation. When increasing the electrocatalyst loading in the ink formulation from 1:3 to 2:3 the electro-activity (i_{PA}) decreased because the quantity of Nafion[®] used could not bind the larger quantity of catalyst used, with the result that some of the catalyst delaminated from the cast-film during cycling. Likewise, by increasing the Nafion[®] content, from 1:3 to 1:6 or 1:12, the fraction of Pt exposed to the electrolyte decreased as Nafion[®] thus acted to block active surface sites from methanol as a result of the bulkiness of the Nafion[®] molecule. It was noted by Easton [18] that high Nafion[®] content in inks lower fuel cell performance as the morphology, low gas permeability, and poor electro-conductivity of Nafion[®] disrupts the three-phase boundary on electrodes. This three-phase boundary exists where the electro-active species, the electrolyte and the electrocatalysts are all present.

According to these results and unless otherwise stated, the 1:3 ink formulation was maintained in the electrochemical screening of nanophase electrocatalysts.

5.1.7. INFLUENCE OF OXYGEN SATURATION ON THE OXYGEN REDUCTION REACTION

The electrochemical response upon oxygen saturation of an acidic electrolyte and in terms of activity towards the ORR was evaluated on a commercial JM Pt/C electrocatalyst. The working electrode was glassy carbon, the reference electrode was saturated calomel, and the counter electrode was a Pt-wire basket. The electrolyte solutions were O₂-saturated and unsaturated 0.5M H₂SO₄. The voltammograms were scanned from 0 V_{SCE} to 0.6 V_{SCE} at a sweep rate of 20 mV.s⁻¹. The corresponding voltammograms are presented in Figure 5.11.

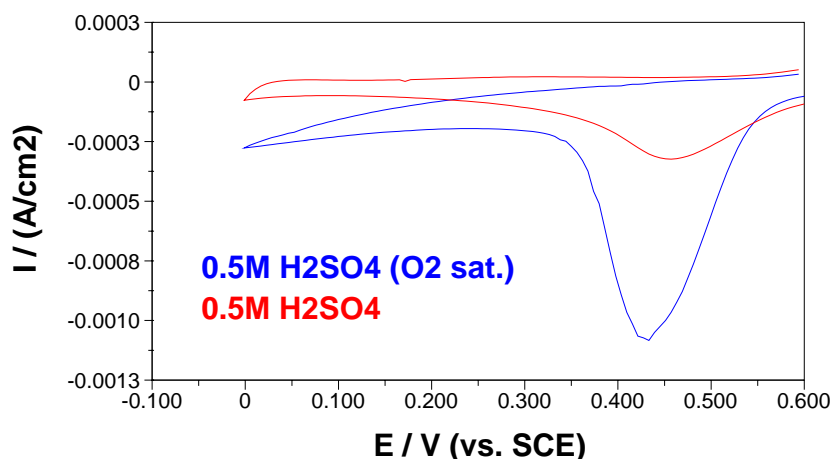


Figure 5.11. Voltammograms for the oxygen reduction reaction on JM Pt/C in O_2 -saturated and unsaturated 0.5M H_2SO_4 (sweep rate = $20 \text{ mV}\cdot\text{s}^{-1}$)

The electrochemical response to the ORR was significantly greater in O_2 -saturated H_2SO_4 compared to unsaturated H_2SO_4 . In addition, a slight shift towards more cathodic potentials was observed upon O_2 -saturation of the electrolyte. Current density $j_{PC} = 1.2 \text{ mA}\cdot\text{cm}^{-2}$ ($E_{PC} = 0.43 \text{ V}_{SCE}$) in O_2 -saturated H_2SO_4 compared to $j_{PC} = 0.4 \text{ mA}\cdot\text{cm}^{-2}$ ($E_{PC} = 0.45 \text{ V}_{SCE}$) in unsaturated H_2SO_4 . In conclusion, electrochemical characterization of nanophase electrocatalysts in terms of the ORR was conducted in O_2 -saturated 0.5M H_2SO_4 because of the greater electrochemical response that could be obtained. O_2 -saturated H_2SO_4 was also used by Antoine *et al* [136] to study the ORR on Pt-based electrocatalysts.

5.2. ELECTROCHEMICAL CHARACTERIZATION OF NANOPHASE ELECTROCATALYSTS

5.2.1. DILUTE ACID ELECTROLYSIS

Dilute acid electrolysis was evaluated on a smooth Pt electrode and compared to that on nanophase JM Pt/C in order to establish the benefit of the nanophase electrocatalyst versus the bulk metal. The electrolyte was 1M H_2SO_4 . The surface

area of the smooth Pt working electrode was 0.07 cm^2 . The potential was swept from $-0.25 \text{ V}_{\text{SCE}}$ to 1 V_{SCE} at a sweep rate of $20 \text{ mV}\cdot\text{s}^{-1}$. The nanophase JM Pt/C electrocatalyst was deposited on a glassy carbon electrode (surface area = 0.07 cm^2). The reference and counter electrodes were saturated calomel and a Pt-wire basket, respectively. The voltammograms are given as Figures 5.12 and 5.13.

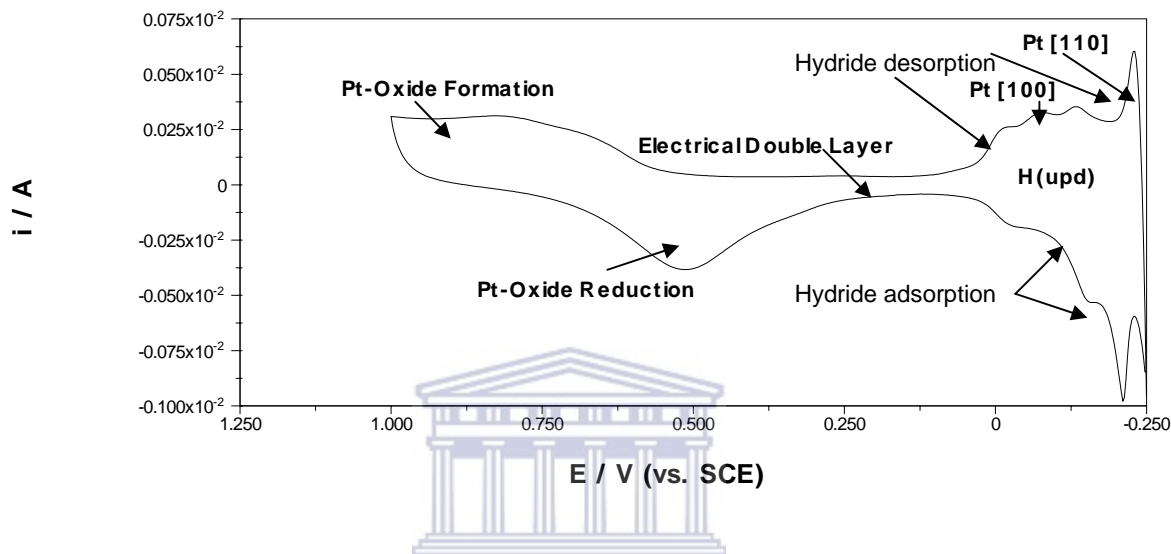


Figure 5.12. Voltammogram for the electrolysis of 1M H_2SO_4 on a smooth Pt electrode (sweep rate = $20 \text{ mV}\cdot\text{s}^{-1}$)

In the electrolysis of dilute acid on a smooth Pt electrode (Figure 5.12), three distinct regions were observed: the hydrogen underpotential deposition (H_{upd}) region consisting of the adsorption/desorption of Pt-hydride species near the H_2 reversible potential ($0.25\text{-}0 \text{ V}_{\text{SHE}}$); the electrical double layer region ($0.25\text{-}0.5 \text{ V}_{\text{SHE}}$) which is an interfacial boundary across which an electrical field exists and at which the electrode surface was relatively clean of adsorbates; and an oxide region consisting of the formation/reduction of stable Pt-oxides ($0.5\text{-}1.25 \text{ V}_{\text{SHE}}$). Typical oxide species that are formed and then reduced in the oxide region include Pt-O and $\text{Pt}(\text{OH})_2$. The H_{upd} region occurs on two distinct crystal facets: (100) and (110), where strongly-adsorbed hydride species are formed on the (100) facets and weakly-adsorbed hydride species are formed on the (110) facets [112].

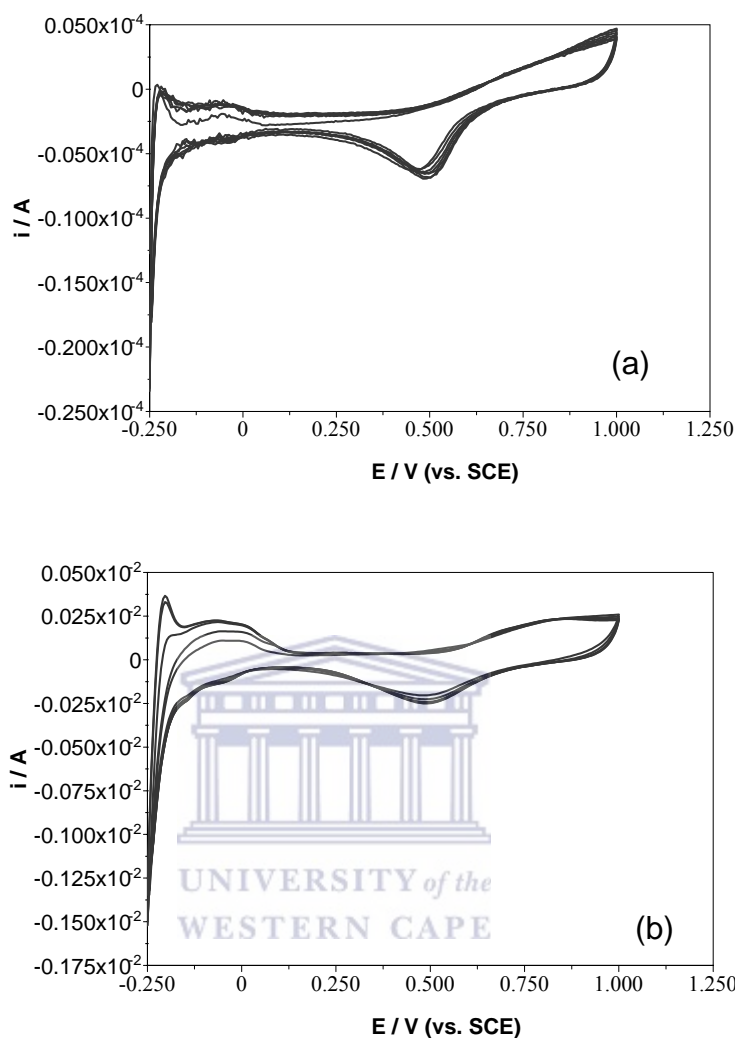


Figure 5.13. Electrolysis of 1M H₂SO₄ on (a) smooth Pt electrode; (b) nanophase JM Pt/C (sweep rate = 20 mV.s⁻¹)

The measured activity on the commercial nanophase JM Pt/C, shown in Figure 5.13 (b), was significantly greater than that on the corresponding smooth Pt electrode in Figure 5.13 (a), on account of the greater surface area of the nanophase Pt/C. In addition, the H_{UPD} region was better resolved on nanophase JM Pt/C than on smooth Pt. Finally, the peak potential for the ORR (E_{PC}) shifted slightly towards more cathodic potentials upon decreasing the Pt particle size to the nanometre domain ($E_{PC} = 0.5 \text{ V}_{SCE}$ on a smooth Pt electrode; $E_{PC} = 0.47 \text{ V}_{SCE}$ on nanophase JM Pt/C).

In conclusion, higher catalytic activity towards the ORR was demonstrated on nanophase Pt/C compared to bulk Pt. This increase was a direct result of the increased active surface area obtained upon decreasing the particle size from the bulk metal to Pt in the nanometre domain.

5.2.2. ELECTROCHEMICAL SCREENING OF NANOPHASE ELECTROCATALYSTS IN POTASSIUM FERROCYANIDE

Cyclic voltammetry was conducted in 0.01M $K_4[Fe(CN)_6]$, supported in 0.1M KCl, to assess the quality of fabricated nanophase electrocatalysts. The methods for the preparation of these novel nanophase electrocatalysts were given in Section 3.1.2 [53, 57-59]. The reversible Fe^{2+}/Fe^{3+} redox couple, in $K_4[Fe(CN)_6]$, supported in 0.1M KCl, was utilised due to its simplicity, convenience, and near-to-ideal behaviour allowing for studies of redox systems: $Fe^{2+} \leftrightarrow Fe^{3+} + \bar{e}$. Nugent *et al* [137] have stated the reaction as being *quasi-reversible* on carbon-based materials with the peak separation $\Delta E_p \geq 0.7$ V, indicative of very slow rates of electron transfer. The applied potential was generally swept between $-0.20 V_{SCE}$ and $0.6 V_{SCE}$ at a sweep rate of $20 mV.s^{-1}$. The working electrode was glassy carbon, the reference electrode was saturated calomel, and the counter electrode was a Pt-wire basket. Results obtained from different electrocatalysts were collected in replicate and the best value presented in each case. Results were tabulated and presented in Table 5.1, and the corresponding voltammograms are attached as APPENDICES C1-4.

Table 5.1. Electrochemical screening of Pt-based nanophase electrocatalysts in 0.01M K₄[Fe(CN)₆], supported in 0.1M KCl (sweep rate = 20 mV.s⁻¹)

Nanophase electrocatalyst	Current density j_{PA} ($\mu\text{A.cm}^{-2}$)	j_{PA}/j_{PC}	E_{PA} (V)	Peak separation $\Delta E_P = E_{PA} - E_{PC}$ (V)	Formal potential $E^0 = [E_{PA} + E_{PC}]/2$ (V)
JM Pt/C	67.2	1.38	0.180	0.118	0.121
JM PtRu/C	120	1.51	0.172	0.110	0.117
Fabricated PtRu/C	49.3	1.56	0.188	0.145	0.116
Pt/C (glycol)	37.6	1.87	0.183	0.120	0.123
Pt/C(1-PrOH/NaOH/pH12)	40.9	1.60	0.180	0.117	0.122
Pt/C(1-PrOH/H ₂ SO ₄ /pH2)	62.2	1.50	0.184	0.124	0.122
Pt/CNT	100	1.46	0.179	0.117	0.121
Pt-plated CNT	34.1	1.82	0.247	0.085	0.205
CA_HMS_Pt_lpg_15	31.9	1.42	0.251	0.110	0.196
CA_HMS_Pt_lpg_30	36.0	1.53	0.188	0.136	0.120
CA_HMS_Pt_lpg_30_red	49.3	1.53	0.174	0.113	0.118
CA_HMS_Pt_lpg_60	48.9	1.36	0.253	0.111	0.198
CA_HMS_Pt_lpg_90	35.1	1.87	0.428	0.372	0.242
CA_HMS_lpg_15_Pt	39.0	1.44	0.278	0.150	0.203
CA_HMS_lpg_30_Pt	32.4	1.53	0.369	0.333	0.203
CA_HMS_lpg_60_Pt	37.6	1.33	0.289	0.167	0.206
CA_HMS_lpg_90_Pt	37.2	1.66	0.330	0.317	0.172
CA_HMS_lpg_90_HSA_Pt	46.4	1.35	0.262	0.123	0.201

In Table 5.1 novel electrocatalysts were compared to commercial JM Pt/C and JM PtRu/C as benchmark materials. Pt/CNT (100 $\mu\text{A.cm}^{-2}$); JM PtRu/C (120 $\mu\text{A.cm}^{-2}$); and Pt/C (1-PrOH/H₂SO₄/pH2) (62.2 $\mu\text{A.cm}^{-2}$) had activities larger or comparable to that of JM Pt/C (67.2 $\mu\text{A.cm}^{-2}$). Pt/CNT and Pt/C (1-PrOH/H₂SO₄/pH2) therefore showed great promise as electrocatalysts. These four materials yielded similar j_{PA}/j_{PC} ratios (≈ 1.4 - 1.5); ΔE_P peak separations (≈ 0.11 - 0.12 V); E^0 values (≈ 0.12 V_{SCE}) and E_{PA} values (≈ 0.17 - 0.18 V_{SCE}). Pt catalysts prepared using 1-propanol as solvent exhibited slightly higher electro-activities than that prepared using glycol as solvent,

suggesting a solvent influence on the activity. There was a significant difference in the electro-activity (j_{PA}) observed on Pt/C(1-PrOH/NaOH/pH12) and Pt/C(1-PrOH/H₂SO₄/pH2), which might indicate that the catalytic activity was influenced by the pH used in the preparation step. This observation was similar to that of Wong *et al* [122] and may be attributed to the incomplete reduction of the Pt precursor onto the carbon support, at high pH.

With regards to mesoporous silica-templated carbon analogues, slightly higher activities were observed upon carbonizing the template after Pt deposition (Pt_lpg), compared to carbonising before Pt deposition (lpg_Pt). The measured electrocatalytic activities of the carbon analogues were too erratic and random to observe a relationship pertaining to the influence of carbonization time on activity. In addition, shifts in E_{PA} were random and could not be attributed to an increase in the carbonization time or the order of deposition. However, the use of high surface area HMS to prepare carbon analogues (i.e. CA_HMS_lpg_90_HSA_Pt) produced higher activities compared to corresponding carbon analogues templated from low surface area HMS. Further reduction of the carbon analogues, using formaldehyde and methanol (i.e. CA_HMS_Pt_lpg_30_red), produced favourable enhancements in the activities of carbon analogues (i.e. higher j_{PA} ; more cathodic E_{PA} ; smaller ΔE_P).

With regards to materials prepared using carbon nanotubes, the impregnation-reduction method (Pt/CNT) produced electrocatalytic materials significantly more active than that produced using electroless-plating (Pt-plated CNT). Pt/CNT produced a higher j_{PA} ; lower j_{PA}/j_{PC} ratio; more cathodic E_{PA} ; and smaller $E^{0'}$, compared to the Pt-plated CNT counterpart, making it a markedly better electrocatalyst. The low activity of Pt-plated CNT may be a result of bulk Pt films of low activity being deposited on the carbon nanotubes in the preparation step.

Finally, JM PtRu/C exhibited superior catalytic activity compared to its fabricated counterpart, where it produced a higher j_{PA} , lower j_{PA}/j_{PC} ratio, more cathodic E_{PA} ,

and a smaller ΔE_p . It also exhibited significantly higher catalytic activity, compared to JM Pt/C. The j_{PA} for the reaction on JM PtRu/C was almost twice the magnitude of j_{PA} for the reaction on JM Pt/C. Ruthenium may therefore have an enhancing effect on the catalytic activity. This was similar to the observations of Radmilović *et al* [32], who found that PtRu-alloy catalysts with 10 wt% Ru composition have catalytic activities two orders of magnitude higher than Pt and several orders higher than Ru. The lowered activity of the fabricated PtRu/C was related to its larger XRD particle size (7.8 nm) determined by Wang [58], compared to the JM PtRu/C (3.48 nm). Also, it was found that in the fabricated PtRu/C the Ru atoms had not alloyed into the Pt structure [58]. This observation is well documented to lead to inferior low-activity PtRu catalysts.

The general wave-shape j_{PA}/j_{PC} on all the electrocatalysts differed from $j_{PA}/j_{PC} = 1$, suggesting the slight non-reversibility of the system on the electrocatalysts.

To summarise, Pt/CNT and Pt/C (1-PrOH/H₂SO₄/pH2) exhibited catalytic activities larger or comparable to that of JM Pt/C. Carbon-supported Pt nanocatalysts prepared using 1-propanol as solvent exhibited slightly higher activities than that prepared using glycol as solvent. Catalytic activity is affected by the pH used in the preparation step, and electrocatalysts prepared from acidic solution exhibited markedly higher catalytic activity compared to electrocatalysts prepared from alkaline solution. The measured electrocatalytic activities of the carbon analogues were too erratic and random to observe a relationship pertaining to the influence of carbonization time on activity. Slightly higher activities were observed upon carbonizing HMS templates after Pt deposition, compared to carbonising before Pt deposition. Using high surface area HMS to prepare carbon analogues led to higher activities compared to carbon analogues templated from lower surface area HMS. Formaldehyde/methanol reduction of carbon analogues produced enhancements in the catalytic activity. The impregnation-reduction method produced superior catalysts

compared to that produced by electroless-plating. And finally, the fabricated PtRu/C was inferior to the JM PtRu/C and the preparation should therefore be revised.

These results show that the $\text{Fe}^{2+}/\text{Fe}^{3+}$ system in potassium ferrocyanide was able to quantitatively discriminate between the activities of various novel nanophase electrocatalysts and can be applied as a tool to optimise catalyst preparation.

5.2.3. ELECTROCHEMICAL CHARACTERIZATION OF NANOPHASE ELECTROCATALYSTS IN THE METHANOL OXIDATION REACTION

The non-reversible MOR was characterized on a smooth Pt electrode, JM Pt/C, JM PtRu/C, and fabricated PtRu/C materials [58]. The nanophase electrocatalysts were deposited as cast-films on a glassy carbon working electrode, the reference electrode was saturated calomel, and the counter electrode was a Pt-wire basket. The electrolyte solution was deaerated 1M CH_3OH in 0.5M H_2SO_4 . The potential range was swept from 0 to 1 V_{SCE} at a sweep rate of $20 \text{ mV}\cdot\text{s}^{-1}$. The corresponding voltammograms are given in Figures 5.14-5.17.

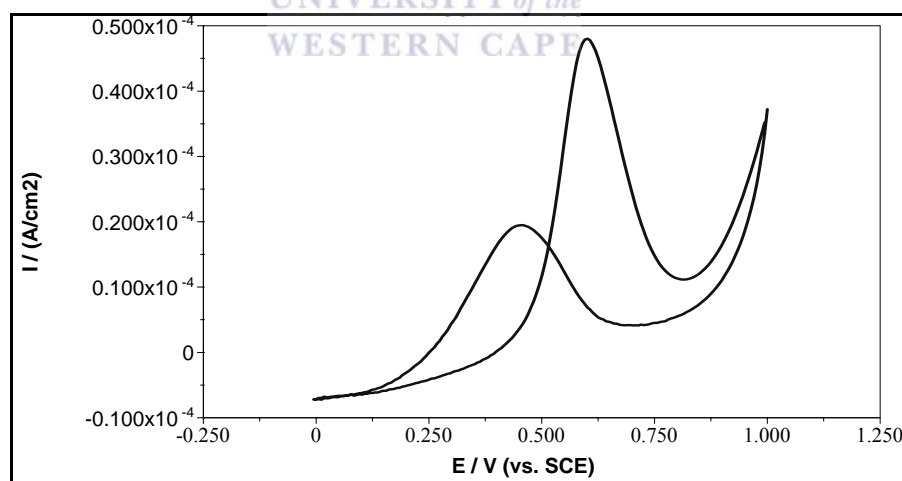


Figure 5.14. Voltammogram for the methanol oxidation reaction on a smooth Pt electrode in 1M CH_3OH + 0.5M H_2SO_4 (sweep rate = $20 \text{ mV}\cdot\text{s}^{-1}$)

According to the data presented in Figure 5.14, four observations can be made regarding the MOR on a smooth Pt electrode: (a) the appearance of a hysteresis at $0.53 \text{ V}_{\text{SCE}}$; (b) the appearance of an oxidation-like peak in the cathodic sweep at $E_{\text{PC}} = 0.46 \text{ V}_{\text{SCE}}$ as a result of the formation of Pt surface sites free of oxides and strongly adsorbed organic residues, such as CO [138]; (c) the absence of the H_{upd} region at $0 \text{ V}_{\text{SCE}} \leq E \leq 0.25 \text{ V}_{\text{SCE}}$; and (d) the appearance of a sharp anodic peak at $E_{\text{PA}} = 0.63 \text{ V}_{\text{SCE}}$ for the oxidation of surface adsorbed species. The characteristic H_{upd} region disappeared in the MOR on smooth Pt as a result of the competition between CH_3OH and H_2 for free surface sites. The two adsorbates cannot exist simultaneously on the Pt surface, and as a result the H_{upd} region disappeared due to the greater surface affinity of Pt towards CH_3OH .

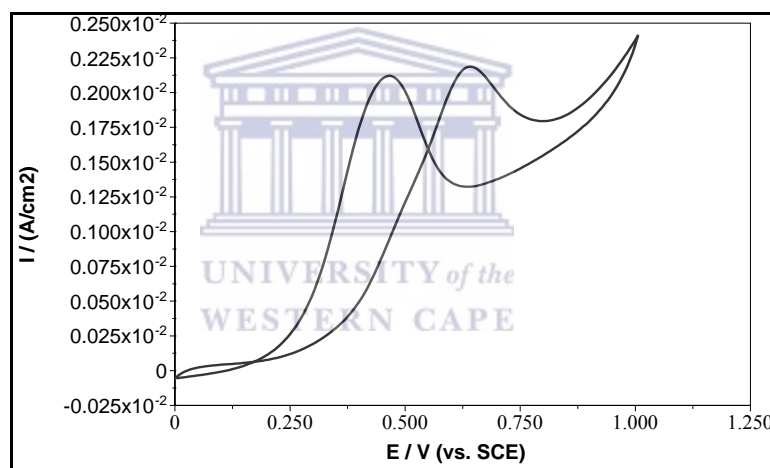


Figure 5.15. Voltammogram for the methanol oxidation reaction on nanophase JM Pt/C in 1M CH_3OH + 0.5M H_2SO_4 (sweep rate = $20 \text{ mV}\cdot\text{s}^{-1}$)

Similar observations were made for the MOR on nanophase JM Pt/C shown in Figure 5.15. However, the hysteresis shifted towards a more anodic potential at $0.56 \text{ V}_{\text{SCE}}$; E_{PA} shifted towards $0.66 \text{ V}_{\text{SCE}}$; and E_{PC} shifted towards $0.47 \text{ V}_{\text{SCE}}$. Also, the anodic and cathodic limiting currents (j_{PA} and j_{PC}) were significantly enhanced upon decreasing the Pt particle size to the nanometre domain. Higher catalytic activity of nanophase Pt towards the MOR was demonstrated compared to the catalytic activity

of smooth Pt. This was a result of the increase in the active surface area upon decreasing the Pt particle size to the nanometre domain.

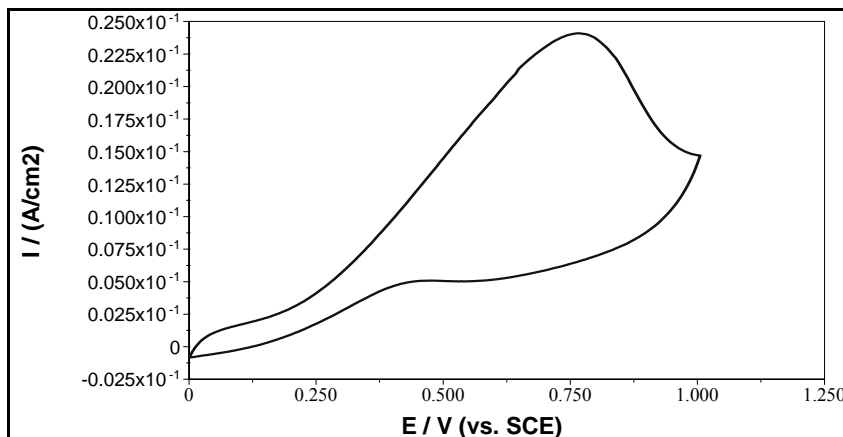


Figure 5.16. Voltammogram for the methanol oxidation reaction on JM PtRu/C in 1M CH₃OH + 0.5M H₂SO₄ (sweep rate = 20 mV.s⁻¹)

In Figure 5.16, the wave-shape for the MOR on commercial nanophase JM PtRu/C differed noticeably from that on JM Pt/C and the smooth Pt electrode. Particularly noteworthy was the absence of the hysteresis previously observed. A slight shift in E_{PC} towards more cathodic values (0.45 V_{SCE}) and a significant shift in E_{PA} towards more anodic values (0.75 V_{SCE}) were observed upon addition of Ru. j_{PC} and j_{PA} were also significantly higher for the MOR on JM PtRu/C, compared to that on JM Pt/C and bulk Pt. This was due to the addition of Ru as a water decomposition promoter.

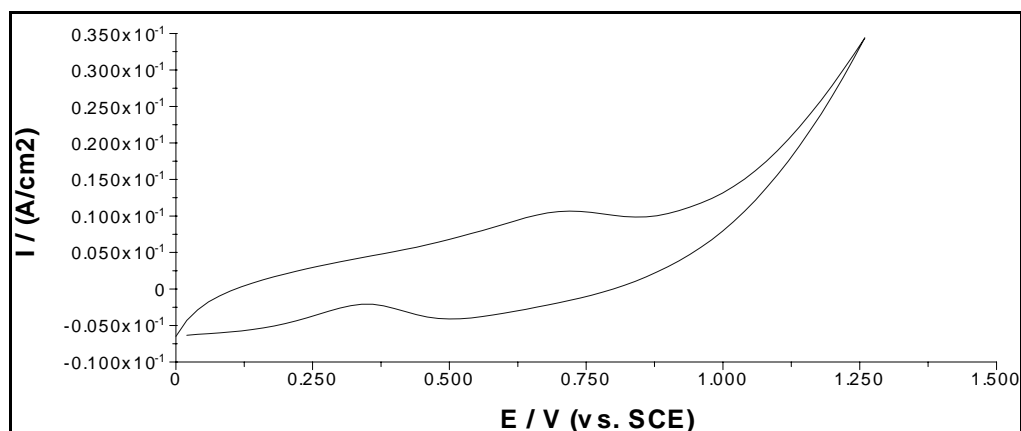


Figure 5.17. Voltammogram for the methanol oxidation reaction on fabricated PtRu/C in 1M CH₃OH + 0.5M H₂SO₄ (sweep rate = 20 mV.s⁻¹)

In terms of the fabricated nanophase PtRu/C electrocatalyst in Figure 5.17, MOR activity significantly lower than that on the JM PtRu/C was observed, where $j_{PA} = 11.3 \text{ mA.cm}^{-2}$ on the fabricated PtRu/C, and $j_{PA} = 23.8 \text{ mA.cm}^{-2}$ on the JM PtRu/C. In addition, the E_{PC} shifted towards 0.35 V_{SCE} and E_{PA} shifted towards 0.72 V_{SCE} , compared to the JM PtRu/C. However, the MOR activities, j_{PA} and j_{PC} , were halved for the reaction on the fabricated PtRu/C, compared to that on the JM PtRu/C. Wang [58] observed that although EDS studies confirmed that Ru was dispersed on the carbon support surface, XRD studies established that Ru atoms had not alloyed into the Pt lattice, with the conclusion that Ru and Pt particles were isolated on the carbon support of the fabricated PtRu/C. This arrangement was unfavourable for the MOR on PtRu-based catalysts as the MOR is optimised when Pt and Ru are alloyed. This was because Pt and Ru active surface sites would be adjacent to each other upon alloying, which was necessary for the Langmuir-Hinshelwood mechanism of the oxidative removal process [46]. The active surface sites in the fabricated PtRu/C were relatively far apart with the result that the Langmuir-Hinshelwood mechanism of reaction could not occur efficiently and low MOR activities were recorded, compared to JM PtRu/C. It is recommended that the methodology for the preparation of fabricated PtRu/C be revised to produce sufficient alloying between Pt and Ru. This observation further demonstrates the technological polymorphism of nanophase electrocatalysts such as PtRu/C. Also, the XRD particle sizes were determined to be 7.8 nm compared to 3.48 nm in the case of the JM PtRu/C catalyst [58]. This may demonstrate a particle size effect on the MOR activities of nanophase PtRu/C electrocatalysts.

Results for the voltammetric study of the MOR on nanophase materials were tabulated and presented in Table 5.2. All results were collected in replicate and the results were compared to that of a smooth Pt electrode.

**Table 5.2. MOR activity on Pt-based materials in 1M CH₃OH + 0.5M H₂SO₄
(Sweep rate = 20 mV.s⁻¹)**

Material	E_{PA} (V _{SCE})	j_{PA} (mA.cm ⁻²)	E_{PC} (V _{SCE})	j_{PC} (mA.cm ⁻²)
Smooth Pt Electrode	0.63	0.05	0.46	0.02
JM Pt/C	0.66	2.21	0.47	2.13
JM PtRu/C	0.75	23.8	0.45	5.0
Fabricated PtRu/C	0.72	11.3	0.35	2.5

Another major observation was the deterioration of the electrochemical signal with prolonged cycling on Pt, observed in Figure 5.18.

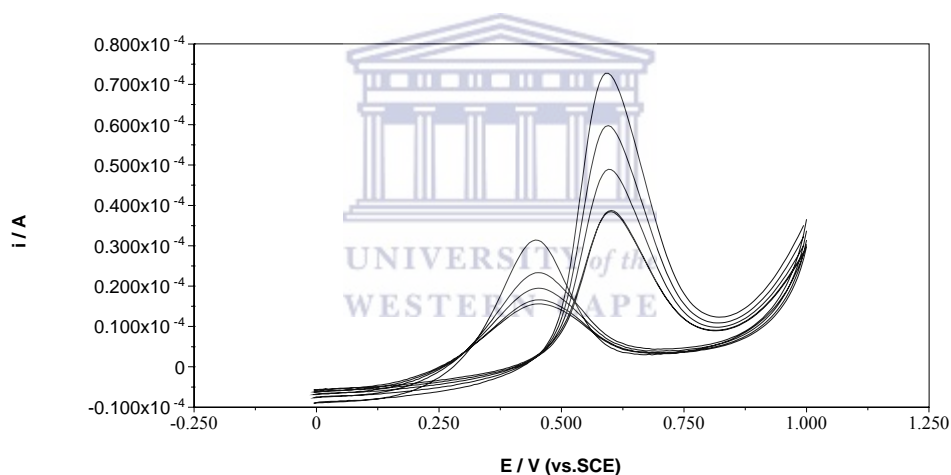


Figure 5.18. Deterioration of the electrochemical signal with CO_{ad} poisoning of smooth Pt in 1M CH₃OH + 0.5M H₂SO₄ (sweep rate = 20 mV.s⁻¹)

This type of behaviour was indicative of the high CO_{ad} poisoning rate of Pt and the CO_{ad} tolerance of Ru-containing materials in the presence of methanol. CO_{ad} poisoning rates were observed to increase in the following order: Smooth Pt > JM Pt/C > JM PtRu/C. The formation of stable Pt-CO_{ad} surface species inhibited the reduction of fresh adsorbates to active sites leading to the subsequent deterioration of the electrochemical signal in the MOR.

A mass transfer study was conducted to determine the diffusion coefficient of the MOR on JM PtRu/C, in comparison to that of the MOR on a smooth Pt electrode. The diffusion coefficients were calculated using the equation given in Section 3.6 and the corresponding Randles-Sevcik plots are given in Figure 5.19.

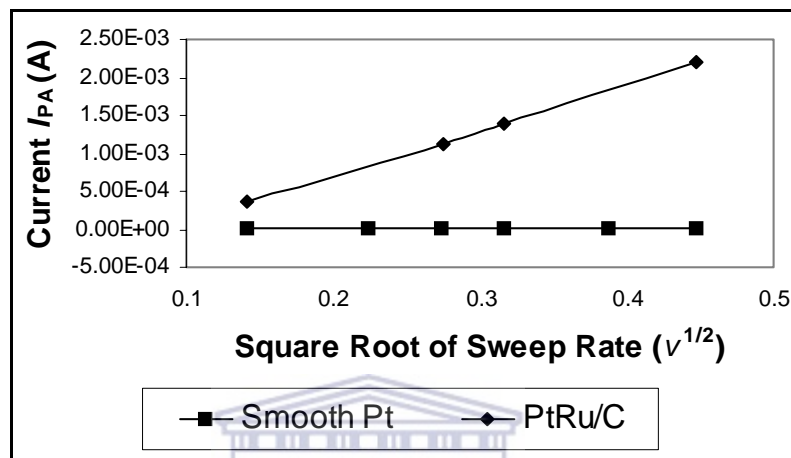


Figure 5.19. Randles-Sevcik plots of the methanol oxidation reaction on JM PtRu/C and smooth Pt in 1M H₂SO₄ + 0.5M CH₃OH

The significantly higher mass transfer properties of the JM PtRu/C electrocatalyst, compared to a smooth Pt electrode were demonstrated in Figure 5.19. The rate of availability of the reagent species was therefore faster and more efficient on nanophase JM PtRu/C. The diffusion coefficients for the MOR on a smooth Pt electrode and nanophase JM PtRu/C are given as follows:

$$D(\text{smooth Pt}) = 1.92 \times 10^{-14} \text{ cm}^2/\text{sec}; \quad D(\text{JM PtRu/C}) = 4.2 \times 10^{-10} \text{ cm}^2/\text{sec}.$$

In conclusion, higher MOR activities were demonstrated upon decreasing the Pt particle size to the nanometre domain compared to that on the smooth Pt electrode. Higher MOR activity upon the addition of Ru to the electrocatalyst composition, compared to Pt/C, was demonstrated. A fabricated nanophase PtRu/C electrocatalyst exhibited significantly lower MOR activity, compared to that of the commercial JM PtRu/C. This was a result of the incomplete alloying of Ru into the Pt lattice in the

electrocatalyst preparation step, as determined by Wang [58]. The preparation methodology for fabricated PtRu/C required revision to ensure the alloying of Ru into Pt and smaller PtRu particle sizes. A particle size influence on MOR activity was demonstrated on PtRu/C nanophase electrocatalysts. Deterioration in the MOR activity was observed, upon continual cycling on all nanophase electrocatalysts analysed, and was a result of CO_{ad} -poisoning, where PtRu/C exhibited the highest CO_{ad} -poisoning tolerance. Finally, the mass transfer properties observed for the MOR on nanophase JM PtRu/C was significantly higher than that on smooth Pt.

5.2.4. ELECTROCHEMICAL CHARACTERIZATION OF NANOPHASE ELECTROCATALYSTS IN THE OXYGEN REDUCTION REACTION

A voltammetric study was conducted for the ORR on JM Pt/C; smooth Pt; fabricated carbon-supported Pt; CNT-supported Pt; and mesoporous silica-supported Pt catalysts, prepared using methods given in Section 3.1.2 [53, 57-59]. The ORR was conducted in O_2 -saturated 0.5M H_2SO_4 between -0.25 to 1.0 V_{SCE} at a sweep rate of 20 $\text{mV}\cdot\text{s}^{-1}$. Nanophase electrocatalysts were deposited as cast-films onto a glassy carbon working electrode, the reference electrode was saturated calomel, and the counter electrode was a Pt-wire basket. Current densities (j_{PC}) and peak potentials (E_{PC}) for the ORR were observed and recorded. Voltammetric results for the ORR on Pt-based electrocatalysts are presented in Table 5.3 and an example of a voltammogram representing the ORR current increase with increasing sweep rate is given as APPENDIX D. Voltammetric results were replicated. Also, the mass transfer properties of the ORR on Pt-based electrocatalysts were studied in O_2 -saturated 0.5M H_2SO_4 . Mass transfer results are illustrated and tabulated in Figure 5.20 and Table 5.3, respectively.

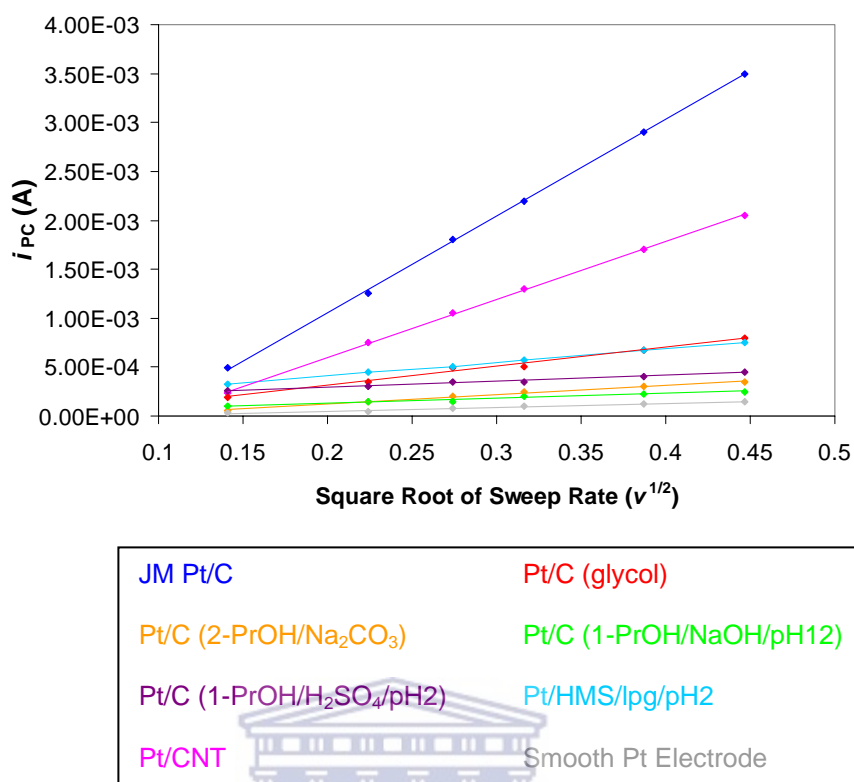


Figure 5.20. Randles-Sevcik plots for the oxygen reduction reaction on Pt-based nanophase electrocatalysts in O₂-saturated 0.5M H₂SO₄

Table 5.3. Voltammetric and mass transfer property study of the oxygen reduction reaction on Pt-based electrocatalysts in O₂-saturated 0.5M H₂SO₄

Material	XRD particle size (nm)	i_{PC} (μ A) at 20 mV.s ⁻¹	j_{PC} (mA.cm ⁻²) at 20 mV.s ⁻¹	E_{PC} (V _{SCE})	Diffusion Coefficient, D (cm ² /sec)
Smooth Pt Electrode	-	33.2	0.47	0.404	8.19×10^{-13}
JM Pt/C	4.23	490	7.00	0.346	1.83×10^{-8}
Pt/C (glycol)	11.43	196	2.80	0.424	9.24×10^{-10}
Pt/C (2-PrOH/Na ₂ CO ₃)	-	57.5	0.82	0.472	2.79×10^{-10}
Pt/C (1-PrOH/H ₂ SO ₄ /pH2)	2.59	257	3.67	0.390	1.32×10^{-10}
Pt/C (1-PrOH/NaOH/pH12)	2.56	98.0	1.40	0.349	1.21×10^{-10}
Pt/HMS/lpg/pH2	-	320	4.57	0.452	5.05×10^{-10}
Pt/CNT	1.99	233	3.33	0.514	7.11×10^{-9}

As observed in Table 5.3, catalytic activity (j_{PC}) for the ORR on the commercial JM Pt/C was significantly higher than that on the other electrocatalysts. JM Pt/C can be regarded as the best electrocatalyst for use in the ORR of the DMFC, hence its employment in many fuel cell research laboratories. JM Pt/C also exhibited the best mass transfer properties, as evidenced by the high diffusion coefficient, which was at least one order larger than that on the other electrocatalysts analysed. ORR therefore occurred at a faster rate on JM Pt/C compared to the other electrocatalysts analysed as the diffusion coefficient can be related to the availability of the reagent species for the surface reaction. Also, there was a very significant enhancement in ORR activity and diffusion coefficient on JM Pt/C compared to smooth Pt, demonstrating the increase in electrocatalytic activity and mass transfer properties gained upon increasing the surface area of Pt by decreasing the particle size to the nanometre domain.

ORR activity on Pt/CNT was lower and had a large shift towards more anodic potentials ($E_{PC} = 0.514 \text{ V}_{SCE}$), compared to the ORR on JM Pt/C. In terms of mass transfer properties, ORR on Pt/CNT performed fairly well compared to JM Pt/C. ORR on Pt/CNT exhibited a notably higher diffusion coefficient compared to the other prepared nanophase electrocatalysts.

ORR on nanophase electrocatalysts prepared using propanol as solvent: Pt/C (1-PrOH/ $\text{H}_2\text{SO}_4/\text{pH}2$); Pt/C (1-PrOH/ $\text{NaOH}/\text{pH}12$); and Pt/C (2-PrOH/ Na_2CO_3), performed poorly in terms of mass transfer properties and ORR activity. Also, the Pt/C prepared using 2-PrOH as solvent exhibited lower ORR activity (j_{PC}) at a more anodic E_{PC} with a higher diffusion coefficient, compared to Pt/C prepared using 1-PrOH as solvent. This observation demonstrates the technological polymorphism and a solvent influence in electrocatalysts used in the ORR study. The pH had a significant influence on the ORR activity, where nanophase catalysts prepared from acidic solvents exhibited higher activity compared to their alkaline counterparts. Future preparation of Pt/C should therefore be conducted in acidic media.

Pt/C (glycol) exhibited low ORR activity compared to JM Pt/C. The mass transfer properties of Pt/C (glycol) were higher than that of Pt/C prepared using propanol as solvent, despite having a significantly larger particle size = 11.43 nm. It however exhibited a significantly lower diffusion coefficient compared to JM Pt/C.

The mesoporous silica-supported Pt/HMS/lpg/pH2, prepared by the method given in Section 3.1.2, exhibited a lower j_{PC} ; large anodic shift in the E_{PC} ; and a lower diffusion coefficient, compared to JM Pt/C. It exhibited the highest catalytic activity (j_{PC}) of all the fabricated materials (Table 5.3). This observation was difficult to explain. However, open framework structure supports, such as mesoporous hexagonal silica, have been stated to provide the best support for Pt electrocatalysts in the ORR [139]

A particle size effect in the ORR activity, on Pt-based nanophase electrocatalysts, was difficult to observe as activities and particle sizes were too random or erratic to identify a trend. This observation was similar to that of Komanicky *et al* [140] who stated that the study of a particle size effect on Pt electrocatalysts in the ORR often produced contradictory results.

According to Marković *et al* [3] low currents are usually measured in the ORR in acidic electrolytes, even on the best catalysts, partially due to the relatively low activity of Pt towards the ORR.

In conclusion, JM Pt/C exhibited significantly higher ORR activity and mass transfer properties compared to the various fabricated Pt/C electrocatalysts. Large enhancements in ORR activity and mass transfer properties were demonstrated upon decreasing the Pt particle size to the nanometre domain. Fabricated carbon-supported Pt nanophase electrocatalysts exhibited lower ORR activities compared to the JM Pt/C. No pH-influence on the ORR activity was observed. A particle size effect in the ORR activity on Pt-based electrocatalysts was not observed. It is assumed that the JM

Pt/C electrocatalyst possessed certain additional physico-chemical properties that enhance its behaviour in the ORR. These properties may not have been distinguished by the characterization applied in this work and may not be observed in the fabricated materials.

5.2.5. ELECTROCHEMICAL CHARACTERIZATION OF NANOPHASE ELECTROCATALYSTS IN THE OXYGEN EVOLUTION REACTION

The oxygen evolution reaction (OER) constituted the anodic reaction in water electrolysis in a SPE-electrolyser for the production of H₂. The overall reaction for the OER in water electrolysis is given as follows: $2\text{H}_2\text{O} \rightarrow 4\text{H}^+(\text{aq}) + \text{O}_2 + 4\bar{e}$

The OER was investigated on commercial and fabricated nanophase IrO₂ electrocatalysts in 0.5M H₂SO₄. The potential range was swept from -0.25 to 1.25 V_{SCE} at a sweep rate of 20 mV.s⁻¹ according to a procedure given by Rasten *et al* [52]. The working electrode was a cast-film prepared from an IrO₂ ink and deposited on a glassy carbon electrode, the reference electrode was saturated calomel, and the counter electrode was a Pt-wire basket. Results were collected in replicate. The voltammogram for JM IrO₂ is presented in Figure 5.21.

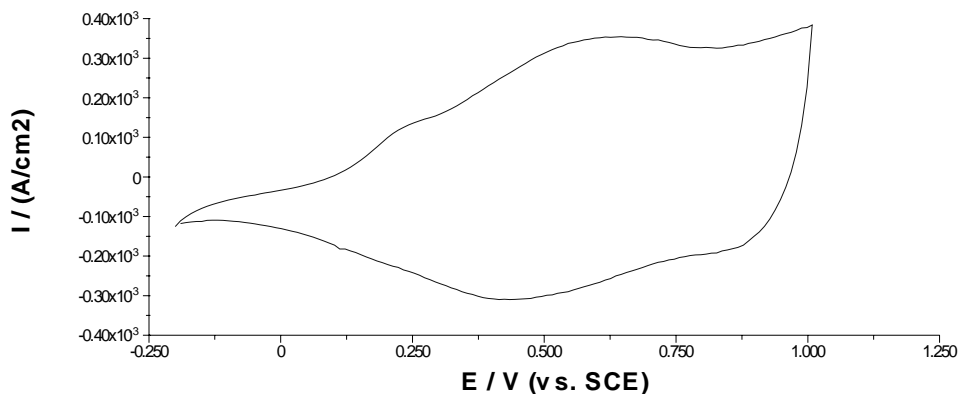


Figure 5.21. Voltammogram for the oxygen evolution reaction on JM IrO₂ in 0.5M H₂SO₄ (sweep rate = 20 mV.s⁻¹)

A reversible set of peaks, in Figure 5.21, at $E_{PA} = 0.63 \text{ V}_{SCE}$ and $E_{PC} = 0.44 \text{ V}_{SCE}$ was observed and may be attributed to an $\text{Ir}^{3+}/\text{Ir}^{4+}$ surface transition, similar to that observed by Rasten *et al* [52]. The $\text{Ir}^{3+}/\text{Ir}^{4+}$ transition mechanism is based on the ion-electronic injection or ejection of H^+ and OH^- onto the IrO_2 surface, compensating for the change in the charge on the oxide film. The hydrated oxide is formed on the IrO_2 electrode surface. A pre-oxidation peak was observed at $E_{PA} = 0.22 \text{ V}_{SCE}$. Its origin may be related to the hydration of the oxide film on Ir, probably with the formation of IrOOH [141]. A current tail of capacitive nature was also observed in the cathodic region of the voltammogram from 0.125 V_{SCE} to -0.25 V_{SCE} .

Unfortunately, the OER could not be characterized on the fabricated IrO_2 nanophase electrocatalyst due to difficulties associated with the disintegration of the cast-film layer by rapid bubble formation in the highly anodic potential region. In addition, the analytical signal did not differ from the background signal.

This reaction is shown to be able to determine the activity of unsupported nanophase JM IrO_2 electrocatalysts that could be applied as an anode electrocatalyst in the SPE-electrolyser and could thus be used in future as a screening technique or benchmark for novel IrO_2 catalysts.

5.2.6. ELECTROCHEMICAL CHARACTERIZATION OF NANOPHASE ELECTROCATALYSTS IN THE HYDROGEN EVOLUTION REACTION

The voltammetric study of HER activity on Pt-based mesoporous silica-templated carbon analogues, carbon black supported electrocatalysts, and carbon nanotube supported electrocatalysts was studied in deaerated $0.5\text{M H}_2\text{SO}_4$. These materials were prepared by methods discussed in Section 3.1.2 [57, 59]. Initially, the potential range was swept from 0 V_{SCE} to -1.7 V_{SCE} which was in the hydrogen evolution region. This produced poor and untidy results and for this reason the potential range was reduced to 0 V_{SCE} to -1.25 V_{SCE} . The current densities for the HER on the

electrocatalysts were then recorded at the vertex potential of $-1.25 V_{SCE}$. The working electrode was electrocatalyst cast-films deposited on a glassy carbon electrode, the reference electrode was saturated calomel, and the counter electrode was a Pt-wire basket. The HER activities of fabricated nanophase catalysts were compared to that of a JM Pt/C catalyst. Initially, the analysis was conducted using CV which led to poor and non-reproducible results. Also the electrochemical response was featureless in the cathodic and anodic sweeps and only an increase in the cathodic current was observed. For this reason LSV was used in the analysis of HER activity on Pt-based nanophase electrocatalysts and was found to be more accurate and presentable. Voltammograms are attached as APPENDICES E1-3. HER activities (j_{PC}) on Pt-based nanophase electrocatalysts were recorded in replicate and are presented in Table 5.4.



Table 5.4. Hydrogen evolution reaction electrocatalytic activities on Pt-based nanophase electrocatalysts in deaerated 0.5M H₂SO₄ (sweep rate = 20 mV.s⁻¹)

Nanophase electrocatalyst	Current density j_{PC} (mA.cm ⁻²)
JM Pt/C	9.70
Pt/C (glycol)	7.90
Pt/C (1-PrOH)	7.30
Pt/C (1-PrOH/H ₂ SO ₄ /pH2)	9.00
Pt/C (1-PrOH/NaOH/pH12)	8.00
Electroless-plated_Pt/CNT	5.88
Pt_CNT	13.5
CA_HMS_Pt_lpg_15	8.60
CA_HMS_Pt_lpg_30	8.90
CA_HMS_Pt_lpg_30 red	8.90
CA_HMS_Pt_lpg_60	8.20
CA_HMS_Pt_lpg_90	6.00
CA_HMS_lpg_15_Pt	6.92
CA_HMS_lpg_30_Pt	6.38
CA_HMS_lpg_60_Pt	5.77
CA_HMS_lpg_90_Pt	10.0
CA_HMS_lpg_90_HL_Pt	5.48

As shown in Table 5.4, Pt/CNT once again was shown to be highly active and exhibited higher HER activity (13.5 mA.cm⁻²) compared to that of the JM Pt/C electrocatalyst (9.7 mA.cm⁻²). This observation was similar to that observed in Section 5.2.2. The high HER activity of Pt/CNT warrants testing of this material in a membrane electrode assembly for hydrogen evolution. The observed high HER activity of Pt/CNT could be credited to the formation of smaller Pt nanoparticles (larger surface area) on the CNT support (1.99 nm by XRD) and the highly conductive nature of the support, as determined by Ying [57]. Overall, the following

fabricated materials exhibited HER activities comparable to that of the commercial JM Pt/C: Pt/C (1-PrOH/H₂SO₄/pH2); Pt/C (1-PrOH/NaOH/pH12); Pt_CNT; CA_HMS_lpg_90_Pt; CA_HMS_Pt_lpg_15; CA_HMS_Pt_lpg_30; CA_HMS_Pt_lpg_30 red; CA_HMS_Pt_lpg_60. The comparable activities of the carbon black- and carbon nanotube-supported Pt catalysts could be credited to their small particle sizes [57].

The inferiority of electroless-plated_Pt/CNT, in terms of HER catalytic activity, was once again demonstrated. This inferiority was previously observed in Section 5.2.2. This may be a result of bulk Pt films of low activity being deposited on the carbon nanotubes of electroless-plated_Pt/CNT. Compared to Pt/CNT, prepared by the impregnation-reduction method, electroless-plated_Pt/CNT produced significantly lower HER activities. Nanophase electrocatalysts for the HER can therefore viably be prepared using the impregnation-reduction method.

In terms of fabricated carbon-supported Pt catalysts, Pt/C (glycol); Pt/C (1-PrOH/H₂SO₄/pH2); Pt/C (1-PrOH/NaOH/pH12) all exhibited satisfactory HER activities while Pt/C (1-PrOH) exhibited a slightly lower HER activity. There may exist a pH-influence on the HER activity of these catalysts where the introduction of an acidic pH-regulator, H₂SO₄, during preparation led to higher activity compared to the activity upon the addition of an alkaline pH-regulator, NaOH. This observation was similar to that of Wong *et al* [122] and that observed in Section 5.2.2 and may be attributed to the incomplete reduction of the Pt precursor onto the carbon support at high pH.

Preparation variables of mesoporous silica-templated carbon analogues were investigated in terms of their measured HER electrocatalytic activity. These variables included: (a) *the influence of carbonization time*; (b) *the influence of the order of deposition*; (c) *the influence of methanol/formaldehyde reduction*. The following

observations were summarised with regard to the HER activity measured in the analysis:

- (a) *Influence of carbonization time*: Generally, the measured HER electrocatalytic activities of the carbon analogues were too erratic and random to observe a relationship pertaining to the influence of carbonization time on HER activity.
- (b) *Influence of the order of deposition*: Generally, higher HER activities were exhibited when the order of deposition was platinization/carbonization (Pt_lpg), compared to carbonization/platinization (lpg_Pt). Similarly, carbonization after Pt deposition produced higher catalytic activities when the carbon analogues were screened in 0.01M $K_4[Fe(CN)_6]$ in Section 5.2.2.
- (c) *Influence of methanol/formaldehyde reduction*: No relationship could be observed between methanol/formaldehyde reduction and measured HER activity. Methanol/formaldehyde reduction was used in converting Pt^x species into the metallic state, Pt^0 . However, when screening the carbon analogues in 0.01M $K_4[Fe(CN)_6]$, carbon analogues reduced with methanol/formaldehyde produced higher activities than those which were unreduced. The methanol/formaldehyde reduction step is deemed advantageous, but not necessary for the carbon analogues prepared for the HER.
- CA_HMS_Pt_lpg_30 and CA_HMS_Pt_lpg_30_red exhibited identical HER activity ($j_{PC} = 8.90 \text{ mA/cm}^2$), suggesting that liquefied petroleum gas carbonization may auto-reduce the Pt in the carbon analogues.

To summarise the results: Pt/CNT exhibited higher HER activity compared to the JM Pt/C, currently used in the MEA cathode of the SPE-electrolyser. Testing of Pt/CNT in an electrolyser was therefore a future recommendation. Good HER activities were exhibited by a range of mesoporous silica-templated carbon analogues, and carbon-supported electrocatalysts which were comparable to that of the JM Pt/C

electrocatalyst. Preparation variables were optimised and require implementation in future fabrication of mesoporous silica-templated carbon analogues for the HER.

5.2.7. ELECTROCHEMICALLY-ACTIVE SURFACE AREA OF PLATINUM-BASED NANOPHASE ELECTROCATALYSTS

The electrochemically-active surface area of fabricated Pt-based nanophase electrocatalysts was evaluated in 1M H₂SO₄, according to the method specified in Section 3.6. All surface areas determined were compared to that of commercial JM Pt/C. The potential range was swept from -0.25 to 1 V_{SCE} at a sweep rate of 20 mV.s⁻¹. The working electrode was a cast-film deposited on a glassy carbon electrode, the reference electrode was saturated calomel, and the counter electrode was a Pt-wire basket. The total metal surface area (SA_{Pt/C}) was determined using an equation presented by Prabhuram *et al* [25]: $SA_{Pt/C} = 6000/[(d)(\rho)]$, where d = density of Pt (21.4 g/cm³); and ρ = particle diameter (nm). The electrochemically-active surface area was determined using an equation presented by Schmidt *et al* [133]: $S_A = Q_H/210 \mu\text{C.cm}^{-2}$, where 210 $\mu\text{C.cm}^{-2}$ is the theoretical charge for full hydride monolayer coverage ($\theta_H = 1 \text{ ML}$) in H₂ adsorption/desorption on Pt (Figure 5.12). Results are presented in Table 5.5. Results were collected in replicate. The electrochemically active Pt utilization is described as the percentage of the available Pt metal surface area which was electrochemically active in the reaction (dilute acid electrolysis on Pt).

Table 5.5. Electrochemically-active surface areas of Pt-based nanophase electrocatalysts (sweep rate = 20 mV.s⁻¹)

Nanophase electrocatalyst	Particle size by XRD (nm)	Metal surface area SA _{Pt/C} (m ² /g)	Integrated peak area (10 ⁻³ C)	Electrochemically active surface area (m ² /g)	Electrochemically active Pt utilization (%)
JM Pt/C	4.23	66.19	4.42	42.51	64.2
			4.38	42.13	63.7
			4.36	41.93	63.3
			4.06	39.05	59.0
			$x = 4.31$	$x = 41.45$	$x = 62.6$
Pt/C (1-PrOH/H ₂ SO ₄ /pH2)	2.59	108.1	1.52	14.62	13.5
Pt/C (1-PrOH/NaOH/pH12)	2.56	109.4	1.47	14.14	12.9
Pt/C (glycol)	11.43	24.5	0.996	9.58	39.1
Pt/CNT	1.99	140.7	1.39	13.37	9.50

From Table 5.5, the metal surface area of commercial JM Pt/C was calculated as 66.19 m²/g compared to the reference value of 62 m²/g specified by the supplier, Johnson Matthey[®] [26]. JM Pt/C exhibited a satisfactory electrochemically active surface area whereas those of Pt/C (glycol), Pt/C (1-PrOH/H₂SO₄/pH2), Pt/C (1-PrOH/NaOH/pH12), and Pt/CNT were deemed poor. The low electrochemically active surface area of Pt/CNT was not expected as the catalyst had previously exhibited high catalytic activity in Sections 5.2.2 and 5.2.6. This occurrence may demonstrate the limited accuracy of the technique. It should be noted that Easton [18] overestimated the electrochemically-active surface area, confirming the somewhat erratic results obtained using this technique. Shan and Pickup [142] also demonstrated the limited absolute accuracy of the technique. This may be a result of the deactivating behaviour of the Nafion[®] binder or a low density of available (100) and (110) Pt facets, during the H_{UPD} surface reactions.

It was previously determined in Section 5.1.3 that Nafion[®] exhibited low electroactivity and makes no meaningful contribution to the analytical signal. Bulky Nafion[®] molecules may also block active species from the active surface sites.

A low density of Pt(110) and (100) facets may also account for the poor electrochemically active surface areas of Pt/C (glycol), Pt/C (1-PrOH/H₂SO₄/pH2), Pt/C (1-PrOH/NaOH/pH12), and Pt/CNT under the conditions tested [32, 143].

Another assumption is that bisulphate anions (SO₄²⁻) and hydroxide adsorbates (OH)_{ad} from the electrolyte may have adsorbed onto the Pt surface during the analysis and acted to deactivate the Pt surface sites. This observation was shared by Marković *et al* [144] who noted that bisulphate anions and hydroxide adsorbates from the H₂SO₄ electrolyte acted to deactivate Pt surface sites of the electrocatalyst.

A limitation of the technique was the assumption of a surface charge of 210 μC/cm² per hydride monolayer. This value pertained to smooth electrode surfaces and not to a multitude of rough nanophase Pt surfaces [133]. The value was also subject to numerous uncertainties [102].

A particle size effect on the electrochemically active surface area of the Pt-based nanophase electrocatalysts was not observed.

In conclusion, the procedure for the determination of electrochemically-active surface area of Pt-based nanophase electrocatalysts produced poor accuracy but an acceptable precision in the analytical data collected. JM Pt/C exhibited a satisfactory electrochemically active surface area whereas those of Pt/C (glycol), Pt/C (1-PrOH/H₂SO₄/pH2), Pt/C (1-PrOH/NaOH/pH12), and Pt/CNT were deemed poor. The technique may be limited by the site-blocking action of Nafion[®] molecules or the non-reproducibility of the cast-film electrodes. It is assumed that the JM Pt/C electrocatalyst possesses certain additional physico-chemical properties that enhance

its electrochemically active surface area, compared to the fabricated electrocatalysts. These properties may not have been distinguished by the characterization applied in this work and may not be observed in the fabricated electrocatalysts.

5.3. SUMMARY OF MAIN RESULTS

A testing protocol for the electrochemical characterization and screening of nanophase electrocatalysts was investigated. The following recommendations were made: (a) 0.5M H₂SO₄ should be used as the electrolyte solution to model the Nafion[®] membrane used in the DMFC and SPE-electrolyser. This is achievable since the pH of 0.5M H₂SO₄ solution is similar to the acid capacity/surface acidity of a Nafion[®] membrane; (b) the nanophase electrocatalyst should be suspended in 5% Nafion[®] solution to form an ink which should then be applied to the working electrode as a cast-film; (c) a 1:3 catalyst-to-Nafion[®] ratio should be used in the formulation of electrocatalyst inks; (d) 1M CH₃OH in 0.5M H₂SO₄ should be used as electrolyte solution for the electrochemical characterization of nanophase electrocatalysts in the MOR; (e) and O₂-saturated 0.5M H₂SO₄ should be used as the electrolyte solution for the electrochemical characterization of nanophase electrocatalysts in the ORR; (f) deaerated 0.5M H₂SO₄ should be used as electrolyte solution for characterization of electrocatalysts in the HER and 0.5M H₂SO₄ should be used for characterization of electrocatalysts in the OER. These recommendations should be used as guidelines for future electrochemical characterization studies of fabricated nanophase electrocatalysts.

Good correlation was not observed between SECM, PIXE, and SEM images with regard to the surface topography of electrocatalyst cast-films. Also, SECM and PIXE were unable to probe at the nanoscale in this investigation. It was difficult to extract quantitative chemical information from SECM images. Many further images were collected without improvement of the quantitation. For this reason the technique was limited to a qualitative role in the characterization of nanophase electrocatalysts.

SECM and PIXE would be better suited to the study of the surface elemental distribution of fuel cell electrodes and the chemical behaviour at the interface between the proton-conducting membrane and the catalyst layers.

Optimization of experimental variables in the impregnation-reduction preparation of carbon-supported Pt catalysts and electrochemical screening of these materials was investigated using CV of a $\text{Fe}^{2+}/\text{Fe}^{3+}$ redox couple. The following observations were made: (a) Pt/CNT and Pt/C(1-PrOH/ H_2SO_4 /pH2) exhibited catalytic activities larger or comparable to that of the JM Pt/C electrocatalyst; (b) nanophase Pt/C prepared using 1-propanol as solvent exhibit higher activities than that prepared using glycol as solvent; (c) catalytic activity is affected by pH where catalysts prepared from acidic solution exhibited notably higher catalytic activity compared to materials prepared from alkaline solution. On the basis of the observations the following recommendations were made: (a) Pt/CNT and Pt/C(1-PrOH/ H_2SO_4 /pH2) show potential as electrocatalysts (b) 1-propanol should be maintained as the solvent in the future preparation of Pt/C catalysts; and (c) fabricated Pt/C catalysts should be prepared from acidic solutions.

Optimization of the experimental variables in the preparation of HMS-templated carbon analogues was investigated using CV of a $\text{Fe}^{2+}/\text{Fe}^{3+}$ redox couple. The following observations were made: (a) Measured electrocatalytic activities of the carbon analogues were too erratic and random to observe a relationship pertaining to the influence of carbonization time on catalytic activity.; (b) slightly higher activities were observed upon carbonizing HMS after Pt deposition, compared to carbonising HMS before Pt deposition; (c) use of high surface area HMS to prepare carbon analogues led to higher activities compared to carbon analogues templated from low surface area HMS; (d) formaldehyde/methanol reduction produced enhancements in the catalytic activity of carbon analogues. On the basis of the findings it was recommended that carbon analogues be prepared by depositing Pt prior to

carbonization using high-surface area HMS templates and formaldehyde/methanol reduction.

The electrochemical characterization of Pt- and PtRu-based nanophase electrocatalysts in the MOR was conducted using CV in deaerated 1M CH₃OH supported by 0.5M H₂SO₄. The following observations were made: (a) higher catalytic activity was demonstrated by nanophase Pt/C, compared to that of bulk Pt; (b) higher activity was demonstrated upon the addition of Ru to the electrocatalyst composition; (c) a fabricated nanophase PtRu/C electrocatalyst exhibited significantly lower activity compared to that of the JM PtRu/C. This was a result of the incomplete alloying of Ru into the Pt lattice in the electrocatalyst preparation step and the larger PtRu particle size of the fabricated material; (d) mass transfer properties observed for the MOR on nanophase JM PtRu/C was significantly higher than that on smooth Pt. On the basis of the observations the following recommendations were made: (a) use of the nanophase JM PtRu/C should be maintained in the MOR; and (b) the methodology for the preparation of PtRu/C should be revised to ensure the complete alloying of Ru into the Pt lattice and smaller PtRu particle size.

The electrochemical characterization of Pt-based catalysts in the ORR was conducted using CV in O₂-saturated 0.5M H₂SO₄. The following observations were made: (a) large enhancements in activity and mass transfer properties were demonstrated upon decreasing the Pt particle size to the nanometre domain; (b) the JM Pt/C catalyst exhibited significantly higher activity and mass transfer properties compared to fabricated Pt catalysts; (c) a pH-influence on the activity was observed where catalysts prepared from acidic solution performed better than those prepared from alkaline solution; (d) higher activity was observed for catalysts prepared from 1-propanol compared to those prepared from 2-propanol indicative of a solvent influence on the catalytic activity of Pt-based catalysts (e) a particle size effect in the activity on Pt-based nanophase electrocatalysts was not observed. On the basis of the observations the following recommendations were made: (a) use of the JM Pt/C

catalyst in the ORR should be continued; and (b) fabricated Pt-based catalysts for the ORR should be prepared using 1-PrOH as solvent and in an acid buffered solution.

The electrochemical characterization of IrO₂ catalysts in the OER was investigated using CV in 0.5M H₂SO₄. The following observations were made: (a) IrO₂ underwent a reversible Ir³⁺/Ir⁴⁺ surface transition; and (b) the OER could not be characterized on fabricated IrO₂ due to difficulties associated with the disintegration of the cast-film layer by rapid bubble formation. Based on the observations, the electrochemical characterization of nanophase IrO₂, in the OER, should be re-evaluated with the preparation of new materials.

The electrochemical characterization of mesoporous silica-templated carbon analogues, carbon-supported Pt, and CNT-supported Pt nanophase electrocatalysts in the HER was investigated using LSV in deaerated 0.5M H₂SO₄. The following observations were made: (a) Pt/CNT exhibited higher activity compared to the JM Pt/C (b) good activities were exhibited by a range of materials which were comparable to that of the JM Pt/C. Based on the observations the following recommendations were made: (a) Pt/CNT should be tested as the cathode electrocatalyst in the membrane electrode assembly of a SPE-electrolyser; and (b) carbon analogues should be prepared by Pt deposition prior to carbonization of HMS templates.

The electrochemically-active surface area of Pt-based catalysts was determined using CV in 1M H₂SO₄. The following observations were made: (a) the technique produced poor accuracy and acceptable precision in the analytical data collected; (b) JM Pt/C exhibited a satisfactory electrochemically active surface area whereas those of Pt/C (glycol), Pt/C (1-PrOH/H₂SO₄/pH2), Pt/C (1-PrOH/NaOH/pH12), and Pt/CNT were deemed poor. These trends did not correlate well with the observed activities probed in Sections 5.2.2 and 5.2.6 (c) a particle size effect on the active surface area was not

observed. Based on the observations it was recommended that the technique be re-evaluated or revised.

The ability of cyclic voltammetry (CV) and linear-sweep voltammetry (LSV) to actively screen and discriminate between commercial and fabricated nanophase electrocatalysts, on the basis of their electrochemical properties, was demonstrated. In addition, CV and LSV were able to readily identify highly-electrocatalytic nanophase electrocatalysts, such as the newly-prepared Pt/CNT. CV and LSV were able to discriminate between various electrocatalysts on the basis of their electrocatalytic performance towards the $\text{Fe}^{2+}/\text{Fe}^{3+}$ redox couple in potassium ferrocyanide and the electrode reactions of the DMFC and SPE-electrolyser (i.e. MOR, ORR, OER, HER). It should be noted that CV and LSV suffered from poor precision and large multitudes of measurements were required to obtain comparable results. This shortcoming stems from the fact that electrocatalyst cast-film electrodes could not be perfectly reproduced in terms of surface structure or appearance. The accuracy of these techniques was demonstrated in their ability to identify Pt/CNT as possessing higher catalytic activity than the commercial JM Pt/C electrocatalyst in both potassium ferrocyanide and the hydrogen evolution reaction in deaerated 0.5M H_2SO_4 .

CHAPTER 6

CONCLUSIONS AND RECOMMENDATIONS

The overall objective of the study was the investigation of the applicability of various analytical tools for the qualitative and quantitative characterization of nanophase electrocatalysts. In addressing the overall objective the structural, thermal, and chemisorptive attributes of commercial nanophase JM Pt/C and JM PtRu/C electrocatalysts were evaluated. This was followed by an evaluation of the electrochemical activities of commercial and fabricated Pt/C, PtRu/C, IrO₂, mesoporous silica-templated carbon analogues, and Pt/CNT nanophase electrocatalysts.

A set of physico-chemical properties governing the catalytic abilities of nanophase electrocatalysts was identified in a comprehensive literature review. Experimental tasks were formulated to address the identified properties and a detailed research work-plan was designed to address these tasks. Characterization techniques were reviewed and used in investigating and evaluating the properties of nanophase electrocatalysts.

Good comparison was found, with reference to structural information of commercial nanophase JM Pt/C and JM PtRu/C (particle size; lattice parameters; surface area), between experimental data and specifications presented by the suppliers, Johnson Matthey™ and Cabot Corporation™. Also, good comparison was found between the experimental structural data in this study and the structural data determined by other investigators.

The high applicability of fundamental analytical techniques such as XRD and TEM in the structural characterization of nanophase electrocatalysts was demonstrated in this study. XRD and TEM allowed for the resolution of characteristics at the nanoscale

and were able to perform accurate analyses in the nanometre size domain. Quantitative information extracted using these characterization techniques were of high accuracy and precision and gave valuable insight into the parameters of interest of the electrocatalysts. These techniques should be used as the starting point of future nanophase electrocatalyst characterization studies. Metal particle sizes determined using XRD and TEM were in good agreement with literature values. Also, metal particle sizes determined using XRD were in good agreement with that determined using TEM. TEM exhibited high precision and accuracy as measured particle sizes were reproducible and agreed well with those determined in literature. TEM was also able to determine the primary carbon black support particle size, which was extremely difficult to quantify with other techniques considering the rapid aggregation of the material after manufacture. XRD was more reliable than TEM in determining the average metal nanoparticle size as TEM required tedious statistical sampling of a large number of particles for the average particle size to be considered representative of the material. However, the metal particle size distribution and qualitative metal dispersion could only be investigated using TEM. XRD could also qualitatively be used to monitor the degree of alloying in bimetallic nanophase electrocatalysts (i.e. PtRu/C).

SAED was successfully used for the rapid determination of the polycrystallinity and symmetry of the nanophase electrocatalysts utilised in this study. SAED was limited to a qualitative tool in the characterization of nanophase electrocatalysts as quantitative information was difficult to extract from SAED patterns.

In this study, metal nanoparticles could not be resolved from the carbon support materials using SEM and the technique was limited to the study of the agglomerate size distribution of the carbon support material. SEM was unable to resolve characteristics at the nanoscale and was therefore limited in its applications in the characterization study. SEM analysis demonstrated the high agglomeration of the “*as-received*” nanophase electrocatalysts when used in conjunction with HPPS data.

In future, SEM should be limited to the qualitative study of the agglomeration state of nanophase electrocatalysts and used in conjunction with HPPS aggregate size data.

In this study, HPPS was unable to probe into the nanoparticle domain (≤ 10 nm) of the metal electrocatalyst as it could not separate the size of the metal electrocatalyst from the size of the carbon support material. HPPS successfully allowed for the quantitative investigation of the average aggregate size and aggregate size distribution in supported catalysts. The aggregates were described as the smallest units of the supported nanophase electrocatalyst which could be separated. The JM Pt/C electrocatalyst was found to have an average aggregate size of 266 nm and an aggregate size distribution of 150-300 nm. This data was not readily available from the supplier. Particle sizing using HPPS was also determined to be optimal when using ethanol as the dispersant. By comparing SEM data to HPPS data the high agglomeration state of the “*as-received*” commercial electrocatalysts was qualitatively demonstrated. HPPS produced data of a high statistical precision illustrating the reliability of the technique for the aggregate size characterization of supported nanophase electrocatalysts used in this study. Knowledge of this parameter may indicate why the chemical behaviour of supported catalysts may differ.

N₂ physisorption produced total surface area and pore size distribution data which correlated well with that extracted from literature (high accuracy), but the technique was found to be limited, in this study, in that it was unable to determine surface areas specific to the active nanophase metal electrocatalyst, in carbon-supported materials. The measured average pore size did not correlate well to the BJH pore size distribution and isotherm plots. The average pore size was an unreliable measurement in this study and should be re-evaluated.

Techniques which were fairly novel in a nanophase electrocatalyst characterization context, such as SECM and PIXE, were applied in the investigation of the surface topography of electrocatalyst cast-films. The resolution of these techniques did not

allow for an investigation of material characteristics at the nanoscale. It was very difficult to extract quantitative chemical information from SECM maps and for this reason the technique was limited to a qualitative role in the characterization of nanophase electrocatalysts and was not a reliable measure of comparative activity. PIXE allowed for the discrimination of uniform elemental dispersion across the surface of electrocatalyst cast-films, but would be better utilised in the study of the surface elemental distribution on fuel cell electrodes than on electrocatalyst cast-films. This type of information may help in the understanding of the chemical behaviour at the interface between the proton-conducting membrane and the catalyst layers.

TGA was used both qualitatively and quantitatively in the investigation of the thermal stabilities of supported nanophase electrocatalysts. The results obtained in the thermal characterization of nanophase electrocatalysts were not significant, in the context of nanophase electrocatalysts in fuel cell operation, as the DMFC and SPE-electrolyser are operated between 60-120 °C, and not at high temperature. In future, TGA should be used in the determination of the volatile content of nanophase electrocatalysts.

In this study, TPR was concluded to be both a qualitative and semi-quantitative analytical tool in the characterization of nanophase electrocatalysts and could be more widely applied for comparative purposes. Observations made in the TPR analysis were in good agreement with those in literature. TPR successfully speciated the surface chemical state and was able to qualitatively investigate the strength of the metal-support interaction.

CV and LSV were well suited to the electrochemical characterization of nanophase electrocatalysts in this study due to the ability to readily identify highly-active materials, such as the newly-developed Pt/CNT. These techniques were successfully employed in a comparative electrochemical screening of the catalytic activities of commercial and fabricated nanophase catalysts in this study. LSV was able to

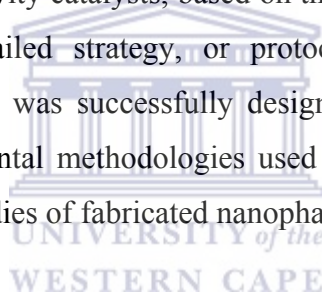
discriminate between various electrocatalysts on the basis of their electrocatalytic performance towards the $\text{Fe}^{2+}/\text{Fe}^{3+}$ redox couple in potassium ferrocyanide and the electrode reactions of the DMFC and SPE-electrolyser. Using these electrochemical techniques, certain materials were successfully identified as potential cost-effective, high activity replacements for the currently-used Johnson Matthey™ Pt/C catalyst. Also, preparation variables could be critically evaluated and optimized for future fabrication of cost-effective highly-active nanophase electrocatalysts. It should be noted that CV and LSV suffered from poor precision and large multitudes of measurements were required to obtain comparable results. This shortcoming stems from the fact that electrocatalyst cast-film electrodes could not be perfectly reproduced in terms of surface structure or appearance. The accuracy of CV and LSV was demonstrated in their ability to identify Pt/CNT as possessing higher catalytic activity than the commercial JM Pt/C electrocatalyst in both potassium ferrocyanide and the hydrogen evolution reaction in deaerated 0.5M H_2SO_4 .

On the basis of its high catalytic activity, a carbon nanotube-supported nanophase Pt catalyst (Pt/CNT) is envisaged as a cost-effective replacement for the currently-used Johnson Matthey™ Pt/C catalyst. It is recommended that Pt/CNT be tested in the membrane electrode assembly of the direct methanol fuel cell or the solid-polymer electrolyte electrolyser.

The electrochemical characterization of the fabricated PtRu/C catalyst highlighted its inefficiency as a methanol oxidation catalyst. It is recommended that the methodology for the preparation of nanophase PtRu/C be revised to ensure the adequate alloying of Ru into the Pt lattice and large reduction in the particle size. For this reason, the Johnson Matthey™ PtRu/C catalyst should be retained in the methanol oxidation reaction, in the DMFC, until more efficient nanophase PtRu/C electrocatalysts are fabricated.

It is recommended that PtRu nanophase electrocatalysts, for the methanol oxidation reaction, be supported on carbon nanotubes instead of Vulcan XC-72[®]. Supporting on carbon nanotubes produced high-activity nanophase Pt electrocatalysts, and supporting nanophase PtRu on carbon nanotubes should also produce high-activity supported materials.

In closing, the applicability of characterization techniques for the quantitative and qualitative characterization of nanophase electrocatalysts was investigated. Techniques such as XRD, TEM, HPPS, TPR, N₂-physisorption, CV, and LSV were used in this study and confirmed to be highly applicable and advantageous in the qualitative and quantitative characterization of the physico-chemical properties of nanophase electrocatalysts. These techniques were also competent in discriminating between high and low activity catalysts, based on the structural-chemical relationship of nanomaterials. A detailed strategy, or protocol, for the characterization of nanophase electrocatalysts was successfully designed. It is recommended that this strategy and the experimental methodologies used in this study be implemented in future characterization studies of fabricated nanophase electrocatalysts.



REFERENCES

- [1] Ebbing. D.D. (1993) *General Chemistry*, 4th Edition, Boston, Houghton Mifflin Company, **14**: 461-466, 606-609, 648-650.
- [2] Thomsett. D. (2003) Catalysts for the Proton Exchange Membrane Fuel Cell, *Fuel Cell Technology Handbook*, Florida, CRC Press LLC, **6**: 1-23.
- [3] Marković. N.M, Radmilovic. V, Ross. Jr, P.N. (2003) Physical and Electrochemical Characterization of Bimetallic Nanoparticle Electrocatalysts, *Catalysis and Electrocatalysis at Nanoparticle Surfaces*, New York, Marcel Dekker Inc. **9**: 311-342.
- [4] Holister. P, Román. C, Harper. T. (2003) *Nanotechnology Opportunity Report*, 2nd Edition, **1**: 61-290.
- [5] Koper. M.T.M, Van Santen. R.A, Neurock. M. (2003) Theory and Modelling of Catalytic and Electrocatalytic Reactions, *Catalysis and Electrocatalysis at Nanoparticle Surfaces*, New York, Marcel Dekker Inc. **1**: 1-34.
- [6] Schoeman. B.J, Higberg. K, Sterte. J. (1999) *Nanostructured Materials*, **12**: 49-54.
- [7] Fitz-Gerald. J, Pennycook. S, Gao. H, Singh. R.K. (1999) *Nanostructured Materials*, **12**: 1167-1171.
- [8] Shi. Z, Liu. M. (2000) Electrical and Electrochemical Analysis of Nanophase Materials, *Characterization of Nanophase Materials*, Weinheim, Wiley-VCH Verlag GmbH, **6**: 165, 166, 171, 177.
- [9] Sheka. E.F, Khavryutchenko. V.D. (1995) *Nanostructured Materials*, **6**: 803-806.
- [10] Electronic references (2003) *Nanomaterials tutorial*, Sigma–Aldrich, [ONLINE]. Available: <http://www.sigmaaldrich.com/suite7>.
- [11] Hahn. H, Padmanabhan. K.A. (1995) *Nanostructured Materials*, **6**: 191-200.
- [12] Walsh. F.C. (2001) *Pure and Applied Chemistry*, **73**: 1820.

References

- [13] Antonucci. V, Arico. A.S, Antonucci. P.L. (2003) Metal-Support Interaction in Low-Temperature Fuel Cell Electrocatalysts, *Catalysis and Electrocatalysis at Nanoparticles Surfaces*, New York, Marcel Dekker Inc. **17**: 613-643.
- [14] Zhdanov. V.P, Kasemo. B. (2003) Simulations of Reaction Kinetics on Nanometre-sized Supported Catalyst Particles, *Catalysis and Electrocatalysis at Nanoparticle Surfaces*, New York, Marcel Dekker Inc. **2**: 35-64.
- [15] Lamy. C, Léger. J.-M. (2003) Electrocatalysis with Electron-Conducting Polymers Modified by Noble Metal Nanoparticles, *Catalysis and Electrocatalysis at Nanoparticle Surfaces*, New York, Marcel Dekker Inc. **25**: 907-929.
- [16] Warren. P.J, Larson. D.J, Weston. C, Cerezo. A, Petford-Long. A.K, Smith. G.D.W, Cantor. B. (1999) *Nanostructured Materials*, **12**: 697-700.
- [17] Jordan. L.R, Shukla. A.K, Behrsing. J, Avery. N.R, Muddle. B.C, Forsyth. M. (2000) *Journal of Applied Electrochemistry*, **30**: 641.
- [18] Easton. E.B. (2003) *Chemical Modification of Fuel Cell Catalysts and Electrochemistry of Proton Exchange Membrane Fuel Cell Electrodes*, PhD Thesis, Newfoundland, Canada: Memorial University of Newfoundland.
- [19] Li. W, Zhou. W, Li. H, Zhou. Z, Zhou. B, Sun. G, Xin. Q. (2004) *Electrochimica Acta*, **49**: 1045-1055.
- [20] Cabot™ Corporation [ONLINE] Available: <http://w1.cabot-corp.com/index.jsp>.
- [21] Vielstich. W, Lamm. A, Gasteiger. H. A. (2003) Part 4: Fuel cell principles, systems and applications, *Handbook of Fuel Cells: Fundamentals, Technology, and Applications*, West Sussex, John Wiley and Sons Ltd. **1**: 42.
- [22] Simonov. P.A, Likholobov. V.A. (2003) Physicochemical Aspects of Preparation of Carbon-Supported Noble Metal Catalysts, *Catalysis and Electrocatalysis at Nanoparticle Surfaces*, New York, Marcel Dekker Inc., **12**: 409-454.
- [23] Hayden. B.E. (2003) Single-Crystal Surfaces as Model Platinum-Based Hydrogen Fuel Cell Electrocatalysts, *Catalysis and Electrocatalysis at Nanoparticle Surfaces*, New York, Marcel Dekker Inc. **1**: 1-34.
- [24] Maillard. F, Martin. M, Gloaguen. F, Léger, J-M. (2002) *Electrochimica Acta*, **47**: 3431-3440.
-

References

- [25] Prabhuram. J; Zhao. T.S; Wong. C.W; Guo. J.W; (2004) *Journal of Power Sources*, **134**(1): 1-6.
- [26] Johnson Matthey™ HiSPEC® Catalyst Datasheet. [ONLINE] Available: http://www.johnsonmattheyfuelcells.com/HiSPEC_Datasheet.pdf.
- [27] Cherstiouk. O.V, Simonov. P.A, Savinova. E.R. (2003) *Electrochimica Acta*, **48**: 3851-3860.
- [28] Gojković. S.Lj, Vidaković. T.R. (2001) *Electrochimica Acta*, **47**: 633-642.
- [29] Zhou. W. (2003) *Research on Anode Catalysts for Low Temperature Direct Alcohol Fuel Cells*, Dalian Institute of Chemical Physics.
- [30] Qin. X, Zhou. W, Zhou. Z. (2001) Chinese patent 011 389,9,5.
- [31] Paulus. U.A. (2002) *Electrocatalysis for Polymer Electrolyte Fuel Cells: Metal Alloys and Model Systems*, PhD Thesis, Zurich: Swiss Federal Institute of Technology.
- [32] Radmilovic. V, Gasteiger. H.A, Ross. P.N, (1995), *Journal of Catalysis*, **154**: 98-106.
- [33] The Center for Nanotechnology at the University of Washington. (2005) *Fabrication and Characterization of Nanomaterials*. Washington. [ONLINE]. Available: https://www.engr.washington.edu/epp/nano/jan_04.html.
- [34] Zhang. J. (2004) *Investigation of CO Tolerance in Proton Exchange Membrane Fuel Cells*, PhD Thesis, Worcester, England: Worcester Polytechnic Institute.
- [35] Oberdöster. G, Maynard. A, Donaldson. K. (2005) *Particle and Fibre Toxicology*, **2**:8.
- [36] Haber. J (1991) *Pure and Applied Chemistry*, **63** (9): 1227-1246.
- [37] International Union of Pure and Applied Chemistry (1997) *IUPAC Compendium of Chemical Terminology*. [ONLINE] Available: <http://www.iupac.org/goldbook/C01433.pdf>.
- [38] Allen. E, Henshaw. J, Smith. P. (2001) *A Review of Particle Agglomeration*, [ONLINE], Available at: <http://www.tanks.org/ttgdoc/AEAT-R-PSEG-0398.doc>.

-
- [39] Han. O.H, Han K.S, Babu. P.K., *Pt Particle Size Effect and Metal-Support Interaction Observed by ^{13}C NMR*, [ONLINE], Available at http://ecssat.peerx-press.org/ms_files/ecssat.pdf.
- [40] Steigerwalt. E.S, Deluga. G.A, Cliffel. D.E. Lukehart. C.M. (2001) *Journal of Physical Chemistry*, **105**: 8097-8101.
- [41] Cattaneo. C, Sanchez de Pinto. M.I, Mishima. H, Lòpez de Mishima. B.A, Lescano. D, Cornaglia. L. (1999) *Journal of Electroanalytical Chemistry*, **461**: 32-39.
- [42] Iwasita. T. (2003) Methanol and CO electro-reduction, *Handbook of Fuel Cells – Fundamentals, Technology, and Applications, Volume 2: Electrocatalysis*, Vielstich. W, Gasteiger. H.A, Lamm. A. (Editors), Chichester, England, John Wiley and Sons, **41**: 603-625.
- [43] Iwasita. T. (2002) *Electrochimica Acta*, **47**: 3663-3674.
- [44] Gojković. S.Lj, Vidaković. T.R, Durović. D.R. (2003) *Electrochimica Acta*, **48**: 3607-3614.
- [45] Jiang. J, Kucernak. A. (2002) *Journal of Electroanalytical Chemistry*, **533**: 153-165.
- [46] Nieto. F, Ramirez Cuesta. A, Velasco. A, Riccardo. J.L, Zgrablich. G. (1993) *Journal of Physics: Condensed Matter*, **5**: A235-236.
- [47] Gattrell. M, MacDougall. B. (2003) Reaction Mechanisms of the O₂ Reduction/Evolution Reaction. Vielstich.W, Lamm. A, Gasteiger. H.A (ed.), *Handbook of Fuel Cells: Fundamentals, Technology, and Applications*. Chichester: John Wiley and Sons, **2**: 453.
- [48] Mukerjee. S. (2003) In-Situ X-ray Absorption Spectroscopy of Carbon-Supported Pt and Pt-Alloy Electrocatalysts: Correlation of Electrocatalytic Activity with Particle Size and Alloying, *Catalysis and Electrocatalysis at Nanoparticle Surfaces*, New York, Marcel Dekker Inc. **14**: 501-530.
- [49] Nagai. N, Takeuchi. M, Kimura. T, Oka. T. (2003) *International Journal of Hydrogen Energy*, **28**: 35-41.
- [50] Matsushima. H, Nishida. T, Konishi. Y, Fukunaka. Y, Ito. Y, Kuribayashi. K. (2003) *Electrochimica Acta*, **48**: 4119-4125.
- [51] Yang. Y-F, Denault. G. (1998) *Journal of Electroanalytical Chemistry*, **443**: 273-282.
-

References

- [52] Rasten. E, Hagen. G, Tunold. R. (2003) *Electrochimica Acta*, **48**: 3945-3952.
- [53] Thamahane. T.C. (2005) *Development of Anodic Electrocatalysts and Optimization of Membrane Electrode Assemblies for Hydrogen Production in Water Electrolysis*, Unpublished MSc Thesis. Department of Chemistry, University of the Western Cape.
- [54] Barber. J.H, Conway. B.E. (1999) *Journal of Electroanalytical Chemistry*, **461**: 80-89.
- [55] Tavares. M.C, Machado. S.A.S, Mazo. L.H. (2001) *Electrochimica Acta*, **46**: 43594369.
- [56] Hu. W. (2000) *International Journal of Hydrogen Energy*, **25**: 111-118.
- [57] Ying. Q. (2005), *Preparation and Characterization of Highly Active Nano Pt/C Electrocatalyst*. Unpublished MSc Thesis. Department of Chemistry, University of the Western Cape.
- [58] Wang. X. (2005), *Pt-Ru/C Catalyst Preparation for DMFC Application*. Unpublished MSc Thesis. Department of Chemistry, University of the Western Cape.
- [59] Godongwana. Z.G. (2005), *Homogeneity and Reproducibility of Nanophase Electrocatalysts Supported on Mesoporous Materials*. Unpublished MSc Thesis. Department of Chemistry, University of the Western Cape.
- [60] Pinault. M, Mayne-L'Hermite. M, Reynaud. C, Pichot. V, Launois. P, Ballutaud. D. (2005) *Carbon*, **43**: 2968-2976.
- [61] Rhoda. R.N, Vines. R.F. (1969) U.S. patent 3,486,928.
- [62] Zhang. W, Pauly. T.R, Pinnavaia. (1997) *Chem. Mater*, **9**: 2491.
- [63] Jenkins. R, de Vries. J.L, *An Introduction to X-Ray Powder Diffractometry*, Eindhoven, N.V. Phillips Gloeilampenfabrieken, **2**: 8-10.
- [64] Perego. G. (1998) *Catalysis Today*, **41**: 251-259.
- [65] Lipson. H, Steeple.H.(1970) *Interpretation of X-ray Powder Diffraction Patterns*, London, Macmillan and Company Ltd. **4**: 93-94, **5**: 113-114.
- [66] Cullity. B.D. (1978) *Elements of X-ray Diffraction*, 2nd Edition, Ontario, Addison-Wesley Publishing Company Inc. **7**: 188-226.

References

- [67] Van Helleputte. H.R.J.R, Haddeman. T.B.J, Verheijen. M.J, Baalbergen. J.-J. (1995) *Microelectronic Engineering*, **27**: 547-550.
- [68] Müller. T.E, Reid. D.G, Hsu. W.K, Hare. J.P, Kroto. H.W, Walton. D.R.M. (1997) *Carbon*, **35**: 495-502.
- [69] Goldstein. J.I, Newbury. D.E, Echlin. P, Joy. D.C, Fiori. C, Lifshin. E. (1981) *Scanning Electron Microscopy and X-ray Microanalysis: A Text for Biologists, Materials Scientists, and Geologists*, New York, Plenum Press, **1**: 1-3, **6**: 275-278.
- [70] Oatley. C.W. (1972) *The Scanning Electron Microscope, Part 1: the Instrument*, London, Cambridge University Press, **1**: 1-2.
- [71] Newbury. D.E, Joy. D.C, Echlin. P, Fiori. C.E, Goldstein. J.I (1986) *Advanced Scanning Electron Microscopy and X-ray Microanalysis*, New York, Plenum Press, **5**: 186, **7**: 295.
- [72] Fultz. B, Howe. J.M. (2002) *Transmission Electron Microscopy and Diffractometry of Materials*, 2nd Edition, Berlin, Springer-Verlag, **2**: 63, **4**: 203-213, **7**: 339.
- [73] Tsang. S.C, de Oliveira. P, Davis. J.J, Green. M.L.H, Hill. H.A.O. (1996) *Chemical Physics Letters*, **249**: 413-422.
- [74] Treacy. M.M.J. (1986) Detection and Imaging of Supported Catalyst Particles, *Materials Problem Solving with the Transmission Electron Microscope*, Hobbs. L.W, Westmacott. K.H, Williams. D.B. (editors), Pittsburgh, Materials Research Society, **62**: 367-378.
- [75] Ganesan. P, Kuo. H.K, Saavedra. A, De Angelis. R.J. (1978) *Journal of Catalysis*, **52**: 310-320.
- [76] Hornyak. G.L, Peschel. S.T, Sawitowski. T.H, Schmid. G. (1998) *Micron*, **29**: 183-190.
- [77] Sklad. P.S. (1988) The Preparation of TEM Specimens form Hazardous or Difficult Materials, *Specimen Preparation for Transmission Electron Microscopy of Materials*, Bravman. J.C, Anderson. R.M, McDonald. M.L. (editors), Pittsburgh, Materials Research Society, **115**: 39-50.

-
- [78] Rice. S.B, Treacy. M.J. (1988) The Art of the Possible: An Overview of Catalyst Specimen Preparation Techniques for TEM Studies, Bravman. J.C, Anderson. R.M, McDonald. M.L. (ed.), *Specimen Preparation for Transmission Electron Microscopy of Materials*, Pittsburgh, Materials Research Society, **115**: 15-27.
- [79] Han. K, Yu-Zhang. K. (2004) *Scripta Materialia*, **50**: 781-786.
- [80] Chao. K.J, Wu. C.N, Chang. A.S, Hu. S.F. (1999) *Microporous and Mesoporous Materials*, **27**: 287-295.
- [81] Ross. S, Olivier. J.P. (1964) *On Physical Adsorption*, New York, John Wiley and Sons Inc., **2**: 12, 29, 66-69, 75-76.
- [82] Wedler. G. (1976) *Chemisorption: An Experimental Approach*, London, Chapel River Press, **3**: 29-31.
- [83] Webb. P.A, Orr. C, Camp. R.W, Olivier. J.P, Yunes. Y.S. (1997) *Analytical Methods in Fine Particle Technology*, Georgia, Micromeritics Instrument Corporation, **1**: 11-14, **6**: 219-268.
- [84] Takasu. Y, Kawaguchi. T, Sugimoto. W, Murakami. Y. (2003) *Electrochimica Acta*, **48**: 3861-3868.
- [85] Long. J.W, Ayers. K.E, Rolison. D.R. (2002) *Journal of Electroanalytical Chemistry*, **522**: 58-65.
- [86] Atkins. P.W. (1979) *Physical Chemistry*, London, Oxford University Press, **28**: 942.
- [87] Fukatsugawa. S, Hatakeyama. S, Saitou. Y, Sera. K. (1996) *Nuclear Instruments and Methods in Physics Research B: Beam Interactions with Materials and Atoms*, **109/110**: 113-120.
- [88] Imaseki. H, Yukawa. M, Watt. F, Ishikawa. T, Iso. H, Hamano. T, Matsumoto. K, Yasuda. N. (2003) *Nuclear Instruments and Methods in Physics Research B: Beam Interactions with Materials and Atoms*, **210**: 42-47.
- [89] Johansson. S.A.E, Campbell. J.L, Malmqvist. K.G. (1995) *Particle-Induced X-ray Emission Spectroscopy (PIXE)*, Wiley, New York, 451.
- [90] Ryan. C.G, Jamieson. D.N, Churms. C.L, Pilcher. J.V. (1995) *Nuclear Instruments and Methods in Physics Research B: Beam Interactions with Materials and Atoms*, **104**: 157-165.
-

References

- [91] Wendlandt. W.W.M. (1964) *Thermal Methods of Analysis*, New York, Interscience Publishers, **2**: 4-43.
- [92] Newkirk. A.E. (1960), *Analytical Chemistry*, **32**: 1558-1563.
- [93] Pan. D, Jaroniec. M, Klinik. J. (1996) *Carbon*, **34**: 1109-1113.
- [94] Jaroniec. M, Gilpin. R.K, Ramler. J, Choma. J. (1996) *Thermochimica Acta*, **272**: 65-73.
- [95] Brown. M.E. (1988) *Introduction to Thermal Analysis: Techniques and Applications*, New York, Chapman and Hall Ltd. **2**: 5, **3**: 7-21.
- [96] Skoog. D.A, West. D.M, Holler. F.J. (1996) *Fundamentals of Analytical Chemistry, 7th Edition*, Florida, Saunders College Publishing, **29**: 690-691.
- [97] Cioci. F, Lavecchia. R, Fierro. G, Jacono. M.L, Inversi. M. (1996) *Thermochimica Acta*, **287**: 351-362.
- [98] Rachmady. W, Vannice. M.A. (2002) *Journal of Catalysis*, **207**: 317-330.
- [99] Reiche. M.A, Maciejewski. M, Baiker. A. (2000) *Catalysis Today*, **56**: 347-355.
- [100] Kenvin. J (2004) *Gas Adsorption and Characterization of Powders and Porous Materials*, Presentation delivered at the Department of Chemical Engineering, University of Cape Town.
- [101] Jarvi. T.D, Stuve. E.M. (1998) Fundamental Aspects of Vacuum and Electrocatalytic Reactions of Methanol and Formic Acid on Platinum Surfaces, *Electrocatalysis*, Lipkowski. J, Ross Jr. P.N. (editors), New York, Wiley-VCH Inc. **3**: 75-153.
- [102] Nart. F.C, Vielstich. W. (2003) Normalization of Porous Active Surfaces. Vielstich.W, Lamm. A, Gasteiger. H.A (ed.), *Handbook of Fuel Cells: Fundamentals, Technology, and Applications*. Chichester: John Wiley and Sons, **2**: 306-307.
- [103] Bard. A.J, Faulkner. L.R. (2001) *Electrochemical Methods: Fundamentals and Applications, 2nd Edition*, New York: John Wiley and Sons, **4**: 137.
- [104] International Union of Pure and Applied Chemistry (1997) *IUPAC Compendium of Chemical Terminology*. [ONLINE] Available: <http://www.iupac.org/goldbook/D01719.pdf>.

References

- [105] Katz.E. (2005) *Biosensors and Bioelectronics Home Page of Eugenii Katz*. [ONLINE] Available: http://chem.ch.huji.ac.il/~eugeniik/randles_sevcik_equation.htm.
- [106] International Union of Pure and Applied Chemistry (1997) *IUPAC Compendium of Chemical Terminology*. [ONLINE] Available: <http://www.iupac.org/goldbook/C01240.pdf>.
- [107] Liu. Z, Ling. X.Y, Su. X, Lee. J.Y, Gan. L.M. (2005) *Journal of Power Sources*, **149**: 1-7.
- [108] Jambunathan. K, Shah. B.C, Hudson. J.L, Hillier. A.C. (2001) *Journal of Electroanalytical Chemistry*, **500**: 279-289.
- [109] Zhou. J, Zu. Y, Bard. A.J. (2000) *Journal of Electroanalytical Chemistry*, **491**: 22-29.
- [110] Kucernak. A.R, Chowdury. P.B, Wilde. C.P, Kelsall. G.H, Zhu. Y.Y, Williams. D.E. (2000) *Electrochimica Acta*, **45**: 4483-4491.
- [111] Barker. A.L, Unwin. P.R, Gardner. J.W, Rieley. H. (2004) *Electrochemistry Communications*, **6**: 91-97.
- [112] Kallio. T, Slevin. C, Sundholm. G, Holmlund. P, Kontturi. K. (2003) *Electrochemistry Communications*, **5**: 561-565.
- [113] Jambunathan. K, Hillier. A.C. (2002) *Journal of Electroanalytical Chemistry*, **524-525**: 144-156.
- [114] Rayendran. L, Ananthi. S.P. (2004) *Journal of Electroanalytical Chemistry*, **561**: 113-118.
- [115] Wipf. D.O. (1998) *Scanning Electrochemical Microscopy* [ONLINE], Available: <http://www.msstate.edu/dept/Chemistry/dow1/secm/secm.html>
- [116] Barker. A.L, Gonsalves. M, Macpherson. J.V, Slevin. C.J, Unwin. P.R. (1999) *Analytica Chimica Acta*, **385**: 223 – 240.
- [117] Nann. T, Heinze. J. (2003) *Electrochimica Acta*, **48**: 3975-3980.
- [118] Etienne. M, Schulte. A, Schuhmann. W. (2003) *Electrochemistry Communications*, **6**: 288-293.

References

- [119] Xiong. H, Guo. J, Kurihara. K, Amemiya. S. (2004) *Electrochemistry Communications*, **6**: 615-620.
- [120] Borgwarth. K, Ebling. D, Heinze. J. (1995) *Electrochimica Acta*, **40**: 1455-1460.
- [121] Mallouk. T.E, Smotkin. E.S. (2003) Combinatorial Catalyst Development Methods. Vielstich.W, Lamm. A, Gasteiger. H.A (ed.), *Handbook of Fuel Cells: Fundamentals, Technology, and Applications*. Chichester: John Wiley and Sons, **2**: 340.
- [122] Wong. C.W, Guo. J.W, Prabhuram. J, Zhao. T.S (2005) *Electrochimica Acta*, **50**: 1973-1983.
- [123] Dale Minerals International, *X-ray Spacing*, [ONLINE], Available: <http://www.webmineral.com/X-Ray/shtml>.
- [124] Kwon. O-K, Kwon. S-H, Park. H-S, Kang. S.W. (2004) *Electrochemical and Solid-State Letters*, **7**(4): C46-C48.
- [125] Tsou. Y-M, Cao. L, De Castro. E, *Characteristics of High Performance PtRu Methanol Catalysts and Mechanistic Understanding*, E-TEK division, De Nora North America, Inc.
- [126] Guo. J.W, Zhao. T.S, Prabhuram. J, Chen. R, Wong. C.W (2005) *Electrochimica Acta*, **51**: 754-763.
- [127] Tripković. A.V, Popović. K.D, Grgur. B.N, Blizanac. B, Ross. P.N, Marković. N.M (2002) *Electrochimica Acta* **47**: 3707-3714.
- [128] International Union of Pure and Applied Chemistry (1997) *IUPAC Compendium of Chemical Terminology*. [ONLINE] Available: <http://www.iupac.org/goldbook/M03672.pdf>.
- [129] Stevens. D.A. and Dahn J.R., *Abs. 1022, 204th Meeting, 2003 The Electrochemical Society, Inc.*
- [130] Yang. B, Lu. Q, Wang. L, Zhuang. L, Lu. J, Liu. P, (2003) *Chemical Materials*, **15**: 3552.
- [131] Long. J.W, Stroud. R.M, Swider-Lyons. K.E, Rolison. D.R. (2000) *Journal of Physical Chemistry B*, **104**: 9772.

References

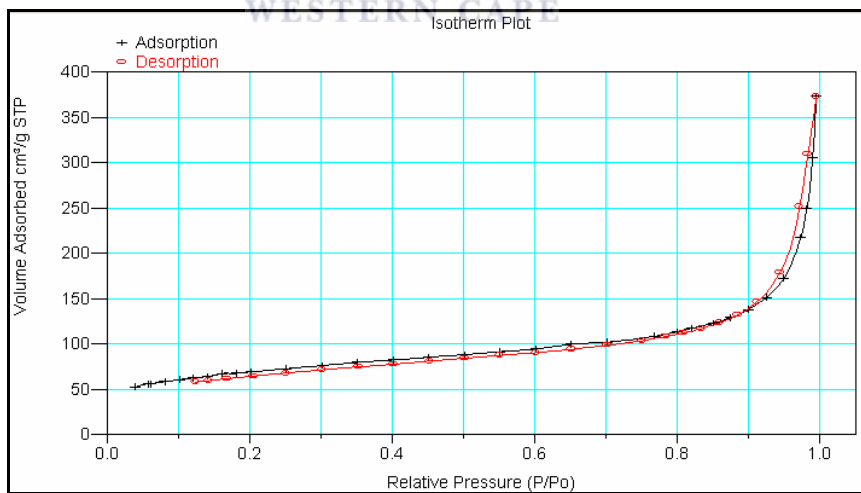
- [132] Gojkovic. S.L, Zecevic. S.K, Savinell. R.F. (1998) *Journal of the Electrochemical Society*, **145**: 3713.
- [133] Schmidt. T.J, Gasteiger. H.A, Stab. G.D, Urban. P.M, Kolb. D.M, Behm. R.J. (1998) *Journal of the Electrochemical Society*, **145**: 2354.
- [134] Choi. L-Y, Zhaolin. L, *Study of the Factors Influencing Catalytic Activity in MOR*, 1-8.
- [135] Cruickshank. J, Scott. K. (1998) *Journal Of Power Sources*, **70**: 40-47.
- [136] Antoine. O, Bultel. Y, Durand. R. (2001) *Journal of Electroanalytical Chemistry*, **499**: 85-94.
- [137] Nugent. J.M, Santhanam. K.S.V, Rubio. A, Ajayan. P.M. (2001) *Nanoletters*, **1**(2): 87-91.
- [138] Casella. I.G, Desimoni. E, (1996) *Electroanalysis*, **8**: 447-453.
- [139] Swider-Lyons. K, Stanley. J, Ugarte. N, Cotton. G, Dmowski. W, Egami. T (2002) *Low-Platinum and Platinum-Free Catalysts for Oxygen Reduction at Fuel Cell Cathodes*. [ONLINE] Available: <http://www.eere.energy.gov/hydrogenandfuelcells/pdfs/nn0123q.pdf>.
- [140] Komanicky. V, Menzel A, You. H. (2005) *Journal of Physical Chemistry B*, **109**: Article in press, Available: <http://pubs.acs.org/cgi-bin/asap.cgi/jpcb/k/asap/pdf/jp054155a.pdf>.
- [141] Da Silva. L.A, Alves. V.A, Da Silva. M.A.P, Trasatti. S, Boodts. J.F.C. (1996) *Electrochimica Acta*, **42**: 271-281.
- [142] Shan. J, Pickup. P.G. (2000) *Electrochimica Acta*, **46**: 119-125.
- [143] Stonehart. P, (1992), *Journal of Applied Electrochemistry*, **22**: 995.
- [144] Marković. N.M, Gasteiger. H.A, Grgur B.N, Ross. P.N. (1999) *Journal of Electroanalytical Chemistry*, **467**: 157-163.

APPENDICES

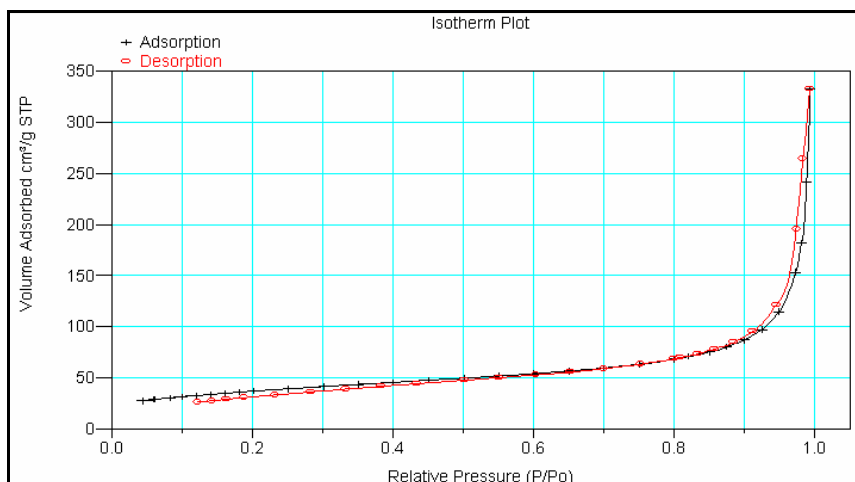
APPENDIX A: Vulcan[®] XC-72 aggregate size data collected using ethanol as the sample dispersant

Sample Identification	Analysis number and particle size (nm)					Mean particle size (nm)
	1 (nm)	2 (nm)	3 (nm)	4 (nm)	5 (nm)	
A	364.4	366.0	367.2	363.9	363.9	365.1
B	366.0	366.1	363.5	367.4	368.2	366.2
C	365.1	362.1	361.9	365.9	367.4	364.5
D	369.6	367.3	364.4	365.5	367.8	366.9
E	364.1	365.8	363.8	367.4	365.9	365.4
F	365.4	366.6	366.6	364.0	364.2	365.4
G	370.7	362.9	368.1	365.7	364.6	366.4

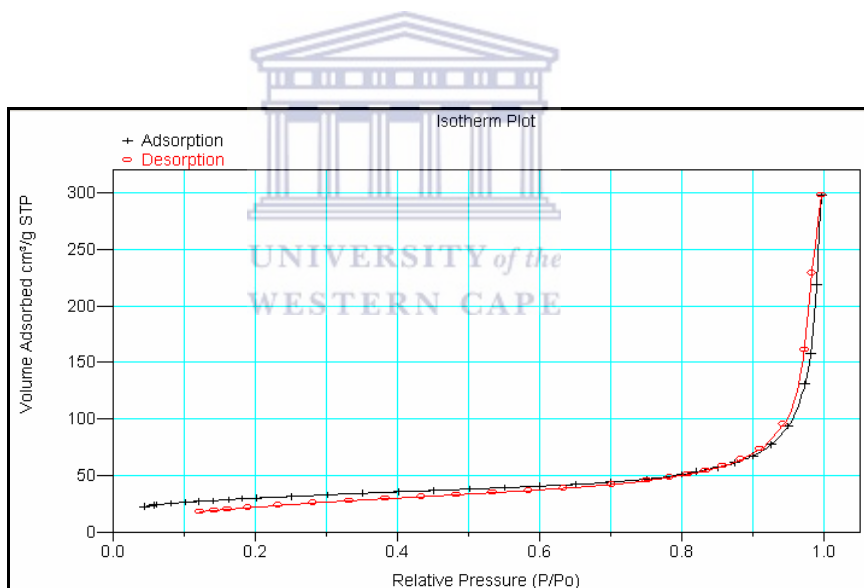
Population mean = 365.7 nm
Population deviation = 0.83 nm



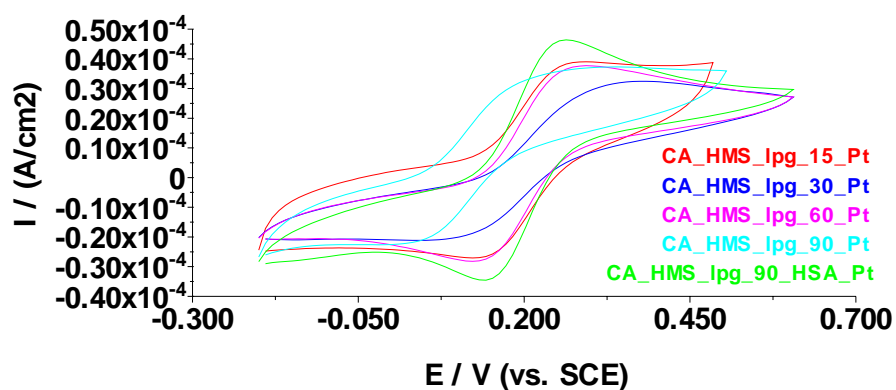
APPENDIX B1: Adsorption isotherm for the total surface area and porosity determination of Vulcan[®] XC-72 using BET N₂-physisorption



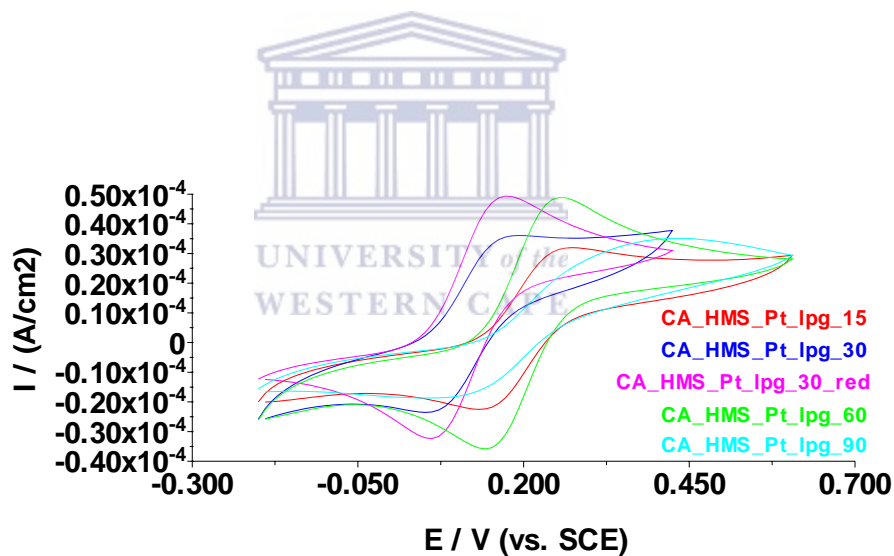
APPENDIX B2: Adsorption isotherm for the total surface area and porosity determination of a nanophase Johnson Matthey™ Pt/C electrocatalyst using BET N₂-physorption



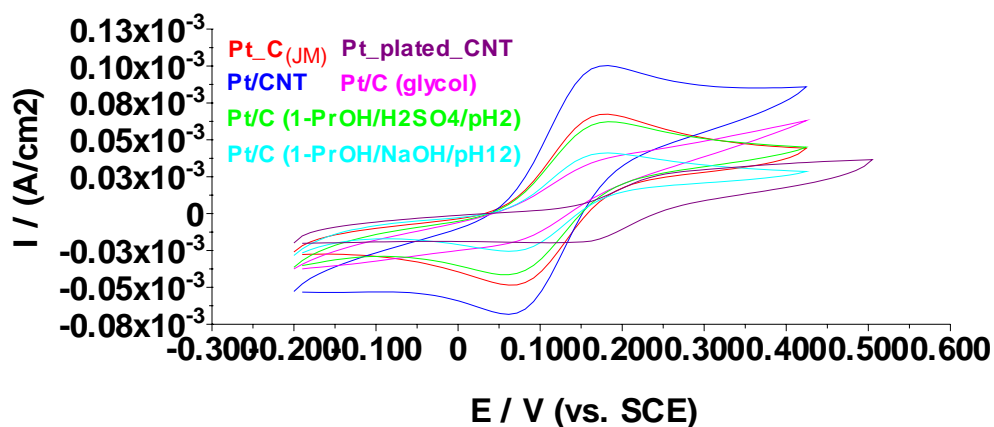
APPENDIX B3: Adsorption isotherm for the total surface area and porosity determination of a Johnson Matthey™ PtRu/C nanophase electrocatalyst using BET N₂-physorption



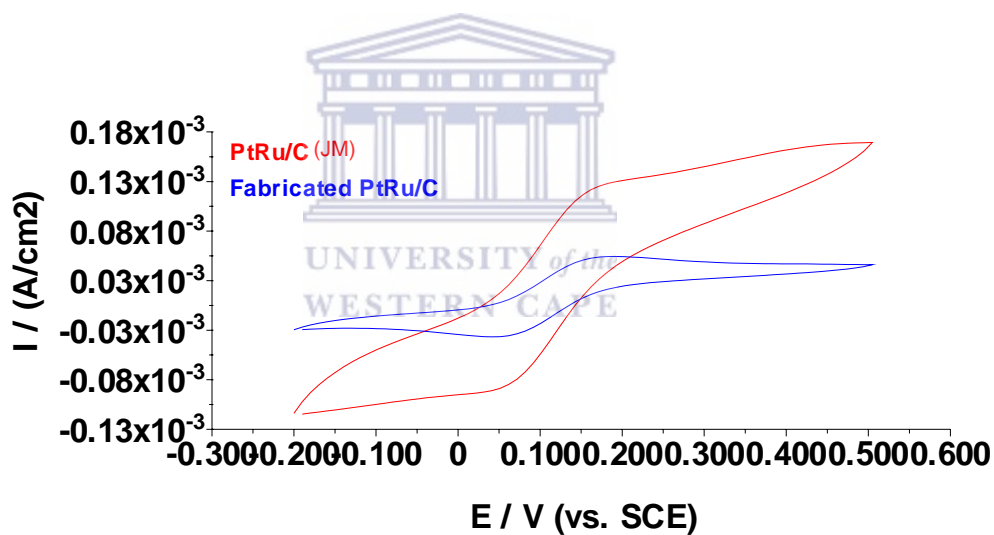
APPENDIX C1: Cyclic voltammograms for the electrochemical screening of mesoporous silica-templated carbon analogues in 0.01M $K_4[Fe(CN)_6]$ supported in 0.1M KCl (sweep rate = $20 \text{ mV}\cdot\text{s}^{-1}$)



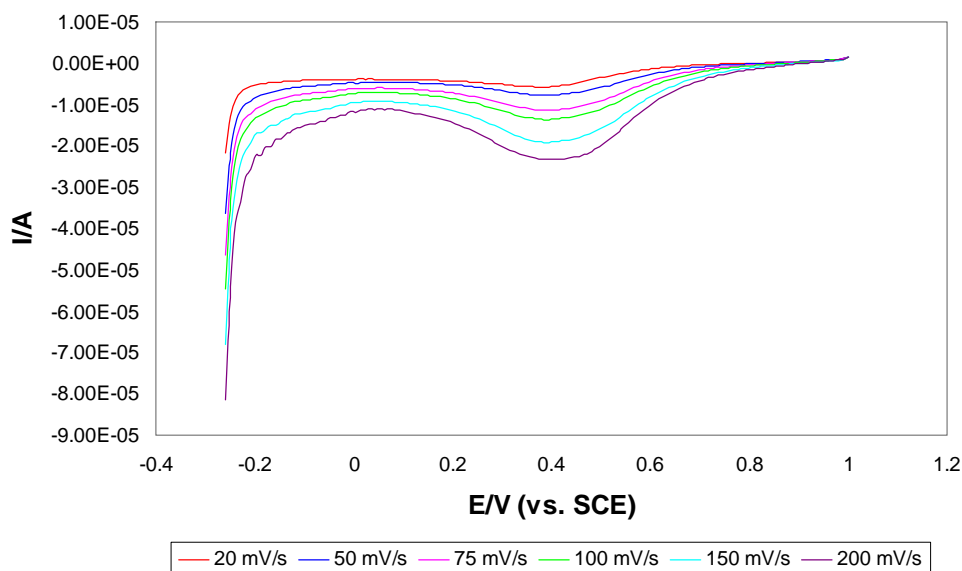
APPENDIX C2: Cyclic voltammograms for the electrochemical screening of mesoporous silica-templated carbon analogues in 0.01M $K_4[Fe(CN)_6]$ supported in 0.1M KCl (sweep rate = $20 \text{ mV}\cdot\text{s}^{-1}$)



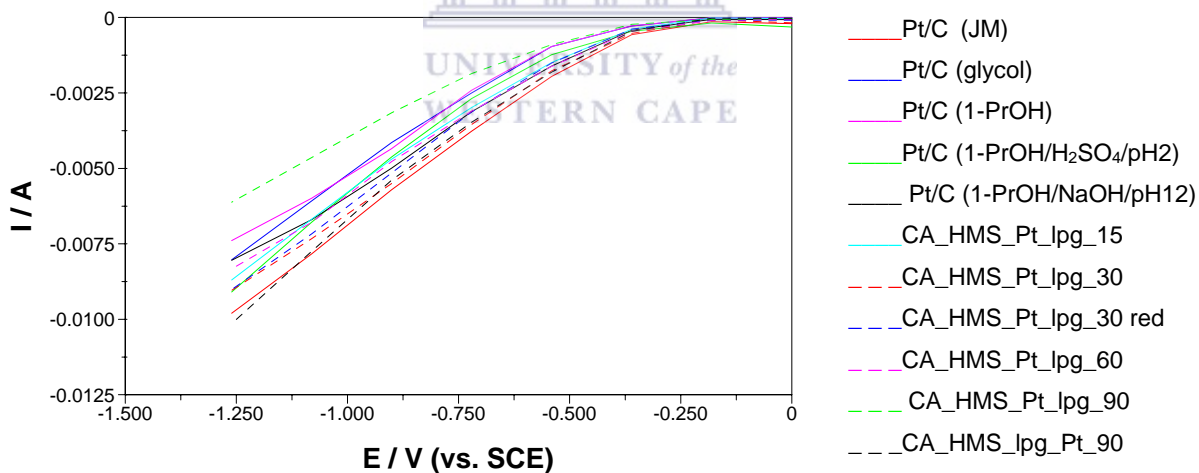
APPENDIX C3: Cyclic voltammograms for the electrochemical screening of fabricated and commercial supported Pt nanophase electrocatalysts in 0.01M $K_4[Fe(CN)_6]$ supported in 0.1M KCl (sweep rate = 20 $mV \cdot s^{-1}$)



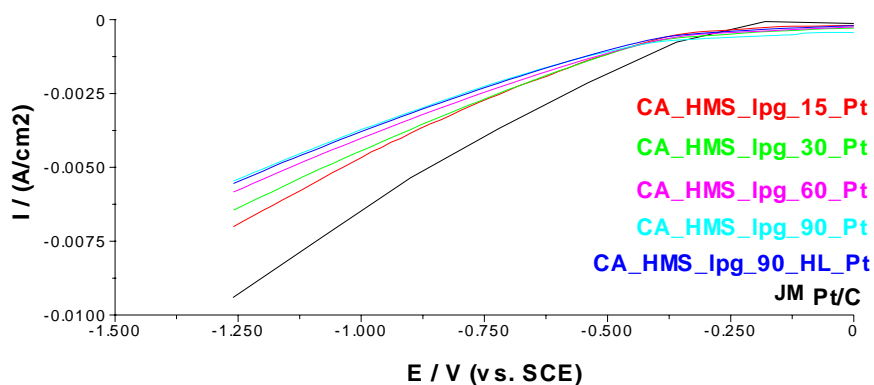
APPENDIX C4. Cyclic voltammograms for the electrochemical screening of fabricated and commercial carbon-supported PtRu nanophase electrocatalysts in 0.01M $K_4[Fe(CN)_6]$ supported in 0.1M KCl (sweep rate = 20 $mV \cdot s^{-1}$)



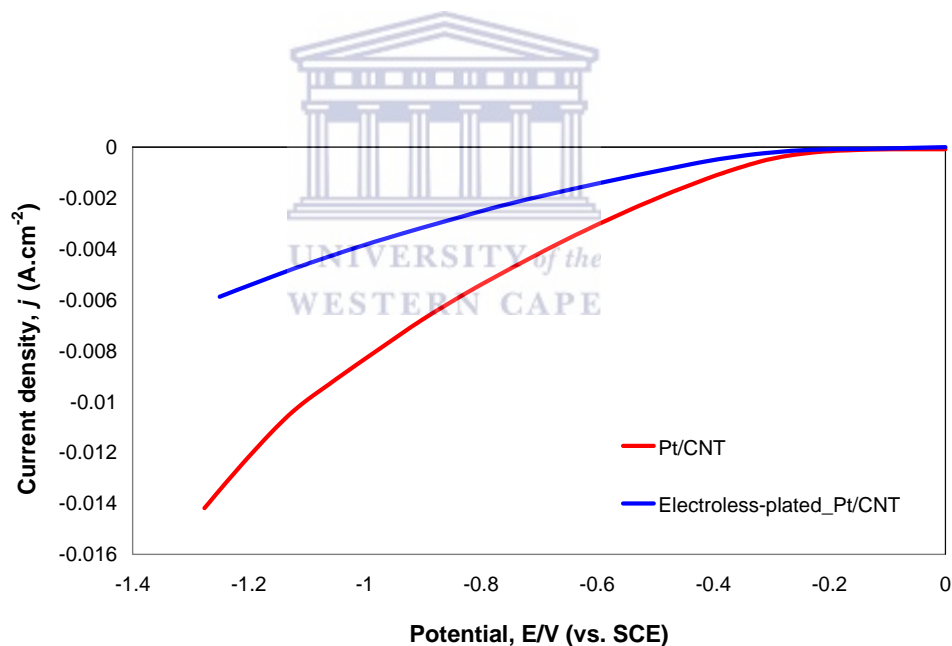
APPENDIX D: Voltammograms for the oxygen reduction reaction on a smooth Pt electrode with increasing sweep rate in 0.5M H₂SO₄



APPENDIX E1. Linear-sweep voltammograms for the electrochemical screening of fabricated and commercial carbon-supported Pt nanophase electrocatalysts and mesoporous silica-templated carbon analogues in the hydrogen evolution reaction in 0.5M H₂SO₄ (sweep rate = 20 mV.s⁻¹)



APPENDIX E2. Linear-sweep voltammograms for the electrochemical screening of fabricated mesoporous silica-templated carbon analogues in the hydrogen evolution reaction in 0.5M H₂SO₄ (sweep rate = 20 mV.s⁻¹)



APPENDIX E3. Linear-sweep voltammograms for the electrochemical screening of fabricated carbon nanotube-supported Pt nanophase electrocatalysts in the hydrogen evolution reaction in 0.5M H₂SO₄ (sweep rate = 20 mV.s⁻¹)